Stability of a stratified fluid on a wall and in a channel

Jun Chen

CENTRALE MARSEILLE

École Doctorale : Nom de l'école doctorale (ED353)

Institut de Recherche sur les Phénomènes Hors Equilibre

THÈSE DE DOCTORAT

pour obtenir le grade de

DOCTEUR de l'ÉCOLE CENTRALE de MARSEILLE

Discipline : Mécanique et physique des fluides

STABILITÉ D'UN ÉCOULEMENT STRATIFIÉ SUR UNE PAROI ET DANS UN CANAL

par

CHEN Jun

Directeur de thèse : **LE DIZÈS Stéphane**
Co-directeur de thèse : **MEUNIER Patrice**

Soutenue le 27 september 2016

devant le jury composé de :

CHOMAZ Jean-Marc	LadHyX	Rapporteur
COSSU Carlo	IMFT	Rapporteur
FLÓR Jan-Bert	LEGI	Examinateur
ROBINET Jean-Christophe	DynFluid	Examinateur
PASSAGGIA Pierre-Yves	UNC	Examinateur
LE DIZÈS Stéphane	IRPHE	Directeur de thèse
MEUNIER Patrice	IRPHE	Co-directeur de thèse

Remerciements

I would like to thank all those people who helped me during my studies.

First of all, I deeply thank my supervisor Stéphane Le Dizès, for his instructive advice and encouragement. He has offered me guidance through all stages of this thesis. I am also thankful to Patrice Meunier, who have put considerable time and effort into the drafts and given me constructive suggestions, especially about the scientific expressions.

Second, I would like to express my very sincere gratitude to Jean-Marc Chomaz and Carlo Cossu, for having accepted to be the rapporteurs. And I'm also grateful to my examiners, Jan-Bert Flór, Jean-Christophe Robinet, and Pierre-Yves Passaggia, for their time and interests.

I'm thankful to everyone I met in IRPHE for these pleasant three years.

Special thanks should go to Prof. Sun Xiaofeng and Prof. Julian Scott for their recommendations and support on this opportunity.

Last but not the least, I should thank China Scholarship Council for their financial support.

Table des matières

Abstract

In the present thesis, the stability of a boundary layer on a vertical wall and a channel flow between two vertical walls is studied in the presence of density stratification.

For the boundary layer, a temporal stability analysis is performed for a tanh velocity profile. The characteristics are analysed as functions of the Reynolds number $Re = UL/\nu$ and the Froude number $F = U/(LN)$, while neglecting the diffusion of density. The non-dimensionalisation is based on the main stream velocity U, the boundary thickness L and kinetic viscosity ν. Besides, N is the buoyancy frequency. The boundary layer is found to be unstable to viscous instability and radiative instability. The classical viscous instability can lead to Tollmien–Schlichting (TS) waves, and the radiative instability may generate gravity waves spontaneously. We demonstrate that the most unstable TS wave remains two-dimensional (2D) in the presence of stratification and therefore independent of F. However, the radiative instability is three-dimensional (3D), inviscid in nature and strongly affected by the stratification. The radiative instability appears first for $Re > Re_c^{(r)} \approx 1995$ for a Froude number close to 1.5 whereas the critical Reynolds number for viscous instability is $Re > Re_c^{(v)} \approx 3980$. Comparing the growth rate of these two instabilities, we demonstrate that, for large Reynolds numbers, the radiative instability dominates the viscous instability. Consequently, the radiative instability may develop in experiments and various geophysical situations in the ocean and atmosphere.

For the channel flow, we choose plane Poiseuille flow as a prototype. Both the exponential instability and transient growth are analysed as functions Re and F. The Schmidt number $Sc = \nu/D$ is set as 1, where D is the mass diffusivity. The length scale for normalisation is half the channel width. According to the modal analysis, there are also two kinds of exponential instabilities : a viscous instability and a 3D instability associated with a resonance mechanism. The results of modal analysis are similar to those for the boundary layers. In addition to that, the 3D instability plays an important role in the non-modal analysis for the transient growth. The fundamental mechanisms in transient growth are commonly identified as the inclination of upstream tilting waves and the growth of streamwise vortices, which are referred to as Orr mechanism and lift-up mechanism. In the presence of stratification, the Orr mechanism is not affected while the lift-up mechanism is weakened. The combination of these two mechanisms, which give rise to titled roll vortices, is amplified by the influence of the 3D instabilities.

Chapitre 1

Introduction

The understanding of fluid on earth leads us to the study of geophysical fluids. In general, these fluids are stratified fluids such as the atmosphere and the ocean. Various layers are formed in nature due to the stratification. These layers have important effects on the geophysical movements such as climate changes and ocean currents. The ecosystem is also highly influenced through temperature, salinity and transport of micro-organisms, etc.

In stratified fluids like ocean interior and atmosphere, turbulence mixing is a phenomenon that frequently appears. Moreover, mixing and stratification effects are essential to the global distribution of energy and nutrients. This property makes them quite significant to climate and biogeochemical cycles in nature circulation system (Wunsch & Ferrari 2004; Kuhlbrodt *et al.* 2007). Therefore, their influences and related mechanisms are worth thorough examinations.

1.1 Basic concepts about stratified fluid

The stratified fluid is a fluid with density variations in the vertical direction. Two typical examples of stratified geophysical fluid are the Earth's atmosphere and its ocean. Besides, although not commonly mentioned, the Earth's liquid core and the fluids in the core of other celestial bodies in astrophysics are all stratified.

Stratification is the result of multiple factors. For the Earth, the atmosphere is a gaseous envelope surrounding our planet, and the density stratification mainly results from its compressibility and the Earth's gravity. Figure 1.1 shows the spatial variations of density on the altitude and density decreases as the altitude increases. The density stratification in the atmosphere is also affected by temperature differences, which is the result of solar radiation, greenhouse effects and the presence of clouds. According to the temperature, the atmosphere is usually divided into four layers along elevation : troposphere, stratosphere, mesosphere, and thermosphere. The troposphere contains nearly 80%

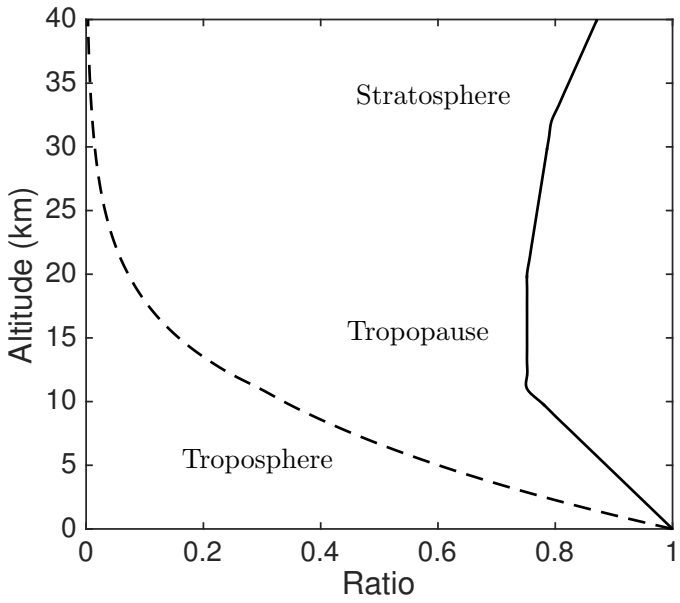

FIGURE 1.1 – Density and temperature profiles of the atmosphere (US Standard Atmosphere, 1976). The solid line is the temperature ratio $T_N = T/T_0$, and the dashed line is the density ratio $\rho_N = \rho/\rho_0$, where $T_0 = 288.15\ K$ and $\rho_0 = 1.226\ kg/m^3$.

of the total mass and almost all water vapour. Meteorologists mainly focus on this region as it is the place where most weather occurs.

The density stratification in the ocean is shown in figure 1.2(a) and this stratification results from the temperature and salinity variations, which are demonstrated in figure 1.2(b). The density gradient is the largest in the layer called pycnocline. This region is stably stratified and separates the mixed layer of the surface and deeper ocean. The separation may hinder vertical transport, but Fernando (1991) indicated that vertical mixing still appears due to the turbulence triggered by the shear effects. Such kind of mixing has significant effects on the marine ecosystem and transports nutrients in the ocean.

1.1.1 Buoyancy frequency

Stratification is usually stable in nature, as shown in figure 1.1 and figure 1.2. Under gravity, a stratified fluid tends to arrange itself so that heavier fluid (the fluid with higher density) are below the lighter fluid. If we consider a fluid in static equilibrium, this situation will be an intuitively stable status. However, if a fluid parcel is disturbed vertically and deviates from its equilibrium position, a recalling force will be produced by the buoyancy force and gravity. This process is illustrated in figure 1.3. Hence, the displaced parcel will oscillate around the equilibrium level under the recalling force. The frequency of the oscillation is termed as the buoyancy frequency, which is also named as Brunt–Väisälä frequency or stratification frequency. The buoyancy frequency is defined

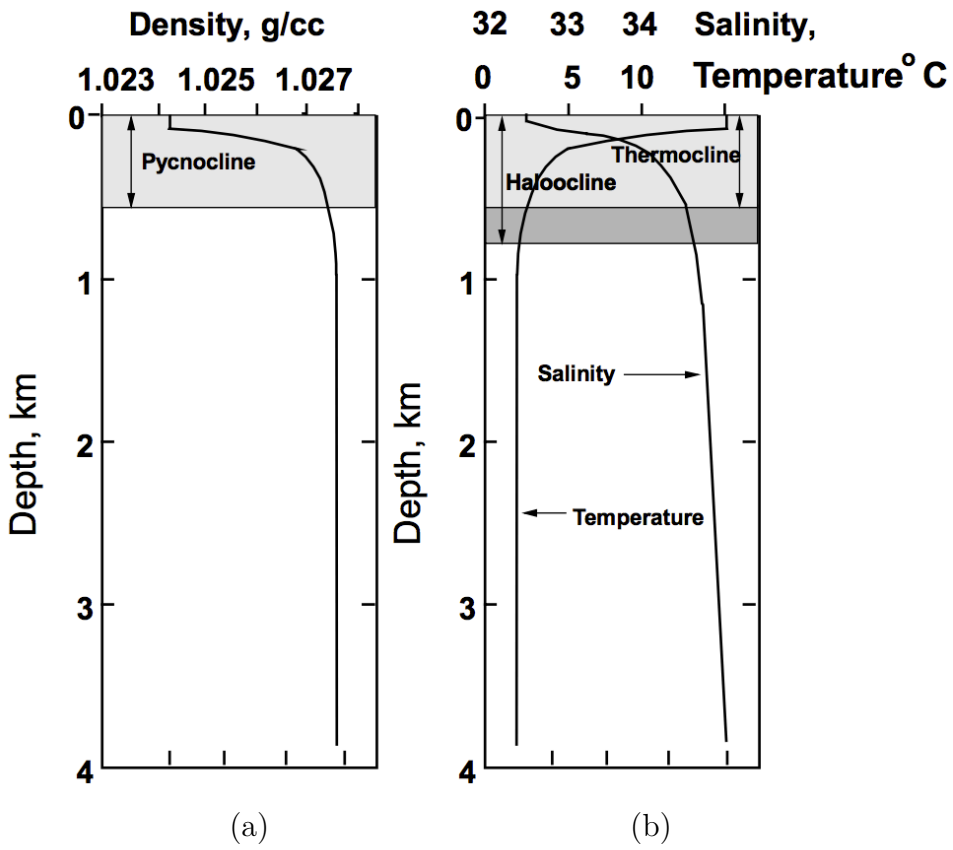

FIGURE 1.2 – Variations of different quantities for the depth in the ocean : (a) density, (b) salinity and temperature. Pycnocline, haloocline, thermocline are marked for the density, salinity and temperature respectively. Source : URL *http* : *//ocean.stanford.edu/courses/bomc/chem/lecture_*03*.pdf*

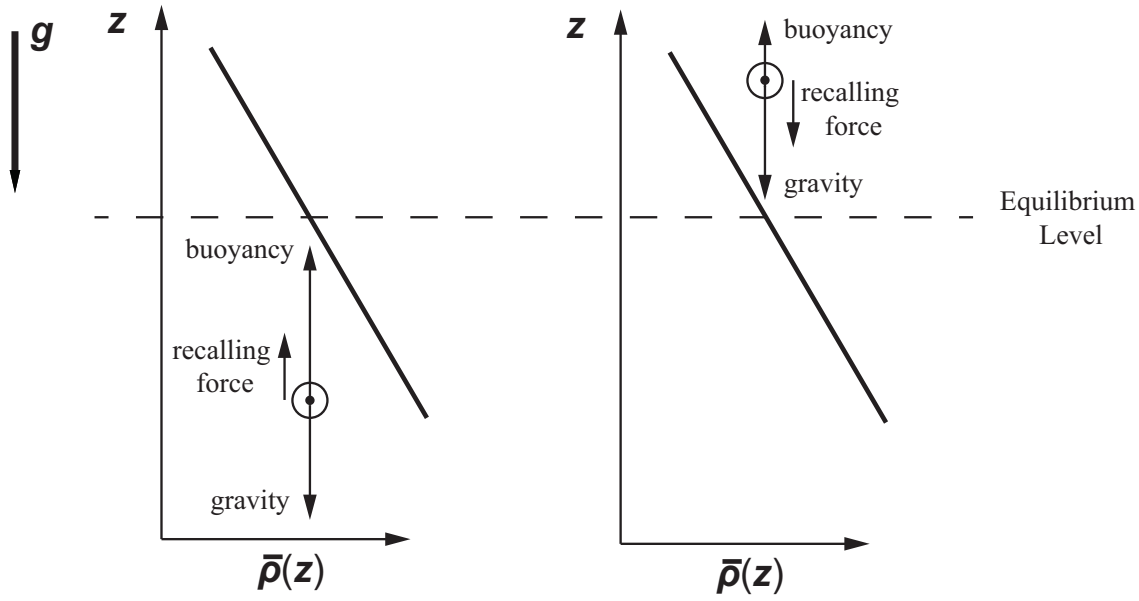

FIGURE 1.3 – Sketch of the oscillation in stably stratified fluid, which supports internal gravity waves. The buoyancy frequency is determined in this process.

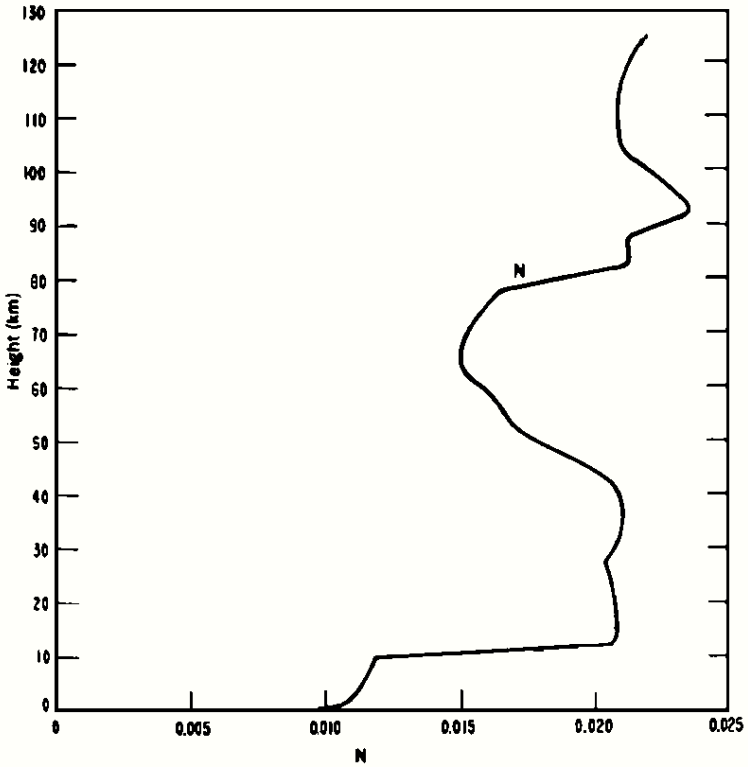

FIGURE 1.4 – Distribution of buoyancy frequency N (Hz) for the US standard atmosphere. Source : Gossard & Hooke (1975).

as $N = \sqrt{-g\partial_z \rho/\rho_0}$, where z is the vertical direction, g the gravity and ρ_0 the reference density. If $\partial_z \rho > 0$ in the definition of buoyancy frequency, which corresponds to a state where a heavier fluid is on top of the lighter fluid, overturning will appear in this case. Furthermore, if a persistent external destabilisation is forced onto the fluid, such as heating on the bottom or cooling on the top, convection will dominate the fluid motion. In the following content of the thesis, our attention mainly focuses on the stably stratified fluid so that the buoyancy frequency is real in our studies.

The oscillation described in this section obviously exists in the atmosphere and ocean, as both of them are stably stratified fluids in terms of density. However, for compressible fluid like the atmosphere, the definition of buoyancy frequency is based on the potential temperature (figure 1.4). The buoyancy frequency in nature are depicted in figure 1.4 and figure 1.5 as examples. The profile in the atmosphere, as shown in figure 1.4, has more variations and a larger average frequency than that of the ocean. The maximum buoyancy frequency shown in figure 1.5 is approximately $N \approx 0.02$ rad $\cdot$ s^{-1}.

The oscillations of a fluid parcel can propagate in the medium and then, waves are formed through propagation. To differentiate the external gravity wave (surface wave), which is generated by a similar but different mechanism, we can particularly call them the internal gravity waves. However, unlike the normal surface waves, internal waves can stretch tens of kilometres in length and propagate throughout the ocean for several hours. As an example, the buoyancy frequency in the Sulu Sea illustrated in figure 1.5 was

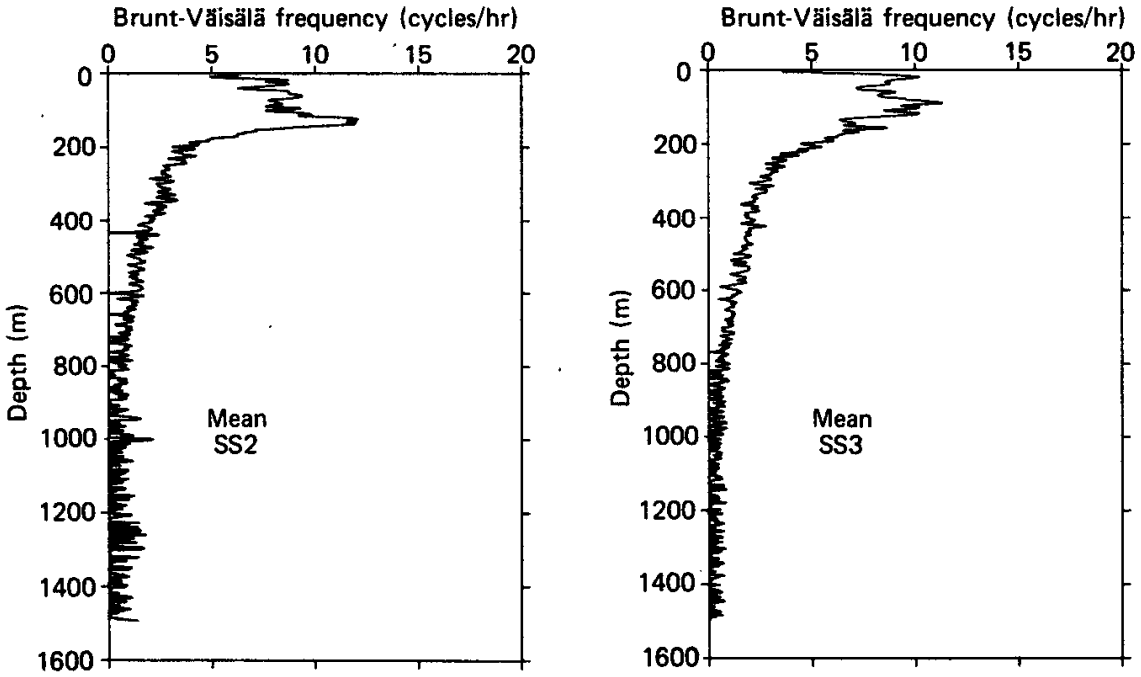

FIGURE 1.5 – Observed buoyancy frequency in the Sulu Sea. SS2 and SS3 are two mooring sites near the centre of the Sulu Sea and the mean profiles around these two locations are illustrated here. Source : Apel *et al.* (1985)

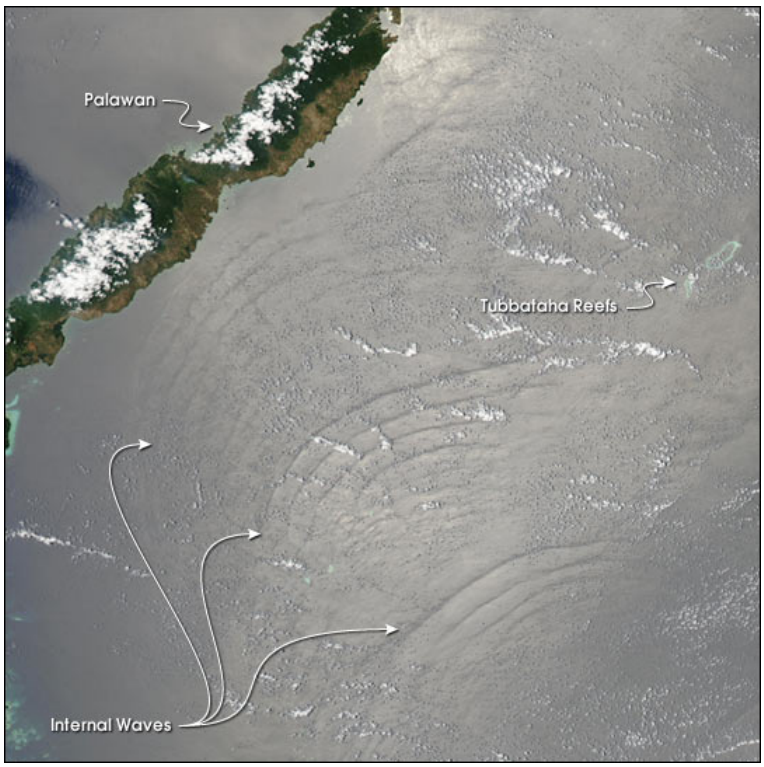

FIGURE 1.6 – Internal waves observed in the Sulu Sea by satellite. Source : Acquired on April 8, 2003. Image courtesy Jacques Descloitres, MODIS Land Rapid Response Team at NASA GSFC

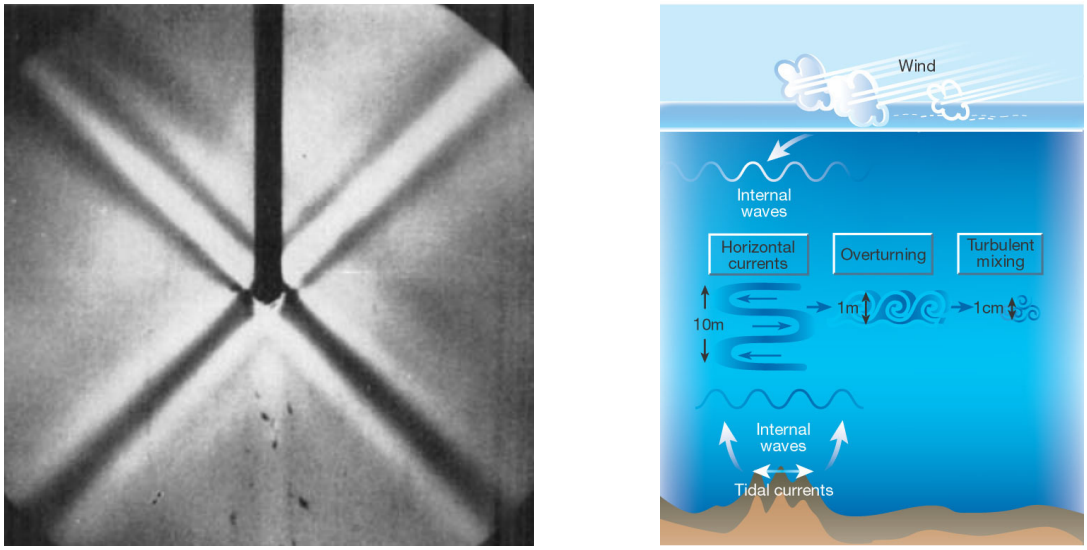

(a) (b)

FIGURE 1.7 – Characteristics of internal waves. (a) Schlieren image of internal waves, generated by oscillating a horizontal cylinder in a stratified fluid. Source : Mowbray & Rarity (1967). (b) Small-scale mixing processes in ocean interior. Source : Garrett (2003)

measured by Apel *et al.* (1985). The internal gravity waves appear can also be observed by satellite, as shown in figure 1.6 in the Sulu Sea.

1.1.2 Internal gravity wave

The internal gravity waves are transverse waves as the movement of the fluid parcels is perpendicular to the direction of wave propagation. For a freely-propagating internal gravity wave, there is a special characteristic : the group velocity is perpendicular to the phase velocity. As shown in figure 1.7(a), internal gravity waves can be generated experimentally in a uniformly stratified fluid (constant N), and the energy is propagating away along surfaces of constant phase (Mowbray & Rarity 1967). More features and behaviours of internal gravity waves can be described with the help of linear theories, as reviewed by Fritts & Alexander (2003). The influences and effects of these waves are evaluated in these theories.

In nature, internal gravity waves also become visible in the satellite era, for example, figure 1.6 and 1.8. Internal waves exist both in the atmosphere and in the ocean, where the density stratification is stable and continuous. They are significant in vertical transfer and mixing.

In the circulation system of the ocean, the internal gravity waves transport micro-organisms, plankton, and nutrients. However, the physics of mixing in ocean interior is not well understood, and the internal mixing problem should be considered (Ivey *et al.* 2008). Although existing in the interior, internal gravity waves can alter the sea surface currents and make a difference. Where these currents converge, the surface is more turbulent and

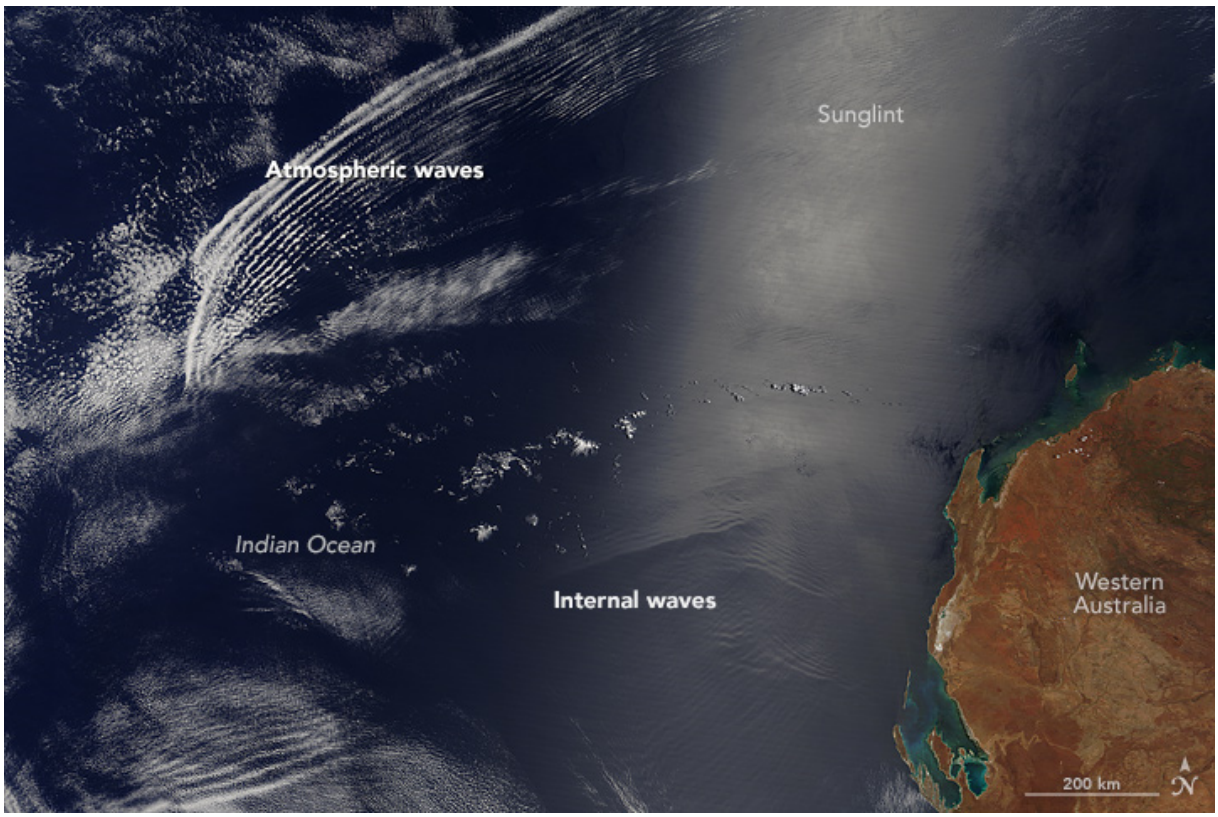

FIGURE 1.8 – Marks of gravity waves in the atmosphere and ocean. Source : Acquired on February 10, 2016. NASA image by Jeff Schmaltz, LANCE/EOSDIS Rapid Response. Caption by Mike Carlowicz and Holli Riebeek.

brighter. Where they diverge, the surface is smoother and darker, and thus, creating a zone called "slicks". The slicks in the Sulu sea appear as dark bands in the centre of figure 1.6. Faint but visible ripples of internal gravity waves appear in figure 1.8 with the help of sunlight. In the ocean, the corresponding waves are tens to hundreds of meters beneath the sea surface and propagate slowly there. The comparisons of the scales in the mixing processes are shown in figure 1.7(b). Phenomena that mix the ocean are hard to be resolved in general ocean circulation models because the scales of relevant turbulent eddies are typically smaller than the grid spacing. In both ocean and atmosphere, this kind of small eddies should be examined so that their effects can be parametrized (Garrett 2003).

In the atmosphere, internal waves mainly appear in the troposphere where the density is relatively high. Due to a decrease in density, the amplitude of these waves has a quasi-exponential growth when propagating in the vertical direction. Hence, at a certain altitude, the energy and momentum of these waves are transported and spread as turbulence mixing. Although the gravity waves themselves are not visible in the atmosphere, the marks of their propagation are left behind and represented by the cloud. The special structures appear on satellite photos, for example, figure 1.8, where the uncommon clouds are marked as atmospheric waves.

The gravity waves in the atmosphere are usually caused by the mountain waves (Lee

waves), which have been studied for a long time through multiple observations and analysis Fritts & Alexander (2003). We often see the waves patterns of the clouds when the dry air moves towards the much moister air. The dry air pushes the moist air higher in the atmosphere, causing water vapour to amass into clouds. When the moister air rises, the gravity pulls it down since it is heavier in density. This procedure repeats and forms the wave patterns in the clouds. However, the source of the atmospheric waves shown in figure 1.8 is not clear. Because the wave patterns are far from the inland, and Western Australia is relatively flat, it is unlikely that these patterns are formed by mountain waves. The studies of internal gravity waves require further attentions because of their importance in global energy circulation and energy budget.

Numerous studies have also examined the effects of stable stratification in the context of atmospheric flows (Mahrt 2014). The internal gravity waves are fully three-dimensional in space, and they are relatively small compared to the normal scales in climate models. With the influence of some instabilities, the exchange of energy and momentum by internal gravity wave can lead to turbulence, mixture and dissipation (Staquet & Sommeria 2002).

To have a better understanding of mechanisms and mixing effects, we need to take the localized dissipation of energy and small-scale processes into account. The onset of turbulent mixing is related to the instability of fluid. To uncover the basic physical mechanisms of instabilities, we need to simplify the realistic complex context while keeping the essential characteristics of the flow. Researches on the instability start with homogeneous fluids, both experimentally and theoretically.

1.2 Modal instability in stratified shear flow

The instability of shear flows has been a classic subject in fluid dynamics since the theoretical studies of Rayleigh (1880) and the experiments by Reynolds (1883) at the end of 19th century, and it is covered by several textbooks (e.g. Drazin & Reid 1981; Schmid & Henningson 2001). For the instability problem, small amplitude perturbations and linearised Navier-Stokes equations are useful approximations and methods in the research field. With the exactly parallel base flow profiles, the linearized instability can be determined by the eigenvalue problem of Orr-Sommerfeld equation and the critical Reynolds number can be defined by the solutions. Some of the well-known instabilities are reviewed in this section.

1.2.1 Kelvin-Helmholtz instability

The instability associated with the inflexion point of the velocity profile (Kelvin-Helmholtz instability) is the one of the first instabilities discovered in fluid mechanics. The Kelvin-Helmholtz instability may appear in the atmosphere, as outlined by the clouds in

FIGURE 1.9 – Special cloud structures formed by Kelvin-Helmholtz instability. Source : Terry Robinson, URL : *http* : *//www.telegraph.co.uk/*

figure 1.9. The question of in what circumstances, this instability occurs in shear flows has occupied many generations of scientists. First works have concerned homogeneous fluids. Rayleigh (1880) demonstrated that a necessary condition for a parallel inviscid shear flow to become unstable is the existence of inflexion point in the velocity profile. Wavelike disturbances appear in this kind of unstable flow and grow exponentially with time. Fjørtoft (1950) later complemented that the inflexion point has to correspond to a maximum (rather than a minimum) of the velocity shear. Another general stability condition is called Howard's semicircle theorem (Howard 1961). This condition bounds the complex phase velocity of the disturbance in a semicircle, whose diameter is the difference between the largest and smallest velocity in the parallel shear flow.

The stable stratification is intuitively believed to have a stabilising effect. In a stably stratified fluid, Miles (1961) and Howard (1961) showed that the criterion of Kelvin-Helmholtz instability for two-dimensional inviscid parallel shear flow can be determined by the local Richardson number (Ri), which is the square of the ratio between buoyancy frequency and the vertical velocity shear rate. The Miles-Howard theorem states that the flow is stable when the local Richardson number is everywhere greater than or equal to 0.25. The stable stratification is thus believed to have a stabilisation effects on Kelvin-Helmholtz instability and can even eliminate the turbulence when the stratification is strong enough. However, the numerical simulations (e.g. Riley & De Bruyn Kops 2003; Lindborg 2006), laboratory experiments (e.g. Spedding *et al.* 1996; Augier *et al.* 2014)

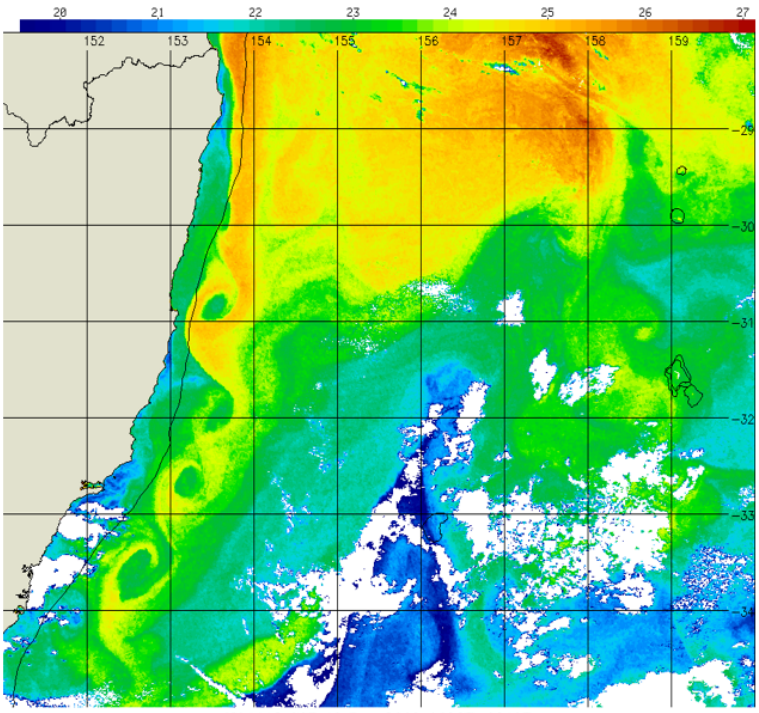

FIGURE 1.10 – Kelvin-Helmholtz instability when when shear and stratification are not aligned. Source : CSIRO Marine Research, Hobart (2002).

and ocean observations (e.g. Mack & Schoeberlein 2004; Polzin & Ferrari 2004) showed unexpected turbulence in strongly stratified fluid ($Ri \geqslant 0.25$). These facts suggest that other mechanisms might be substantial in stratified fluids, and further research is required in the regions beyond the applicability of Miles-Howard theorem.

Little work has been done when shear and stratification are not aligned in the same direction, but such kind of cases occur in nature (e.g. Figure 1.10). The Kelvin-Helmholtz instability is modified in such cases as studied by Deloncle *et al.* (2007), Candelier *et al.* (2011) and Arratia (2011).

1.2.2 Viscous instability (Tollmien-Schlichting wave)

In the subject of instability in fluids, the viscosity is well-known to have dual roles. Most studies about viscous instability depend on the exact parallel shear flows. The plane Poiseuille flow is one of the simplest shear flows, but its instability and transition to turbulence have proved to be subtle. As a result, this flow is widely used to illustrate the fundamentals of the stability theory (Drazin & Reid 1981).

In the context of an unstratified fluid, Heisenberg (1924) first demonstrated the viscous instability mechanism for plane Poiseuille flow. As the velocity profile of base flow has no inflexion point, the instability must be related to viscosity. The Reynolds number of the base flow can estimate the effects of viscosity, and instability appears when the Reynolds number exceeds a specific critical value (the critical Reynolds number). The viscous

instability is commonly referred to as Tollmien-Schlichting (TS) wave (Tollmien 1935; Schlichting 1933) in honour of the researchers who first predicted that Orr-Sommerfeld equation has unstable modes for flows without inflexion points. The Squire's theorem (Squire 1933) gives the assertion that it is sufficient to consider two-dimensional modes to determine the critical Reynolds number. In other words, the most unstable mode is always two-dimensional. Experimental observations of TS wave were obtained by Klebanoff *et al.* (1962).

For unstratified plane Poiseuille flow, Orszag (1971) obtained the critical Reynolds number $Re_c = 5772.22$ from the accurate solution of the Orr-Sommerfeld stability equation. The definition of the Reynolds number is based on the half width of the channel, the centre-plane velocity, and the kinematic viscosity.

Experimental results of Nishioka *et al.* (1975) show good agreement that the small perturbations behave as predicted by the linear stability theory, in a condition of a very low background turbulence level. However, the transition in plane Poiseuille flow is sensitive to ambient disturbances. Carlson *et al.* (1982) observed that both natural and artificially triggered transition can occur for Reynolds numbers slightly greater than 1000, and the most amplified wave is three dimensional. More experimental results (e.g. Nishioka & Asai 1985; Alavyoon *et al.* 1986) and the considerable variations of different critical Reynold numbers indicate that the three-dimensional effects are important in the transition of plane Poiseuille flow, which is opposed to the Squire's theorem. This reduction of critical Reynolds number is related to the so-called subcritical instability. The subcritical instability exists in a fluid with a Reynolds number below the critical one. Experiments in boundary layer flows (e.g. Klebanof 1971; Kendall 1985; Matsubara & Alfredsson 2001) also demonstrate that transition is usually preceded by streamwise motion in the form of streaks rather than the TS waves predicted by modal stability analysis. This phenomenon is especially distinct in the presence of natural background disturbance.

The limitation of Squire's theorem was further revealed by Wu & Luo (2006), who examined the influence of small imperfections on the stability of plane Poiseuille flow. The classical Squire's transformation was also extended by Jerome & Chomaz (2014).

In a stratified fluid, the Squire's theorem is not applicable, but Ohya & Uchida (2003) experimentally proved the existence of TS waves in stratified boundary layers. However, the effect of stratification on TS waves is less understood, and it could be destabilising as indicated by Wu & Zhang (2008*a*). Although the Squire's theorem applies strictly to linear normal-mode analysis for a homogeneous viscous fluid, both the 3D and 2D TS waves should be examined in a stably stratified fluid.

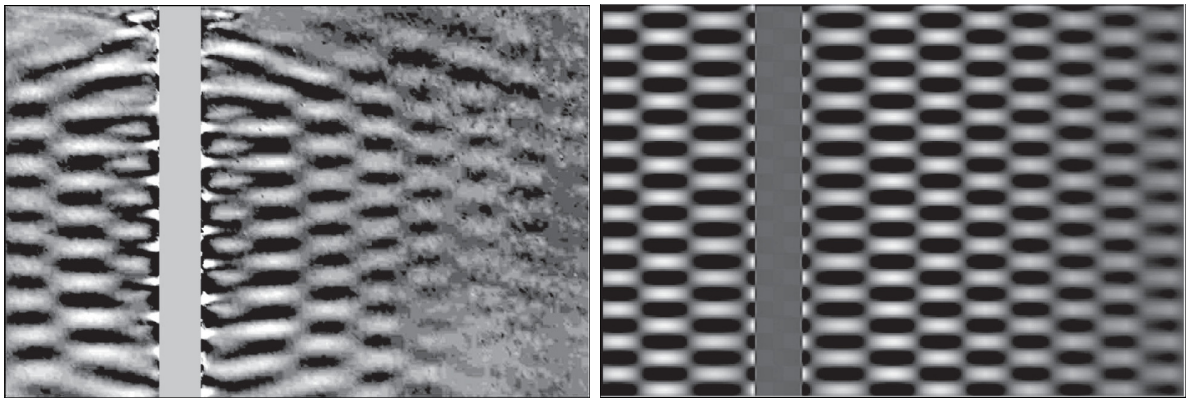

(a) (b)

FIGURE 1.11 – Vertical density gradient pattern of the radiative instability in the Taylor-Couette flow. The grey vertical rectangle corresponds to the cylinder (of radius 15mm). (a) Experimental results obtained with synthetic Schlieren. (b) Numerical results. Source : Riedinger *et al.* (2011)

1.2.3 Radiative instability

Although it may be true to a degree that stratification can stabilise the fluid (Miles 1961; Howard 1961), instability still exist even without inflexion points in the velocity profiles of the flow. For instance, Churilov (2005, 2008) analysed the stability of the flows with inflection-free velocity profiles in a stratified fluid. Stratified fluids can support internal gravity waves. Together with shear effects, small scale unstable waves are generated and thus can promote turbulent mixing in stratified fluids.

When shear and stratification are not aligned, an inflection-free boundary layer can become unstable. The coupling between shear effects and internal gravity waves becomes the strongest when the inclination angle between shear and stratification is $\pi/2$, as demonstrated by Candelier *et al.* (2012). The responsible instability for this phenomenon is called radiative instability. The word 'radiative' describing this instability is borrowed from the quantum mechanics because the demonstrated phenomenon is analogous to the radioactive decay of nuclei (Le Dizès & Billant 2009).

The radiative instability is a hydrodynamic instability that is much less known than the shear instability. However, it has been a subject of many works for decades, and it has also shown its significant influences with some specific conditions. Broadbent & Moore (1979) first found the radiative instability in the context of vortices in a compressible fluid. This instability appears in various contexts, in the shallow waters associated with surface gravity waves, in compressible fluids with acoustic waves and in linearly stratified flows with internal gravity waves. The genesis of radiative instability is reviewed in Riedinger (2009).

With the help of a WKBJ analysis for large axial wave number, Le Dizès & Billant (2009) and Billant & Le Dizès (2009) showed that the radiative instability could be vie-

wed as a result of an over-reflection process at a critical level. The relationship between instability and over-reflection mechanism has been studied for a long time (e.g. Lindzen & Tung 1978; Lindzen & Barker 1985). Further details about this mechanism will be explained later in section 1.3.1.

In recent researches, Riedinger *et al.* (2010*a*) obtained radiative instability for the Lamb–Oseen vortex and analysed the Froude and Reynolds number effects. Experimental results were first provided in Riedinger *et al.* (2010*b*). In figure 1.11, Riedinger *et al.* (2011) also demonstrated, both experimentally and numerically, the occurrence of the radiative instability generated by a rotating cylinder in the stratified flow. In Taylor–Couette and Keplerian flows, Le Dizès & Riedinger (2010) analysed the transition of the instability for a finite-gap, which is associated with a mechanism of resonance, into the radiative instability for an infinite gap. Park & Billant (2013*b*) studied the stability of stratified Taylor-Couette flow and its relationship to radiative instability. Park & Billant (2012, 2013*a*) also investigated the radiative instability of a columnar Rankine vortex in a stratified rotating fluid.

In addition to the stratified rotating flows, the radiative instability can also be found in supersonic flows (Mack 1990; Parras & Le Dizès 2010), atmospheric jets, boundary layers (Candelier 2010; Candelier *et al.* 2012) and stratified shallow waters (Satomura 1981; Riedinger & Gilbert 2014).

1.3 Mechanisms of modal instability in stratified fluids

Because of the abundant literature about the radiative instability and its universal characters, the mechanism was rediscovered several times in history by different communities, and was explained in terms of over-reflection phenomenon (Grimshaw 1979; Lindzen & Barker 1985; Takehiro & Hayashi 1992), negative energy waves (Kópev & Leontev 1983; Schecter & Montgomery 2004) or spontaneous wave emission (Plougonven & Zeitlin 2002; Le Dizès & Billant 2009).

The details of the over-reflection process is explained in this part.

1.3.1 Over-reflection phenomenon

Over-reflection is a phenomenon that the incident waves in a fluid can be reflected with a consequent increase in amplitude. In other words, the reflection coefficient in some circumstances can be greater than 1. This mechanism is found in numerous situations and physical models. The over-reflection phenomenon was first encountered in the field of sound waves by Miles (1957) and Ribner (1957). Acheson (1976) later summarised the conditions for the occurrences of over-reflection. He also attempted to clarify the way in

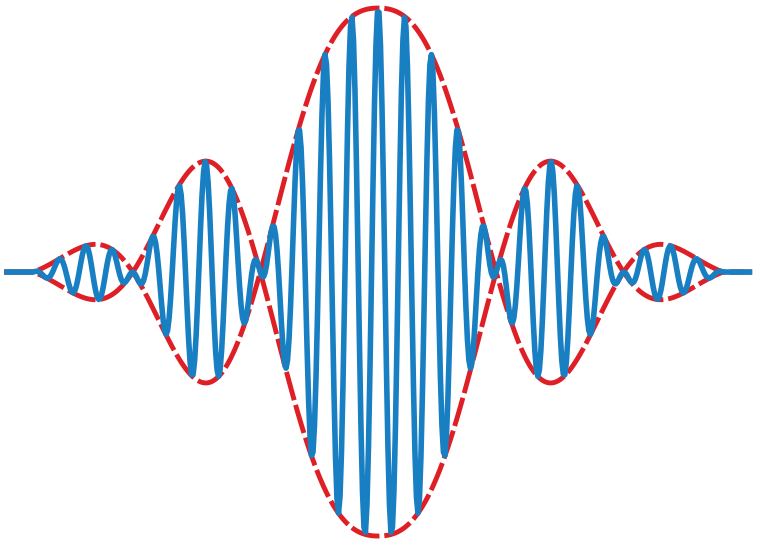

FIGURE 1.12 – A wave packet and its envelope. Solid line : The wave packet. Dashed line : The envelope of the wave packet. The peaks and troughs move at the phase velocity and the envelope moves at the group velocity. Source : Wikipedia

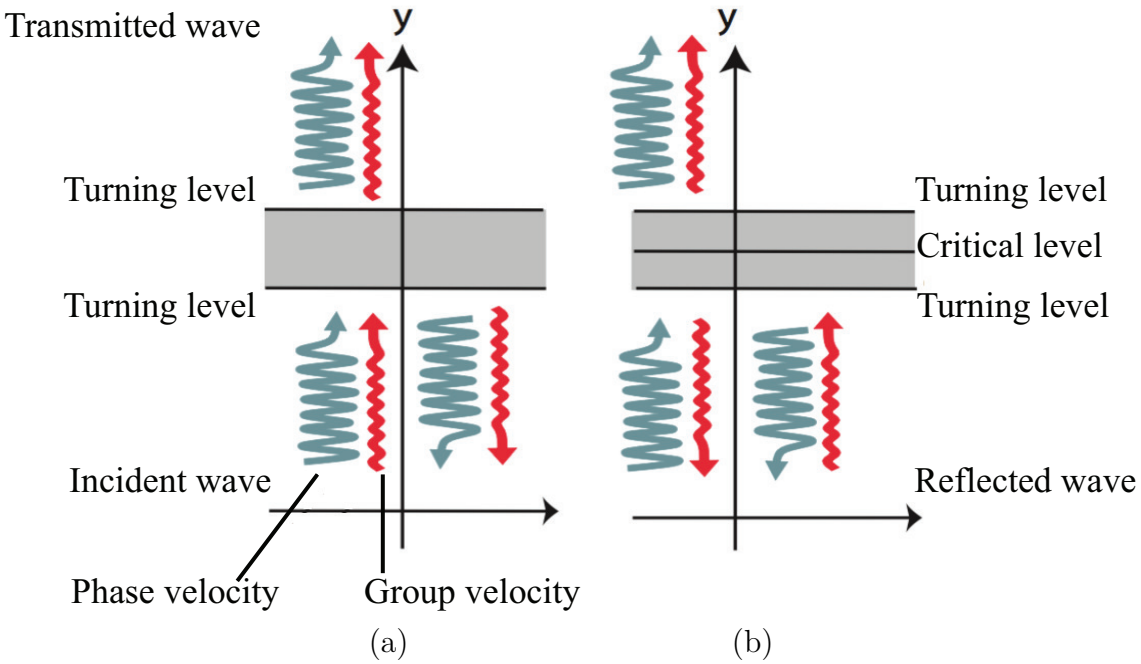

FIGURE 1.13 – Comparison based on the directions of group velocity and phase velocity. (a) Classical reflection ; (b) Over-reflection. Source : Riedinger (2009).

which the excess reflected waves extracted energy from the mean flow motion, and the sense that the transmitted wave can be viewed as a carrier of 'negative energy'. The over-reflection process was thus explained through the conservation of wave action (Acheson 1976).

The summary by Acheson (1976), however, is not sufficient. The connections between over-reflection and unstable modes are discovered in different context (Lindzen & Tung 1978; Lindzen & Rambaldi 1986). Lindzen (1988) summarised and gave the statement that the mode which satisfies 'quantization' conditions can become unstable through the over-reflection process. Then the unstable mode determines the wave geometry.

A quantization zone is an oscillating area confined either by two turning levels or by one turning level together with a perfectly reflecting wall. Perturbations in this area will propagate, be reflected by over-reflection and thus increase. The reflection is always accompanied by a transmitted wave in the external transmission region. This reflection satisfies the conservation law of momentum for three waves : incident, transmitted and reflected waves. However, the conservation law of energy is different in this case, as part of the energy is drawn from the mean flow motion.

A perturbation in the quantization zone can be modelled as a wave propagating in this domain to illustrate the mechanism. A simple example of a wave packet is shown in figure 1.12. The phase velocity and group velocity may be different and can move towards separate directions.

The comparison between a conventional reflection case and an over-reflection case is illustrated in figure 1.13. In the conventional reflection case (figure 1.13 (a)), for example, the radioactive emission through a potential barrier, there is no critical level inside the evanescent region between two turning levels. The phase velocity and group velocity of the incident wave in the conventional case are in the same direction. The intermediate evanescent region partially reflects the incident wave with an amplitude A_i. The amplitudes of the reflected and transmitted waves are A_r and A_t, respectively. The classical relationship ($A_i = A_r + A_t$) for the amplitudes of these three waves applies to this conventional case.

However, the circumstances are different in the over-reflection case, as illustrated in figure 1.13 (b). In the intermediate evanescent region, there exists a critical level, which has the effect of changing the group velocity's direction. Hence, the directions of the group velocity and phase velocity are opposite in the propagation area of the incident and reflected wave, but not in the field of the transmitted wave. As the group velocity represents the energy of the wave packet, the roles of the incident and reflected waves are 'inverted' from the point of energy conservation. Therefore, the amplitude of the reflected wave is greater than that of the incident wave (i.e. $A_r > A_i$). The transmitted wave has an opposite amplitude ($A_t < 0$) or phase compared to the incident wave, as shown in figure

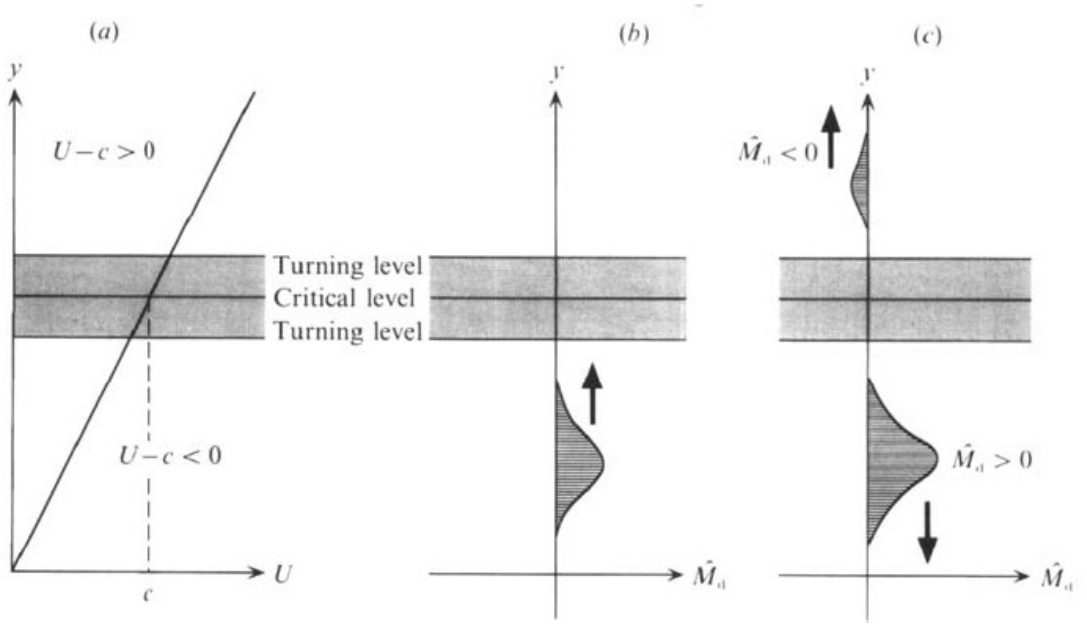

FIGURE 1.14 – Schematic picture of over-reflection. Source : Takehiro & Hayashi (1992).

1.14. According to the amplitudes, the energy associated with the wave packet grows after reflection, and this phenomenon is called 'over-reflection'.

Although the over-reflection process is not a sufficient condition for the appearance of instability in a fluid, many kinds of instabilities are revealed to be associated with this mechanism, for example, barotropic instability (Lindzen & Tung 1978) and baroclinic instability (Lindzen *et al.* 1980). The generation process of radiative instability is illustrated in figure 1.15 based on Takehiro & Hayashi (1992). The wave packet is over-reflected by the critical level and perfectly reflected by the rigid wall. The amplitude of the wave is increased by repeating this process. The disturbance propagates far away and does not diminish like in the common cases. The oscillation frequency and the wavelength are determined by the reflection processes, while the growth rate is associated with the over-reflection.

1.3.2 Resonance phenomenon

In the stratified rotating flows with Taylor–Couette and Keplerian velocity profiles, Le Dizès & Riedinger (2010) showed that the linear inviscid instability change into radiative instability as the size of the gap d becomes infinite, and is associated with a mechanism of resonance when d is finite. This instability is called strato-rotational instability in the Taylor–Couette system and is considered to be directly related to the emission of internal gravity flows (Le Dizès & Billant 2009; Billant & Le Dizès 2009).

The resonance mechanism for small gaps is interpreted by Yavneh *et al.* (2001). For large gaps, results of numerical methods and WKBJ analysis show that when the frequency curves of trapped modes cross, one of the two modes becomes unstable around

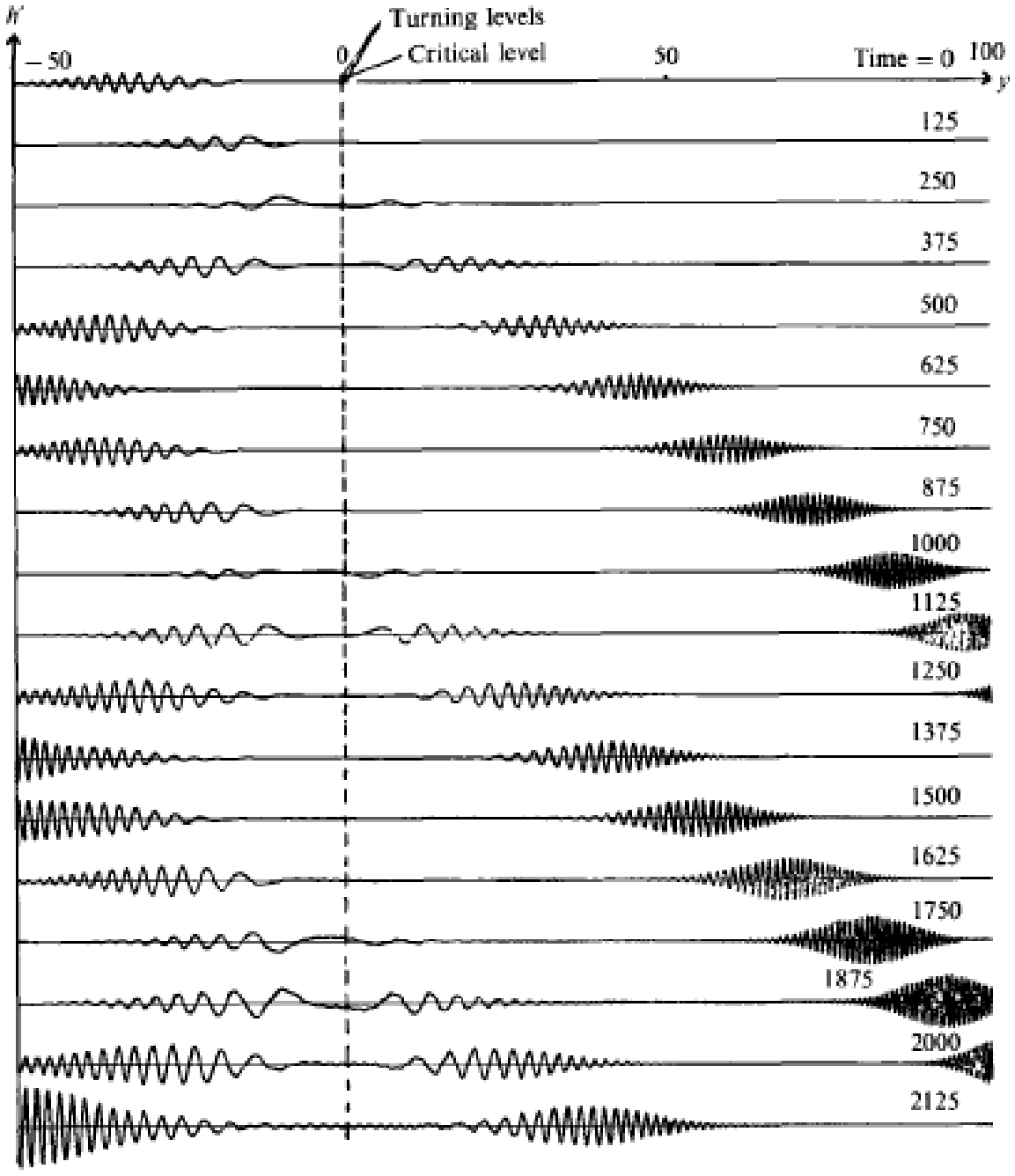

FIGURE 1.15 – Multiple over-reflection of a shallow-water wave. Source : Takehiro & Hayashi (1992).

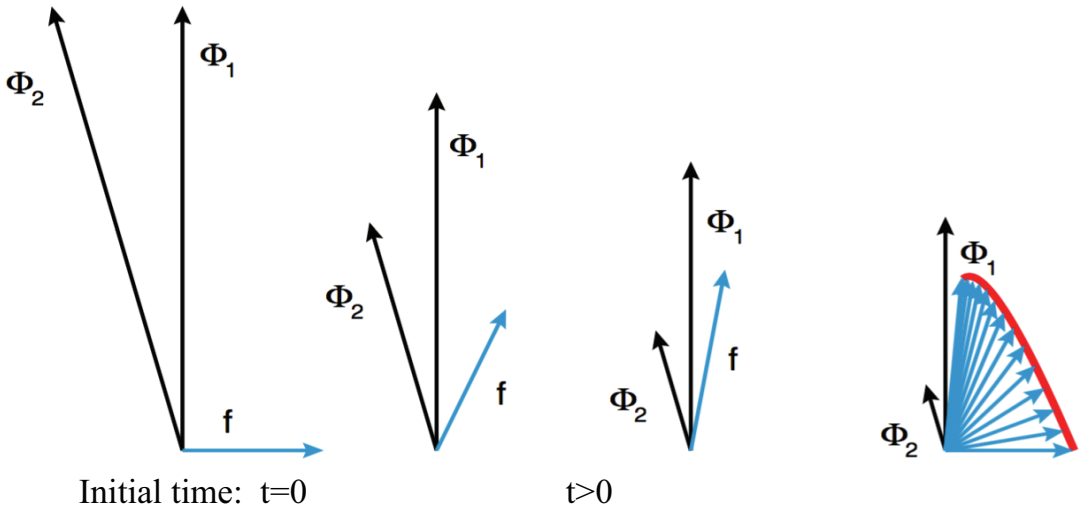

FIGURE 1.16 – Sketch illustrating transient growth. The vector $\boldsymbol{f}$ is defined by the difference between two shrinking vectors $\boldsymbol{f} = \boldsymbol{\Phi}_1 - \boldsymbol{\Phi}_2$, where the vector $\boldsymbol{\Phi}_1$ shrinks by 20% and vector $\boldsymbol{\Phi}_2$ shrinks by 50% starting from the initial time on the left. Source : Schmid (2007).

the corresponding points (Le Dizès & Riedinger 2010). This mechanism of resonance is also described in the context of shallow waters (Satomura 1981). The same phenomenon is to be expected for the stratified plane Poiseuille flow, and we will discuss the resonance mechanism in chapter 4

1.4 Transient growth and optimal perturbation

Modal analysis has dominated the field of stability theory for many decades. Based on the eigenvalue analysis, plenty of significant accomplishments were achieved (e.g. Orr 1907; Tollmien 1929). However, the subcritical instability has shown its importance in numerous studies, as mentioned in section 1.2. The limitation of modal approach is recognised, and then a novel method (transient growth theory) has emerged in the 1990s (e.g. Farrell & Moore 1992; Trefethen *et al.* 1993). Transient growth theory, which can give a quantitative description of the short-time effects of the subcritical instabilities, has drawn considerable attention since then. Even though all eigenvalues are stable according to the modal analysis, a general initial disturbance may undergo large growth in finite time (Butler & Farrell 1992; Reddy & Henningson 1993).

1.4.1 Non-normality and finite time intervals

The transient growth theory has achieved several developments and now provided a better understanding of the transition in various flows (Schmid & Henningson 2001; Schmid 2007).

The finite-time increase of the total perturbation can appear without nonlinear effects. Mathematically, it is because the governing linear operator is not self-adjoint (Butler & Farrell 1992) and the associated eigenfunctions are non-orthogonal (Reddy & Henningson 1993). The linear nature of the transient growth is demonstrated in figure 1.16, and is also revealed in Trefethen *et al.* (1993) and Henningson & Reddy (1994). The basic mechanism can be explained by this simple geometric example (Schmid 2007). Over a finite time interval, the lengths of two component vectors $\boldsymbol{\Phi}_1$ and $\boldsymbol{\Phi}_2$ decrease by 20% and 50%. However, the difference between these two vectors $\boldsymbol{f}$ may grow in length and changes its direction transiently. The vector $\boldsymbol{f}$ can be viewed as an initial condition for a flow at time $t = 0$, and it may be amplified over a finite time interval, even though $\boldsymbol{f} \to \boldsymbol{0}$ when $t \to \infty$ in this specific case. As illustrated by the process in figure 1.16, even if each eigenfunction decays exponentially according to its associated eigenvalue, a linear combination of non-orthogonal eigenfunctions may still lead to large transient growth before the time it eventually decreases at the rate of the least stable eigenfunctions. Although the transient growth in many studies is related to degenerate eigenvalues, it is not necessarily limited to them (Reddy & Henningson 1993).

1.4.2 Optimal perturbation and adjoint equations

Different types of perturbations may experience transient growth, but only the most amplified one can dominate the behaviour and structure of the fluid. The optimal perturbation provides the initial conditions that lead to a maximum energy growth over a finite time interval T, thus is also referred to as optimal initial conditions. The most amplified perturbation at the time $t = T$ can be named as the optimal response. As $T \to \infty$, the optimal response tend towards the eigenfunction associated with most unstable modal instability. Correspondingly, in this case, the optimal initial conditions are determined by the dominant adjoint eigenmode. Even in the flows expected to be stable by the modal analysis, Kerswell *et al.* (2014) demonstrated that when the amplified transient perturbations reach finite amplitude, they may be essential to the 'subcritical' transition.

1.5 Mechanism of transient growth

In the transient growth analysis, two fundamental mechanisms are commonly identified, the Orr mechanism (Orr 1907) and the lift-up mechanism (Ellingsen & Palm 1975; Landahl 1980). The background of these two mechanisms is introduced in this section. First works are also performed on homogeneous fluid.

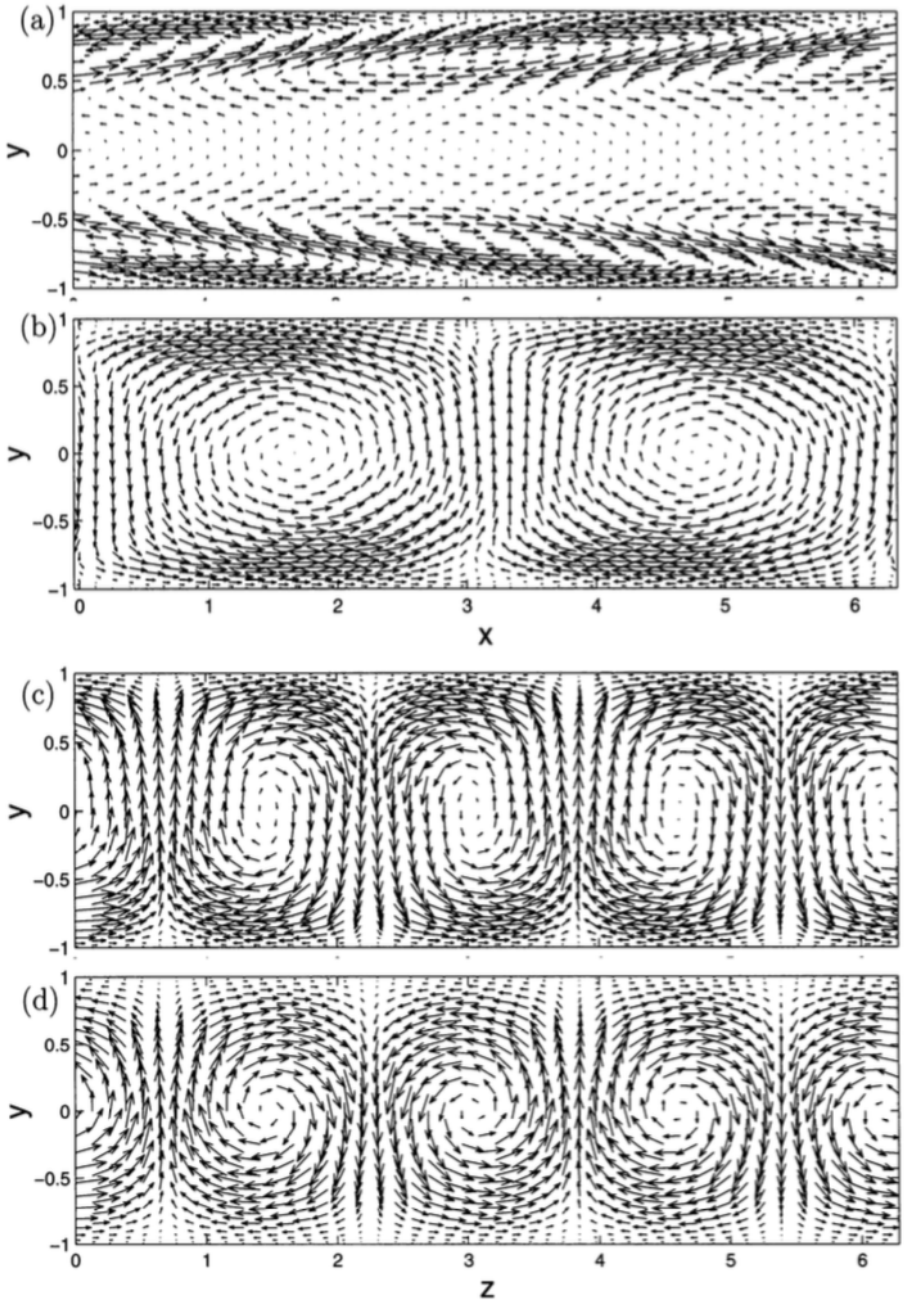

FIGURE 1.17 – Velocity field of optimal perturbations for plane Poiseuille flow. (a,b) Two-dimensional optimal initial conditions at $t = 0$ and response at $t = T$ due to Orr mechanism (spanwise uniform). (c,d) Three-dimensional optimal initial conditions at $t = 0$ and response at $t = T$ due to lift-up mechanism (streamwise uniform). Source : Schmid & Henningson (2001)

1.5.1 Orr mechanism

The Orr mechanism, also called Reynolds stress mechanism (Butler & Farrell 1992), is associated with a disturbance that can extract energy from mean shear through the Reynolds stress term. As shown in figure 1.17(a), with the effect of Orr mechanism, the optimal initial condition is titled against the mean shear at $t = 0$. As time evolves, the vortices are sheared by the mean flow and maximise the energy grow when it aligns in the cross-stream direction, as shown in figure 1.17(b) (Schmid & Henningson 2001).

1.5.2 Lift-up mechanism

Ellingsen & Palm (1975) demonstrated that a finite streamwise-uniform perturbation might lead to instability in a linear flow which has no inflexion point in the velocity profile. Even in an exponentially stable flow predicted by the modal stability analysis, the initial disturbance may undergo an important total perturbation energy growth. According to the linear theory, Landahl (1980) showed that such kind of transient growth appears in all inviscid parallel shear flows, and the kinetic energy of perturbation can grow at least linearly with time.

Gustavsson (1991) proved that the initial perturbations could determine the onset of transition to turbulence in plane Poiseuille flow, even if the flow is expected to be exponentially stable. Butler & Farrell (1992) and Reddy & Henningson (1993) later established that transient growth is important for the amplification of perturbations in a finite time interval. In some stable shear flows, the primary initial perturbations that maximise the energy growth is shown to be streamwise-uniform with non-zero wall normal velocity (Luchini 2000; Schmid 2007). For unstratified plane Poiseuille flow, as illustrated in figure 1.17(c,d), the streamwise vortices change little as time evolves. However, the streamwise velocity greatly grows in the process which will, in the end, lead to streaks in the fluid (Schmid & Henningson 2001).

This phenomenon is the physical representation of the lift-up mechanism (Ellingsen & Palm 1975; Landahl 1975), which is also called vortex tilting or vortex stretching process (Butler & Farrell 1992) because of the three-dimensional deformation.

1.5.3 Combination of Orr and lift-up mechanisms

The two mechanisms described above determines the optimal initial conditions as streamwise vortices (lift-up) or upstream tilting spanwise vortices (Orr). However, for short time intervals, the structures of the most amplified perturbations are titled roll vortices. Farrell & Ioannou (1993a) interpreted this phenomenon as combinations of the two fundamental mechanisms. Farrell & Ioannou (1993b) also showed that this three-dimensional structure is a universal character in shear flows and is consistent with the

result in Butler & Farrell (1992) and Butler & Farrell (1993). In the stratified fluid, Arratia (2011) also studied this synergy effect in the context of horizontal shear layers.

1.6 Motivation and purpose

As discussed in section 1.1.2, internal waves are ubiquitous and essential in nature. Thus, their generation mechanisms have drawn lots of research interest. The problem about the sources remains a debate in an extensive literature. Wu & Zhang (2008*b*) indicated that instability waves could generate internal waves if they approach a boundary. Le Dizès & Billant (2009) also demonstrated that the radiative instability can be associated with the emission of internal waves in stratified shear flows. Candelier *et al.* (2012) showed that the radiative instability is present in inviscid boundary layers when the shear direction is inclined relative to the stratification. It is reasonable to quantify the viscous effect on the radiative instability, and it is one of the major purposes of the present thesis. We also aim to evaluate the stratification effect on the transient growth, especially the effects on the related fundamental mechanisms.

In fluid mechanics, idealised models are widely used in theoretical and experimental researches to focus on the important aspects and elements. We use tanh velocity profile as a boundary layer and plane Poiseuille flow as a prototype of channel flow in our studies because of their simple configurations. Modal and non-modal analysis are both conducted in our studies. As one of the first prototypes for transient growth, unstratified plane Poiseuille flow is demonstrated to exhibit large transient growth in finite time intervals (Butler & Farrell 1992; Reddy & Henningson 1993). The basic mechanisms are revealed and classified in previous works (Farrell & Ioannou 1993*a*; Arratia 2011). It becomes natural to ask, what is the effects of vertical stratification on the transient growth ? Which mechanism is dominant in stratified flows ?

1.7 Summary of this thesis

The present thesis is composed of 5 chapters.

In chapter 1, basic concepts in stratified fluid have been introduced in a general way. The motivations and objectives of our study have been presented. We have also briefly introduced some well-known instabilities in parallel shear flows and stratified fluid : viscous instability, Kelvin-Helmholtz instability and the radiative instability. We have mostly focused on the viscous instability and the radiative instability in boundary layers. The concepts of both modal and non-modal stability analysis have been introduced and described. For the modal instability, we have discussed the over-reflection and resonance

phenomena, and for transient growth, we have reviewed the Orr mechanism, lift-up mechanism and the combination of both.

In chapter 2, the governing equations are derived, and the numerical method we used is introduced. We have solved the linearised Navier-Stokes equations under the Boussinesq approximation for the stratified flow. The pseudo-spectral method is used for the spatial discretization. We have also applied a complex path method. The transient growth is evaluated by the 'Direct-Adjoint-Loop' method, and the specific procedure is described in this chapter.

Chapter 3 contains the modal stability results of a boundary layer flow on a vertical wall in the presence of stratification. The viscous instability and radiative instability are compared for various Reynolds numbers and Froude numbers. The viscous effect on radiative instability is also exhibited in this part.

Chapter 4 reveals both the exponential and transient growth in stratified plane Poiseuille flow. The three-dimensional instability due to the resonance mechanism is investigated. The transient growth is computed for both long and short time intervals. The stratification effects on the fundamental mechanisms are examined to determine the dominate one.

Finally, some conclusions and perspectives are provided in chapter 5.

Chapitre 2

Method

In this chapter, the mathematical formulation of two models are derived : a plane Poiseuille flow between two vertical walls and a hyperbolic tangent boundary layer flow on one vertical wall. The fluid in both cases is uniformly stratified.

With the Boussinesq approximation, the governing equations for an incompressible viscous fluid are

$$\frac{\partial \boldsymbol{u}}{\partial t} = -(\boldsymbol{u}\cdot\nabla)\boldsymbol{u} - \frac{1}{\rho_0}\nabla p + \nu\Delta\boldsymbol{u} + \frac{\rho}{\rho_0}\boldsymbol{g}, \tag{2.1a}$$

$$\nabla\cdot\boldsymbol{u} = 0 \tag{2.1b}$$

where ν is the kinetic viscosity and $\boldsymbol{g}$ is the gravity. For a stratified flow, the density diffusion equation is

$$\frac{\partial \rho}{\partial t} + (\boldsymbol{u}\cdot\nabla)\rho = D\Delta\rho \tag{2.2}$$

where D is the mass diffusivity.

2.1 Base flow and perturbation equations

In this part we consider a horizontally directed flow of a viscous and stably stratified incompressible fluid in a vertical channel and on a wall, as sketched in figure 2.1. The stratification is assumed to be uniform with a constant buoyancy frequency

$$N = \sqrt{-\frac{g}{\rho_0}\frac{\partial\overline{\rho}}{\partial z}} \tag{2.3}$$

where g is gravity, ρ_0 is a characteristic value of the mean density $\overline{\rho}$.

In the channel, the base flow is assumed to be a parallel flow, i.e., a flow in x-direction that only depends on the wall-normal direction y (see figure 2.1 defining the coordinate system and base flow). Using the maximum velocity at the centre of the channel U and half the channel width L for non-dimensionalization, we define the base flow velocity field as

$$\overline{\boldsymbol{U}} = U_0(y)\boldsymbol{e_x} = (1-y^2)\boldsymbol{e_x}. \quad -1 \leqslant y \leqslant 1 \tag{2.4}$$

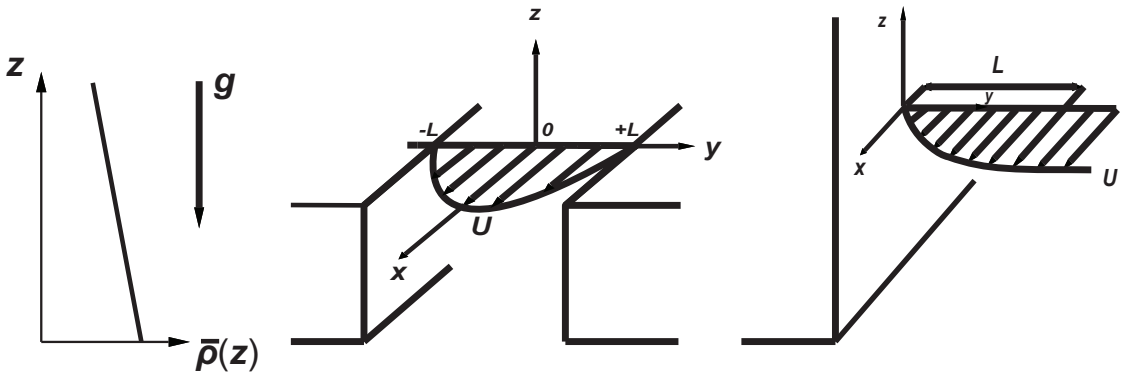

FIGURE 2.1 – Sketch of the base flow geometry and coordinate system

where $\boldsymbol{e_x}$ is the unit vector in the streamwise direction x. This base flow is the so-called plane Poiseuille flow.

For the boundary flow on a wall, we apply a local parallel-flow assumption and assume that the base flow velocity field is given by the tanh profile

$$\overline{\boldsymbol{u}} = U_0(y)\boldsymbol{e_x} = \tanh(y)\,\boldsymbol{e_x}. \tag{2.5}$$

where $\boldsymbol{e_x}$ is the unit vector in the streamwise direction x, and where we have used the main stream velocity U and the boundary layer thickness L to non-dimensionalize all the variables.

The characteristics of the base flow are defined by three parameters :

$$Re = \frac{UL}{\nu} \quad \text{The Reynolds number,} \tag{2.6a}$$

$$Sc = \frac{\nu}{D} \quad \text{The Schmidt number,} \tag{2.6b}$$

$$F = \frac{U}{NL} \quad \text{The Froude number,} \tag{2.6c}$$

where ν and D are the kinematic viscosity and the mass diffusivity of the fluid. In the present study, for the plane Poiseuille flow, the Schmidt number is set to $Sc = 1$. For the boundary layer flow, we assume $Sc = \infty$.

To study the stability of this flow, we consider a basic state $(\overline{U_i}, \overline{P}, \overline{\rho})$ and a perturbed state $(\overline{U_i} + u', \overline{P} + p', \overline{\rho} + \rho')$, both satisfying the Navier-Stokes equations (2.1) and the density diffusion equation (2.2). The expressions are

$$\boldsymbol{u}(\boldsymbol{x}, t) = \overline{\boldsymbol{U}} + \boldsymbol{u}'(\boldsymbol{x}, t), \tag{2.7a}$$

$$P(\boldsymbol{x}, t) = \overline{P} + p'(\boldsymbol{x}, t), \tag{2.7b}$$

$$\rho(\boldsymbol{x}, t) = \overline{\rho} + \rho'(\boldsymbol{x}, t) \tag{2.7c}$$

Under the Boussinesq approximation, the governing equations of this flow can be derived by introducing (2.4) (2.7) into the Navier-Stokes equations (2.1) and the density

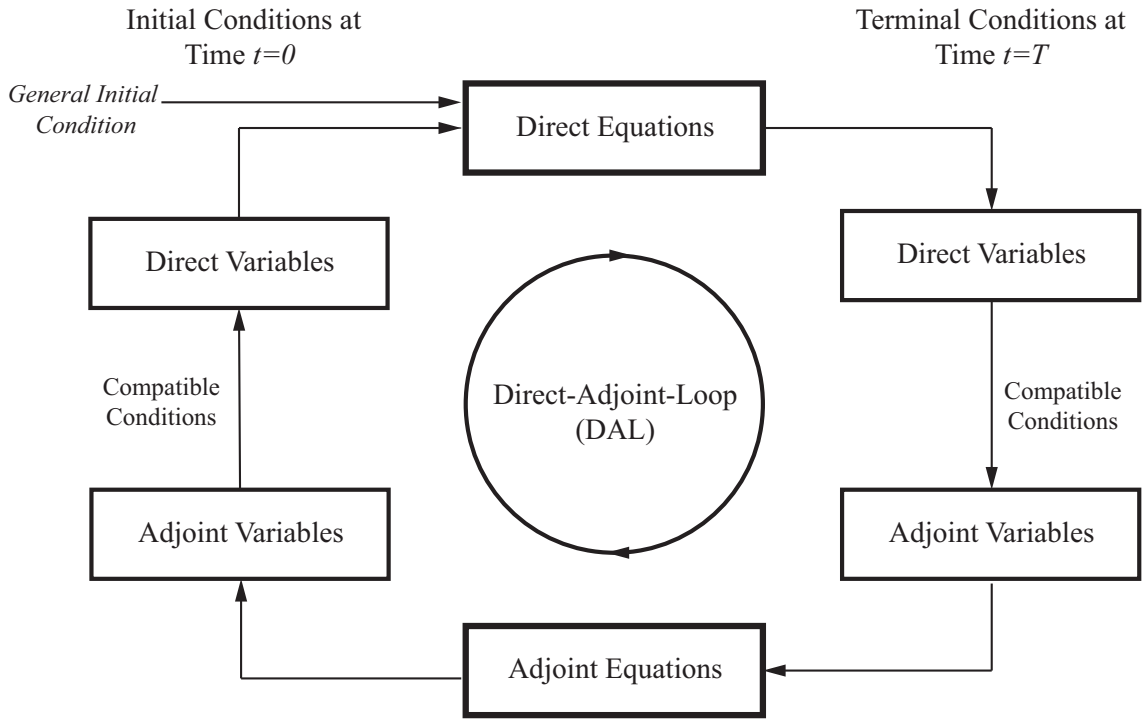

FIGURE 2.2 – Sketch of iterative procedure

diffusion equation (2.2)

$$\frac{\partial u'}{\partial t} = -U_0\frac{\partial u'}{\partial x} - \frac{dU_0}{dy}v' - \frac{\partial p'}{\partial x} + \frac{1}{Re}\Delta u', \tag{2.8a}$$

$$\frac{\partial v'}{\partial t} = -U_0\frac{\partial v'}{\partial x} - \frac{\partial p'}{\partial y} + \frac{1}{Re}\Delta v', \tag{2.8b}$$

$$\frac{\partial w'}{\partial t} = -U_0\frac{\partial w'}{\partial x} - \frac{\partial p'}{\partial z} + \frac{1}{Re}\Delta w' + \frac{b'}{F^2}, \tag{2.8c}$$

$$\frac{\partial b'}{\partial t} = -U_0\frac{\partial b'}{\partial x} + \frac{1}{ReSc}\Delta b' - w', \tag{2.8d}$$

$$0 = \frac{\partial u'}{\partial x} + \frac{\partial v'}{\partial y} + \frac{\partial w'}{\partial z} \tag{2.8e}$$

where $b' = \rho'/\partial_z\overline{\rho}$ and the nonlinear terms are neglected.

2.2 Optimal perturbations

The method of non-modal analysis is first introduced in this section. Optimal perturbation provides the initial conditions that excite the most energetic perturbation in a given base flow. Recently, Kaminski *et al.* (2014) analysed the transient growth in a strongly stratified shear layers depending on the now-conventional 'direct-adjoint looping' (DAL) method, which is summarised by Schmid (2007). We used a similar method for the non-modal analysis.

The application of adjoint equations has been developed significantly in the field of hydrodynamic stability theory (Luchini & Bottaro 2014). In the DAL method, it helps to

identify the optimal perturbations (Schmid 2007). Variational and optimisation techniques are incorporated in this method. The objective of the optimisation process is the total energy growth over a given time interval ($0 \leqslant t \leqslant T$), and the constraints are the governing equations, for example, the linearised Navier-Stokes equations, and boundary conditions and initial conditions.

The iterative procedure of 'direct-adjoint-loop' method is shown in figure 2.2. At the start of the loop in DAL method, a general initial perturbation for the 'direct' variables (mostly physical variables) is involved, and the 'direct' equations for the evolution are integrated forward from $t = 0$ to $t = T$. At time $t = T$, the total energy growth is evaluated, and the direct variables are converted to the adjoint variables as the terminal conditions for the 'adjoint' equations. Then the adjoint equations are subsequently integrated backward from $t = T$ to $t = 0$. At time $t = 0$, the adjoint variables are recovered to the direct ones and thus the new initial conditions for the direct problem are generated. This process is repeated until the initial perturbation converges to the optimal one and the total energy growth is maximised. It has become an essential purpose of transient growth analysis to evaluate the evolution and amplification quantitatively.

In this part, we introduce the DAL variational method in the context of stratified flows. The total perturbation energy $E(T)$ is defined as a sum of the kinetic energy and potential energy of the perturbation (2.9),

$$E = \frac{\langle \boldsymbol{u}', \boldsymbol{u}' \rangle}{2} + \frac{1}{2}\frac{\langle b', b' \rangle}{F^2} \tag{2.9}$$

where angled bracket denote an appropriate inner product, e.g. $\langle \boldsymbol{u}, \boldsymbol{v} \rangle \equiv \frac{1}{V}\int_V \boldsymbol{u} \cdot \boldsymbol{v} \mathrm{d}V$, and V is the domain volume. The weighted 2-norm in equation (2.9) is natural because in this way, the body force terms in equation (2.8c,d) can be cancelled in the expression

$$\frac{dE}{dt} = -\frac{1}{V}\int_V \left(\frac{dU_0}{dy} v'u' + \frac{1}{Re}\frac{|\nabla \boldsymbol{u}'|^2}{2} + \frac{1}{ReScF^2}\frac{|\nabla b'|^2}{2} \right) \mathrm{d}V \tag{2.10}$$

The boundary conditions in our model are applied to get this expression. In equation (2.10), the first term in the bracket is related to the Reynolds stress, and the other two positive definite terms are respectively associated with the dissipation of kinetic and potential energy.

The objective function of our optimisation procedure is the perturbation energy gain (2.11)

$$G(T) = \frac{E(T)}{E_0} \tag{2.11}$$

where

$$E_0 = \frac{\langle \boldsymbol{u}_0', \boldsymbol{u}_0' \rangle}{2} + \frac{1}{2}\frac{\langle b_0', b_0' \rangle}{F^2}.$$

Specifically, we search for the initial conditions $(\boldsymbol{u}_0'(\boldsymbol{x}), b_0'(\boldsymbol{x}), p_0'(\boldsymbol{x}))$ that can maximize the perturbation energy gain $G(T)$ over a finite time T.

The evolution of the initial perturbations is governed by (2.8). The objective functional is defined as

$$\begin{aligned}\mathscr{L} =&\frac{E(T)}{E(0)}\\ &-\left[\frac{\partial u_i'}{\partial t}+u_j'\frac{\partial \overline{U_i}}{\partial x_j}+\overline{U_j}\frac{\partial u_i'}{\partial x_j}+\frac{\partial p'}{\partial x_i}-\frac{1}{Re}\Delta u_i'-\frac{b}{F^2}\delta_{i3},\ u_i^A\right]\\ &-\left[\frac{\partial b'}{\partial t}+\overline{U_j}\frac{\partial b_i'}{\partial x_j}+u_i'\delta_{i3}-\frac{1}{ReSc}\Delta b',\ b^A\right]-\left[\frac{\partial u_i'}{\partial x_i},\ p^A\right]\\ &-\langle u_i'(0)-u_{0i}',\ u_{0i}^A\rangle-\langle b'(0)-b_0',\ b_0^A\rangle-\langle p'(0)-p_0',\ p_0^A\rangle\end{aligned} \tag{2.12}$$

where $[\boldsymbol{u},\ \boldsymbol{v}]\equiv\int_0^T\langle\boldsymbol{u},\boldsymbol{v}\rangle\mathrm{d}t$. The first term is the perturbation energy gain, and the penalty terms contain the constraints of governing equations (2.8) and the initial conditions of the flow at $t=0$. The Lagrange multipliers $(\boldsymbol{u}^A(\boldsymbol{x},t),b^A(\boldsymbol{x},t),p^A(\boldsymbol{x},t))$ represent the adjoint variables. The direct evolution equations, i.e. the linearised Navier-Stokes equations, continuity equation, and density distribution equation, can be recovered by taking variations of $\mathscr{L}$ with respect to the adjoint variables. Variations of $\mathscr{L}$ with respect to $(\boldsymbol{u}_0^A(\boldsymbol{x}),b_0^A(\boldsymbol{x}),p_0^A(\boldsymbol{x}))$ set the initial conditions $(\boldsymbol{u}_0'(\boldsymbol{x}),b_0'(\boldsymbol{x}),p_0'(\boldsymbol{x}))$ for the flow. The subscript '0' in these variables indicates that these quantities are the initial conditions at time $t=0$.

The adjoint equations, which describe the evolution of the adjoint variables, can be obtained by taking variations of (2.12) with respect to the direct (physical perturbation) variables $(\boldsymbol{u}',b',p')$, and setting the results equal to zero. These equations read

$$\frac{\partial u^A}{\partial t}=-U_0\frac{\partial u^A}{\partial x}-\frac{\partial p^A}{\partial x}-\frac{1}{Re}\Delta u^A, \tag{2.13a}$$

$$\frac{\partial v^A}{\partial t}=\frac{dU_0}{dy}u^A-U_0\frac{\partial v^A}{\partial x}-\frac{\partial p^A}{\partial y}-\frac{1}{Re}\Delta v^A, \tag{2.13b}$$

$$\frac{\partial w^A}{\partial t}=-U_0\frac{\partial w^A}{\partial x}-\frac{\partial p^A}{\partial z}-\frac{1}{Re}\Delta w^A+b^A, \tag{2.13c}$$

$$\frac{\partial b^A}{\partial t}=-U_0\frac{\partial b^A}{\partial x}-\frac{w^A}{F^2}-\frac{1}{ReSc}\Delta b^A, \tag{2.13d}$$

$$0=\frac{\partial u^A}{\partial x}+\frac{\partial v^A}{\partial y}+\frac{\partial w^A}{\partial z} \tag{2.13e}$$

The adjoint equations (2.13) must be satisfied for all times over the interval $[0,T]$, and should be well-posed when integrated backwards in time (Schmid 2007; Luchini & Bottaro 2014). Variations of (2.12) with respect to $(\boldsymbol{u}',b',p')$ can also give compatibility conditions, which represent the relationships between the direct variables $(\boldsymbol{u}',b',p')$ and the adjoint variables $(\boldsymbol{u}^A,b^A,p^A)$ at the target time T :

$$\left(\frac{u_i'}{E_0}-u_i^A\right)\bigg|_{t=T}=0, \tag{2.14a}$$

$$\left(\frac{b}{F^2E_0}-b^A\right)\bigg|_{t=T}=0 \tag{2.14b}$$

The variations of $\mathscr{L}$ with respect to the initial perturbations $(\boldsymbol{u}_0', b_0', p_0')$ should also be set as zero to maximize the objective functional (2.12). This functional can give the compatibility conditions that should be satisfied at the initial time $t = 0$:

$$\left(\frac{u_{0i}^A E_0^2}{E(T)} - u_{0i}'\right)\Big|_{t=0} = 0, \tag{2.15a}$$

$$\left(\frac{F^2 E_0^2 b_0^A}{E(T)} - b_0'\right)\Big|_{t=0} = 0 \tag{2.15b}$$

The perturbations can be further assumed to be in the form of

$$\boldsymbol{u}'(\boldsymbol{x}, t) = \boldsymbol{u}(y, t) e^{ik_x x + ik_z z}, \tag{2.16a}$$

$$b'(\boldsymbol{x}, t) = b(y, t) e^{ik_x x + ik_z z}, \tag{2.16b}$$

$$p'(\boldsymbol{x}, t) = p(y, t) e^{ik_x x + ik_z z} \tag{2.16c}$$

This form (2.16) is introduced into (2.8), the resulting equations can be written as :

$$\frac{\partial u}{\partial t} = -iU_0 k_x u - \frac{dU_0}{dy} v - ik_x p + \frac{1}{Re}\Delta_y u, \tag{2.17a}$$

$$\frac{\partial v}{\partial t} = -iU_0 k_x v - \frac{dp}{dy} + \frac{1}{Re}\Delta_y v, \tag{2.17b}$$

$$\frac{\partial w}{\partial t} = -iU_0 k_x w - ik_z p + \frac{b}{F^2} + \frac{1}{Re}\Delta_y w, \tag{2.17c}$$

$$\frac{\partial b}{\partial t} = -iU_0 k_x b - w + \frac{1}{ReSc}\Delta_y b, \tag{2.17d}$$

$$0 = ik_x u + \frac{dv}{dy} + ik_z w \tag{2.17e}$$

where

$$\Delta_y = \frac{d^2}{dy^2} - k_x^2 - k_z^2.$$

The corresponding adjoint equations are :

$$\frac{\partial u^A}{\partial t} = -iU_0 k_x u^A - ik_x p^A - \frac{1}{Re}\Delta_y u^A, \tag{2.18a}$$

$$\frac{\partial v^A}{\partial t} = \frac{dU_0}{dy} u^A - iU_0 k_x v^A - \frac{dp^A}{dy} - \frac{1}{Re}\Delta_y v^A, \tag{2.18b}$$

$$\frac{\partial w^A}{\partial t} = -iU_0 k_x w^A - ik_z p^A + b^A - \frac{1}{Re}\Delta_y w^A, \tag{2.18c}$$

$$\frac{\partial b^A}{\partial t} = -iU_0 k_x b^A - \frac{w^A}{F^2} - \frac{1}{ReSc}\Delta_y b^A, \tag{2.18d}$$

$$0 = ik_x u^A + \frac{dv^A}{dy} + ik_z w^A \tag{2.18e}$$

In the context of method described above, optimal perturbation is an initial configuration $(u_0, v_0, w_0, b_0, p_0)$ that can maximize the energy gain $G(T)$ at a prescribed terminal time $t = T$, for a given set of parameters (k_x, k_z, Re, F, Sc).

The optimal perturbations can be obtained by applying the iterative optimisation algorithm, which essentially relies on the power iteration method (Corbett & Bottaro 2000; Schmid 2007). The randomly initialized flow marches forward in time from $t = 0$ to $t = T$, satisfying the direct governing equations (2.17a-e). At time $t = T$, the initial adjoint variables are generated with the help of the direct physical variables and the compatibility conditions (2.14). Then the adjoint variables evolve backward in time with the adjoint equations (2.18a-e) until $t = 0$. The initial conditions can then be updated by adopting the direct variables and the compatibility conditions (2.15). Successive iterations can be scaled to ensure that their magnitudes remain reasonable. This procedure, which is the so-called 'direct-adjoint-loop', is repeated until the initial conditions converge to the optimal ones, and the energy gain $G(T)$ reaches its maxima. The typical convergence criterion is that the relative error of $G(T)$ is smaller than 10^{-3}.

In the iterative procedure, the evolutions in time are implemented with backward differentiation formula (BDF), which is a family of implicit multi-step method for numerical integration of ordinary differential equations, e.g.

$$\frac{\partial \boldsymbol{f}}{\partial t} = \boldsymbol{A}\boldsymbol{f}, \quad \boldsymbol{f} = (u, v, w, p, b)^T \tag{2.19}$$

Depending on the direct equations (2.17), we can get the matrix $\boldsymbol{A}$

$$\boldsymbol{A} = \begin{bmatrix} -ik_xU_0 + \frac{1}{Re}\Delta_y & -\frac{dU_0}{dy} & 0 & -ik_x & 0 \\ 0 & -ik_xU_0 + \frac{1}{Re}\Delta_y & 0 & -\frac{d}{dy} & 0 \\ 0 & 0 & -ik_xU_0 + \frac{1}{Re}\Delta_y & -ik_z & \frac{1}{F^2} \\ ik_x & \frac{d}{dy} & ik_z & 0 & 0 \\ 0 & 0 & -1 & 0 & -ik_xU_0 + \frac{1}{ReSc}\Delta_y \end{bmatrix}$$

Correspondingly, the matrix $\boldsymbol{A}^A$ for the adjoint equations (2.18) is

$$\boldsymbol{A}^A = \begin{bmatrix} -ik_xU_0 - \frac{1}{Re}\Delta_y & 0 & 0 & -ik_x & 0 \\ \frac{dU_0}{dy} & -ik_xU_0 - \frac{1}{Re}\Delta_y & 0 & -\frac{d}{dy} & 0 \\ 0 & 0 & -ik_xU_0 - \frac{1}{Re}\Delta_y & -ik_z & 1 \\ ik_x & \frac{d}{dy} & ik_z & 0 & 0 \\ 0 & 0 & -\frac{1}{F^2} & 0 & -ik_xU_0 - \frac{1}{ReSc}\Delta_y \end{bmatrix}$$

and the adjoint equation for (2.19) is

$$\frac{\partial \boldsymbol{f}^A}{\partial t} = \boldsymbol{A}^A\boldsymbol{f}^A, \quad \boldsymbol{f}^{\boldsymbol{A}} = (u^A, v^A, w^A, p^A, b^A)^T. \tag{2.20}$$

The specific formulas of s-step BDFs for the time integration are (Süli & Mayers 2003) :

$$\text{BDF1}: \quad \frac{\boldsymbol{f}_{n+1}-\boldsymbol{f}_n}{\Delta t}=\boldsymbol{A}\boldsymbol{f}_{n+1}$$

$$\text{BDF2}: \quad \frac{3\boldsymbol{f}_{n+2}-4\boldsymbol{f}_{n+1}+\boldsymbol{f}_n}{2\Delta t}=\boldsymbol{A}\boldsymbol{f}_{n+2},$$

$$\text{BDF3}: \quad \frac{11\boldsymbol{f}_{n+3}-18\boldsymbol{f}_{n+2}+9\boldsymbol{f}_{n+1}-2\boldsymbol{f}_n}{6\Delta t}=\boldsymbol{A}\boldsymbol{f}_{n+3}$$

$$\text{BDF4}: \quad \frac{25\boldsymbol{f}_{n+4}-48\boldsymbol{f}_{n+3}+36\boldsymbol{f}_{n+2}-16\boldsymbol{f}_{n+1}+3\boldsymbol{f}_n}{12\Delta t}=\boldsymbol{A}\boldsymbol{f}_{n+4}$$

$$\text{BDF5}: \quad \frac{137\boldsymbol{f}_{n+5}-300\boldsymbol{f}_{n+4}+300\boldsymbol{f}_{n+3}-200\boldsymbol{f}_{n+2}+75\boldsymbol{f}_{n+1}-12\boldsymbol{f}_n}{60\Delta t}=\boldsymbol{A}\boldsymbol{f}_{n+5}$$

$$\text{BDF6}: \quad \frac{147\boldsymbol{f}_{n+6}-360\boldsymbol{f}_{n+5}+450\boldsymbol{f}_{n+4}-400\boldsymbol{f}_{n+3}+225\boldsymbol{f}_{n+2}-72\boldsymbol{f}_{n+1}+10\boldsymbol{f}_n}{60\Delta t}=\boldsymbol{A}\boldsymbol{f}_{n+6}$$

where Δt is the step size and the s-step formula can achieve s-th order during computation. Typically, the formula BDF6 is used and the time step size in the present study is set as $\Delta t = 0.05$. However, for larger wavenumbers, a smaller step size should be used to avoid the numerical stability problem in time integration. In the present study, only the transient growth in plane Poiseuille flow is provided (see Chapter 4).

Spatial derivatives are computed with the pseudo-spectral method. We have applied Gauss-Lobatto points and Chebyshev polynomials for the plane Poiseuille flow (see section 2.3.1), and the collocation points of Laguerre polynomials for the boundary layer flow (see section 2.3.2).

2.3 Numerical method for eigenvalues

In this part, we provide the framework of linear temporal stability analysis of the base flow (2.4). The perturbations are searched in the form of normal modes

$$(u', v', w', p', b') = (u(y), v(y), w(y), p(y), F^2 b(y)) e^{ik_x x + ik_z z - i\omega t} \tag{2.21}$$

where k_x and k_z are real wavenumbers and ω the complex frequency ($\omega = \omega_r + i\omega_i$). The equations for (u, v, w, p, b) can be obtained by substituting (2.21) into (2.8)

$$-i\omega u = -iU_0 k_x u - \frac{dU_0}{dy} v - ik_x p + \frac{1}{Re}\Delta_y u, \tag{2.22a}$$

$$-i\omega v = -iU_0 k_x v - \frac{dp}{dy} + \frac{1}{Re}\Delta_y v, \tag{2.22b}$$

$$-i\omega w = -iU_0 k_x w - ik_z p + b + \frac{1}{Re}\Delta_y w, \tag{2.22c}$$

$$-i\omega b = -iU_0 k_x b - \frac{w}{F^2} + \frac{1}{ReSc}\Delta_y b, \tag{2.22d}$$

$$0 = ik_x u + \frac{dv}{dy} + ik_z w \tag{2.22e}$$

where

$$\Delta_y = \frac{d^2}{dy^2} - k_x^2 - k_z^2.$$

The equation system (2.22) is solved numerically using a pseudo-spectral method. A generalised problem

$$\boldsymbol{A}\boldsymbol{f} = \omega \boldsymbol{B}\boldsymbol{f}, \quad \boldsymbol{f} = (u, v, w, p, b)^T \tag{2.23}$$

can be derived from (2.22) and then be solved with the help of several subroutines in Matlab©.

2.3.1 Eigenvalues for plane Poiseuille flow

For the plane Poiseuille flow, the boundary conditions for (2.22) are set as non-slip boundary conditions

$$u(\pm 1) = v(\pm 1) = w(\pm 1) = 0.$$

The equation (2.23) is solved using Gauss-Lobatto points and Chebyshev polynomials. The advantage of Chebyshev polynomials in solving hydrodynamic stability problems is verified by Orszag (1971). Typically, the number of the points used in the present study is 100.

Illustration of the spectrum associated with (2.22) is shown in figure 2.3. This figure can be compared to the result of figure 3.1 (page 64) in Schmid & Henningson (2001). The three main branches of Orr-Sommerfeld modes (the eigenvalues of Orr-Sommerfeld equations), which have been label A ($\omega_r \to 0$), S ($\omega_r \approx 0.67$), P ($\omega_r \to 1$) by Mack (1976), are all included in figure 2.3. In addition to those Orr-Sommerfeld modes, an extra branch of Squire modes (the eigenvalues of Squire equation) also exists, which is located between the smaller branches of A modes. There is one slightly unstable eigenvalue ($\omega_i > 0$) on the A branch in figure 2.3, $\omega = 0.2375 + 0.00374i$, and this value exactly agrees with the 'accurate' solution of Orszag (1971). This unstable mode roots in the destabilising effects of viscosity, and is the so-called TS wave. The eigenfunctions associated with this mode are displayed in figure 2.4. The largest variations of velocities are close to the boundaries, and the pressure is the smallest ($p(0) = 0$) at the centre.

2.3.2 Eigenvalues for boundary layer flow

In our study of boundary layer flow, the choice of a tanh profile (instead of a Blasius profile) has been made for numerical convenience. Both the viscous and the radiative instabilities that we discuss here are expected to be weakly sensitive to the details of the profile (as long as it remains non-inflectional). In the very large Reynolds number limit, it is indeed known that the characteristics of these instabilities only depend on the velocity

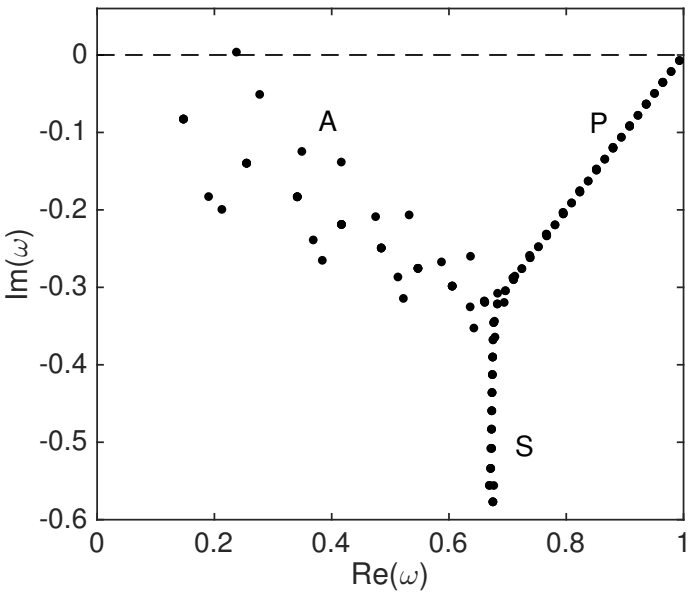

FIGURE 2.3 – Eigenvalues of unstratified ($F = \infty$) plane Poiseuille flow for $Re = 10^4, k_x = 1, k_z = 0$. The eigenvalue with a positive imaginary part is $\omega = 0.2375 + 0.00374i$.

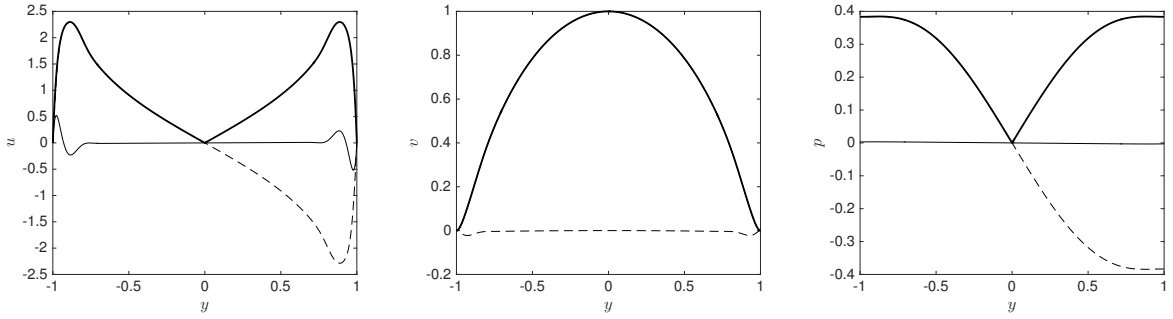

(a) (b) (c)

FIGURE 2.4 – Eigenfunctions for plane Poiseuille flow with $Re = 10^4$, $F = \infty$, $k_x = 1$, $k_z = 0$, $\omega = 0.2375 + 0.00374i$. (a) streamwise velocity ; (b) normal velocity ; (c) pressure. The thick solid lines represent the magnitude (absolute values), the thin solid lines and dashed lines are the real part and imaginary part, respectively. All the eigenfunctions are normalized by $v(0)$.

derivatives at the boundary (see Drazin & Reid (1981) for the viscous instability and Candelier *et al.* (2012) for the radiative instability).

In the present study, the Froude and Reynolds numbers are varied in the intervals

$$100 < Re < 10^7 \ , \quad 0.01 < F < 20. \tag{2.24}$$

We neglect the diffusion of mass and set $Sc = \infty$. This hypothesis is valid for salty water, for which Sc is around 700.

The goal of the present study is to perform a linear temporal stability analysis of the base flow (2.5). Perturbations are then searched in the form of normal modes. The velocity, pressure and buoyancy amplitudes (u, v, w, p, b) satisfy the equation system (2.22a-e)

obtained by linearising the Navier-Stokes and density equations under the Boussinesq approximation.

The no-slip boundary condition gives $u(0) = v(0) = w(0) = 0$. Far away from the boundary, we apply a condition of radiation which prescribes that the energy should propagate outward.

The system (2.22a-e) is discretized using a pseudo-spectral method on the collocation points of Laguerre polynomials. These polynomials are well-adapted to semi-infinite domain $[0, +\infty[$. This method has already been used in Riedinger *et al.* (2010*b*) and Candelier *et al.* (2012). The system of equations is then transformed into a generalized eigenvalue problem (2.23), which is solved using subroutines of Matlab©.

The eigenfunctions obtained by this method automatically vanish at infinity. As already explained by Riedinger *et al.* (2010*b*), this is not an adequate behaviour for all the physical perturbations.

By considering (2.22) for large y, it is easy to show that all solutions to (2.22) are, for large y, a sum of exponentials $e^{i\beta z}$ with $\Lambda = k_x^2 + k_z^2 + \beta^2$ satisfying

$$(\Lambda - i(\omega - k_x)Re)\left[i(\Lambda - k_z^2)Re - \Lambda F^2(\omega - k_x)\left(\Lambda - i(\omega - k_x)Re\right)\right] = 0. \qquad (2.25)$$

The condition of radiation prescribes that the solution should expend at infinity on 3 exponentials among the 6 possible (only the exponentials corresponding to waves propagating energy outward are kept). When $\mathrm{Im}(\omega) > 0$, this condition of radiation is equivalent to discarding the growing exponentials and keeping the decreasing exponentials. It is therefore equivalent to the vanishing of the solution at infinity. This implies that all unstable modes can a priori be captured by the spectral code. When $\mathrm{Im}(\omega) = 0$ or $\mathrm{Im}(\omega) < 0$, the conditions of radiation and of vanishing do not necessarily match. There are large regions of the complex ω plane where these two conditions are not equivalent. In these regions, the modes obtained by the spectral code are therefore "unphysical". The boundaries of these regions correspond to curves in the ω plane where one of the wavenumber β satisfying (2.25) becomes real. These curves are the so-called continuous spectrum. An illustration showing the numerical spectrum and the continuous spectrum is displayed in figure 2.5(a) for a typical example.

In figure 2.5, we have indicated, by a dashed rectangle, the region of the ω plane where the interesting eigenvalues corresponding to the radiative instability are expected. This region is very close to the continuous spectrum, which means that the eigenfunctions decay slowly at infinity.

As explained in Riedinger *et al.* (2010*b*), the exponentially decreasing behaviour of the solution can be improved by introducing a complex mapping $z = z'e^{i\alpha}$ where α is a fixed positive angle. The mapping of the complex path is shown in figure 2.6(a). Such a mapping modifies an oscillating behaviour on the z variable, say $e^{i\beta z}$ with $\beta > 0$ into an

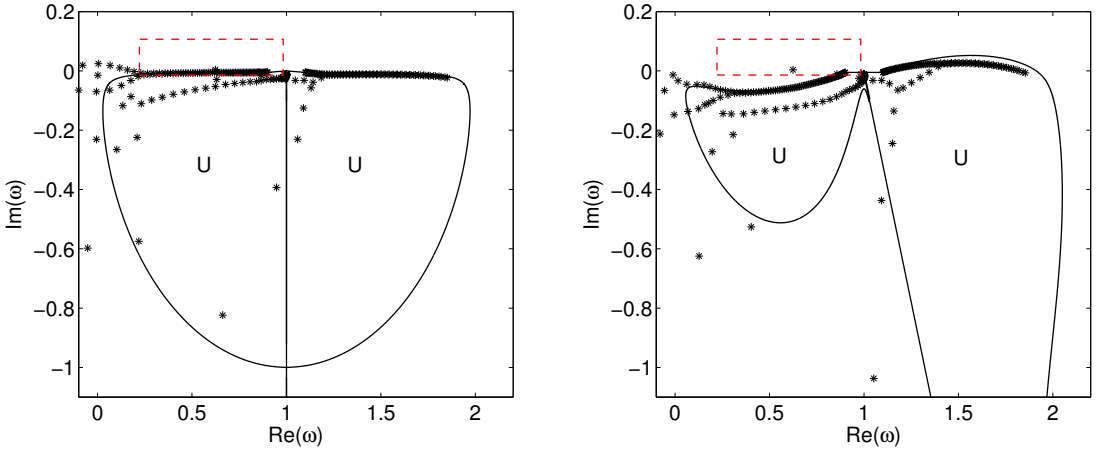

(a) (b)

FIGURE 2.5 – Continuous spectrum (solid lines) and numerical eigenvalues (stars) for $N = 100$ and the parameters $Re = 10^4$, $F = 1$, $k_x = 1$, $k_z = 10$. The 'unphysical' domain is indicated by the letter 'U'. (a) Integration on the real axis ($\alpha = 0$) ; (b) Integration on a complex path $z' = ze^{-i\alpha}$ with $\alpha = \pi/20$. The eigenvalue domain of interest is indicated by the dashed rectangle.

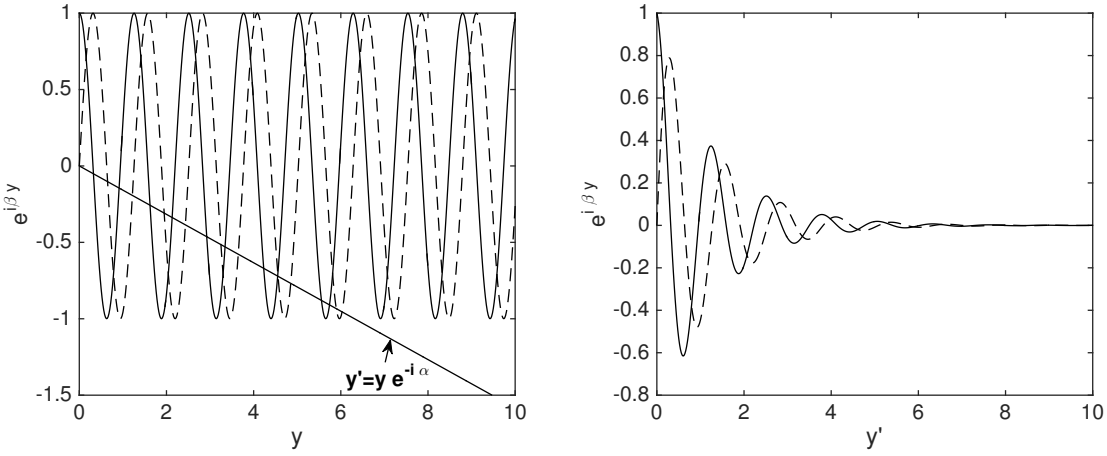

(a) (b)

FIGURE 2.6 – Application of complex path. (a) Oscillating behaviour of $e^{i\beta y}$ and complex path $y' = ye^{-i\alpha}$. (b) Exponential decreasing behaviour $e^{i\beta y' \cos\alpha} e^{-\beta y' \sin\alpha}$ (modified $e^{i\beta y}$) on the y' variable. The parameters used for these two figures are $\beta = 1$ and $\alpha = \pi/20$. The thin solid lines and dashed lines are the real part and imaginary part of the solutions.

exponential decreasing behaviour $e^{i\beta \cos\alpha z'} e^{-\beta \sin\alpha z'}$ on the z' variable. The modification effects on $e^{i\beta z}$ with $\beta > 0$ is illustrated in figure 2.6(b) as an example. The mapping thus modifies the spectrum and the continuous spectrum as shown in figure 2.5(b). Meanwhile, the physically relevant eigenvalue is not modified by the use of the complex path. The unstable mode in the dashed rectangle is now further away from the continuous spectrum curve. Being localized nearer to the origin, this mode is more easily resolved by the pseudo-spectral code. Neutral eigenvalues as well as weakly damped eigenvalues can also be captured by this method.

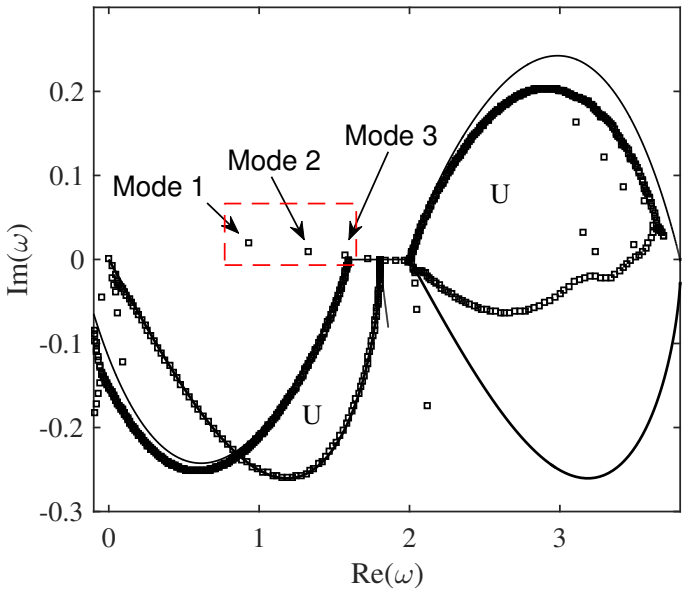

(a)

FIGURE 2.7 – Continuous spectrum (solid lines) and numerical eigenvalues (stars) for $N = 320$ and the parameters $Re = 10^7$, $F = 0.5$, $k_x = 1.8$, $k_z = 15.76$. The 'unphysical' domain is indicated by the letter 'U'. Integration on a complex path $z' = ze^{-i\alpha}$ with $\alpha = \pi/10$. The eigenvalue domain of interest is indicated by the dashed rectangle. Three different radiative modes are indicated by the arrows.

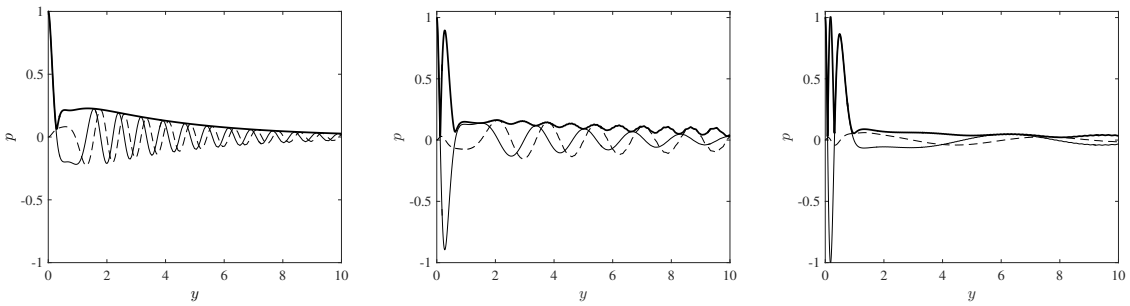

(a) (b) (c)

FIGURE 2.8 – Pressure eigenfunction of distinguished radiative modes for $Re = 10^7$, $F = 0.5$, $k_x = 1.8$, $k_z = 15.76$ (corresponding to the three modes in figure 2.7 but with $\alpha = 0$). (a) Mode 1 (most unstable), $\omega = 0.928 + 0.0209i$; (b) Mode 2, $\omega = 1.33 + 0.00957i$; (c) Mode 3, $\omega = 1.567 + 0.00488i$. Thick solid lines, solid lines and dashed lines represent absolute value, real part and imaginary part, respectively.

For a given set of parameters (k_x, k_z, Re, F), there may exist several radiative modes, for example, the eigenvalues shown in figure 2.7. The pressures eigenfunctions for the corresponding radiative modes (Mode 1, 2, 3) are displayed in figure 2.8. All modes exhibit a well-defined localised structure close to the wall and an oscillating structure faraway. The higher the mode, the more complex the localised structure close to the wall and the larger the wavelength in the radiative zone. In the following, we mainly focus on the first mode, which has both the simplest wall structure and the largest growth rate.

As soon as an eigenvalue is obtained, its robustness is tested by varying the angle α and the number N of polynomials. We have typically used $\alpha = \pi/20$ and $N = 100$.

Chapitre 3

Instability of a boundary layer flow on a vertical wall in a stably stratified fluid

(This chapter is based on the article Chen, J., Bai, Y., & Le Dizès, S. 2016 Instability of a boundary layer flow on a vertical wall in a stably stratified fluid. *J. Fluid Mech.* **795**, 262–277.)

3.1 Introduction

Boundary layers are ubiquitous in any flow close to boundaries. They are known to be unstable with respect to viscous instabilities for Reynolds numbers above a few thousands. In the presence of a stable stratification, such a flow on a vertical wall is shown to be unstable with respect to a stronger instability associated with the emission of internal gravity waves. The goal of the present chapter is to analyse the competition between both instabilities for a simple model of boundary layer flow as a function of viscosity and stratification strength.

The stability of boundary layer flows is a subject almost as old as fluid mechanics, which is covered by several textbooks (e.g. Betchov & Criminale 1967). In particular, it is well-established that an inflection-free boundary layer profile is unstable with respect to a 2D viscous instability that gives rise to the so-called Tollmien-Schlichting (TS) waves.

The effect of a stable stratification has been mainly studied in the context of atmospheric flows on flat horizontal surfaces (see Mahrt 2014, for a review). However, in this context, the velocity profile usually exhibits an inflectional point which makes it unstable with respect to the Kelvin-Helmholtz instability. This instability is modified by stratification as shown in Howard (1961); Miles (1961); Churilov (2005, 2008); Candelier *et al.* (2011). The effect of stratification on Tollmien-Schlichting waves is less known. It was studied experimentally in Ohya & Uchida (2003). Wu & Zhang (2008*a*) also demonstrated

that it could be destabilizing. On a vertical wall, the 2D Tollmien-Schlichting waves are not expected to be affected by stratification. But as Squire theorem is not applicable in the presence of stratification, more unstable 3D TS waves could a priori exist.

The inclination of shear with respect to the direction of stratification is also known to be a source of instability. Candelier *et al.* (2012) showed that an inflection-free boundary layer profile becomes unstable with respect to an inviscid "radiative instability" as soon as there is an angle between the directions of shear and stratification, the instability being the strongest for an angle of $\pi/2$, that is for a vertical wall. This instability which results from the coupling between shear and internal waves has been obtained in other contexts : shallow water flows (Satomura 1981; Balmforth 1999; Riedinger & Gilbert 2014), compressible flows (Mack 1990; Parras & Le Dizès 2010), rotating flows (Riedinger *et al.* 2010*b*, 2011). It has often been associated with a phenomenon of resonant over-reflection (McIntyre & Weissman 1978; Grimshaw 1979; Lindzen & Barker 1985), negative energy waves (Kópev & Leontev 1983), or spontaneous wave emission (Plougonven & Zeitlin 2002; Le Dizès & Billant 2009). In the present work, we shall analyse the effect of viscosity on the radiative instability of a boundary layer.

This chapter is organized as follows. In section 3.2.1, we first analyse the effect of stratification on the viscous instability, and then, in section 3.2.2, we study the radiative instability in the presence of viscosity. In section 3.2.3, we provide a summary of the stability results. The last section (section 3.3) is a brief discussion in the context of applications.

3.2 Temporal stability results

3.2.1 Boundary layer instability (Tollmien-Schlichting waves)

Considering a boundary layer flow, the viscous instability associated with Tollmien-Schlichting waves is expected to be active. Without stratification ($F = \infty$), the viscous instability of a boundary layer profile has been known for a long time (see for instance Betchov & Criminale 1967). In that case, Squire's theorem is applicable : the most unstable mode among all the possible wavenumbers k_x and k_z is obtained for $k_z = 0$. Being 2D without variation in the stratification direction y, this mode is also expected to exist in the presence of stratification, as the equations for the transverse velocity v and the buoyancy b are decoupled from the other velocity components and the pressure. However, there is no Squire theorem which guarantees that this 2D mode remains the most unstable in the presence of stratification.

The effect of the Froude number on the growth rate curve in the (k_x, k_z) plane is illustrated in figure 3.1. In these plots, we do see that for a given Reynolds number, the instability domain associated with the viscous instability grows as the stratification

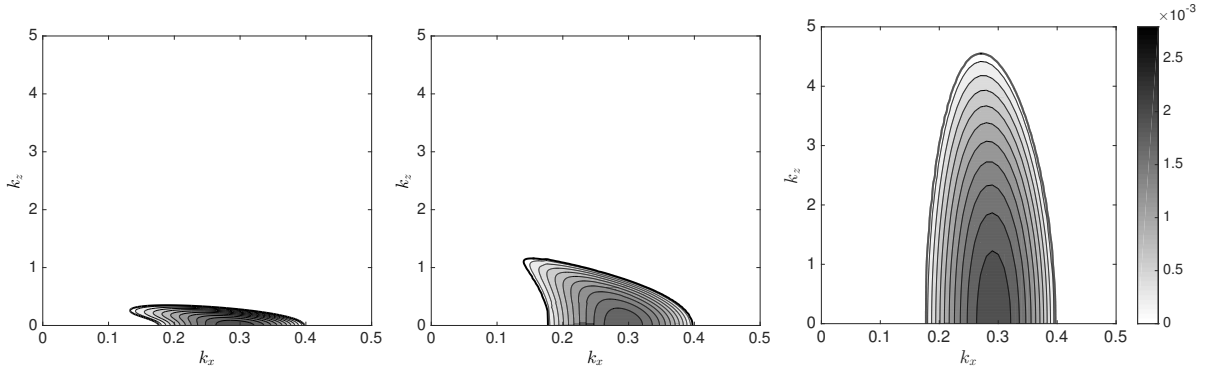

FIGURE 3.1 – Growth rate contours of the viscous instability in the (k_x, k_z) plane for $Re = 10^4$ and different Froude numbers. (a) $F = \infty$ (unstratified case) ; (b) $F = 1$; (c) $F = 0.1$. Contours are every 0.00025 from 0 to 0.0028.

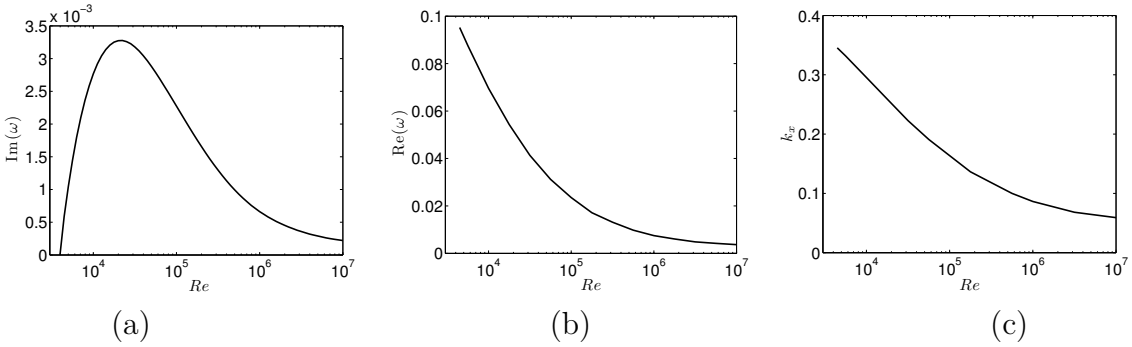

FIGURE 3.2 – Characteristics of the most unstable TS wave as a function of Re. (a) Growth rate $\mathrm{Im}(\omega)$; (b) Oscillation frequency $\mathrm{Re}(\omega)$; (c) Wavenumber k_x.

increases while the largest growth rate in this (k_x, k_z) domain is still reached for $k_z = 0$. We have tried other values of the Reynolds number, and always obtained that the most unstable Tollmien-Schlichting wave among all the possible wavenumbers k_x and k_z remains 2D whatever the Froude number. Since this mode does not depend on F, it means that its characteristics are not affected by the stratification. The characteristics of the most unstable Tollmien-Schliching wave are therefore independent of the stratification. They are shown in figure 3.2 as a function of the Reynolds number. The critical Reynolds number is found to be $Re_c^{(v)} \approx 3981$ for which the critical Tollmien-Schlichting wave has the characteristics : $k_x = 0.35$, $\omega = 0.1$. The growth rate decreases for large Reynolds numbers. It reaches its maximum at the most dangerous Reynolds number $Re_m^{(v)} \approx 22390$ for the most dangerous mode of characteristics $k_x = 0.13$, $\omega = 0.016 + 0.0033i$.

The eigenfunctions of the critical and most dangerous Tollmien-Schlichting waves are presented in figure 3.3. Note that the eigenfunctions of both modes are very similar. The only noticeable difference is the stronger localization of the critical mode close to the boundary. This can be related to the streamwise wavenumber difference and the behavior in $e^{-k_x y}$ of the eigenfunctions far from the boundary.

The evidence that Squire's theorem is not applicable in the presence of stratification

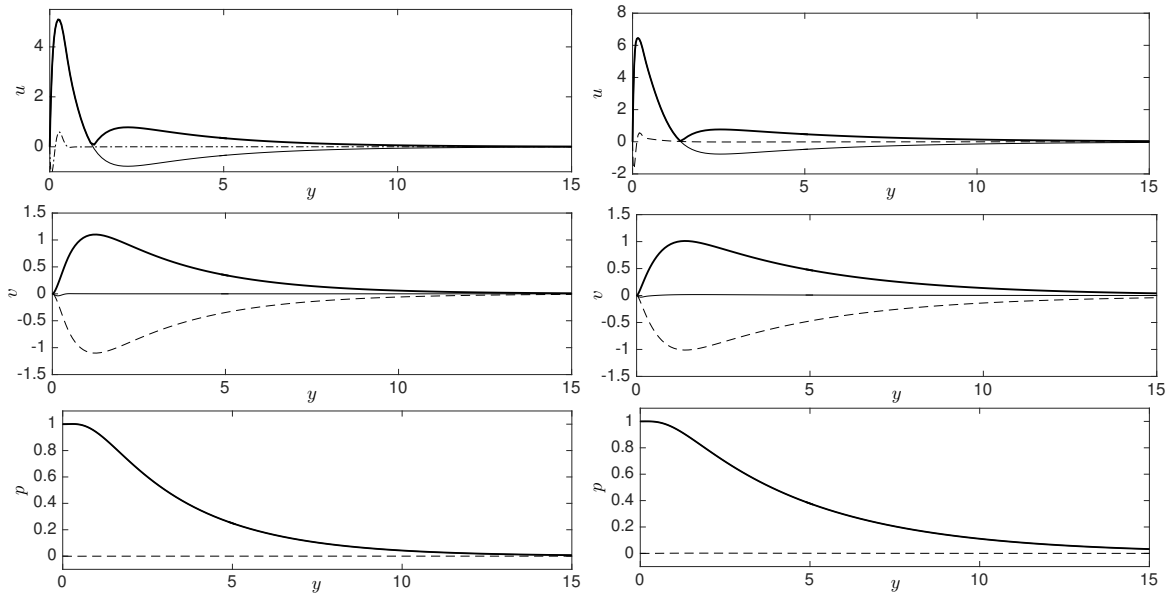

FIGURE 3.3 – Eigenfunctions of the most unstable TS wave (top : streamwise velocity u ; middle : normal velocity w ; bottom : pressure p) for the critical Reynolds number $Re = Re_c^{(v)} \approx 3981$ (left) and the most dangerous Reynolds number $Re = Re_m^{(v)} \approx 22390$ (right). Thick solid lines, solid lines and dashed lines represent absolute value, real part and imaginary part, respectively.

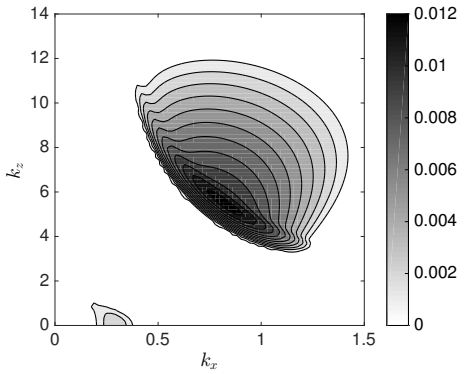

FIGURE 3.4 – Growth rate contours in the (k_x, k_z) plane for $Re = 10^4$ and $F = 1$ [enlarged view of figure 3.1(b)]. The two regions correspond to the viscous and radiative instability respectively. Contours are every 0.001 from 0.001 to 0.012.

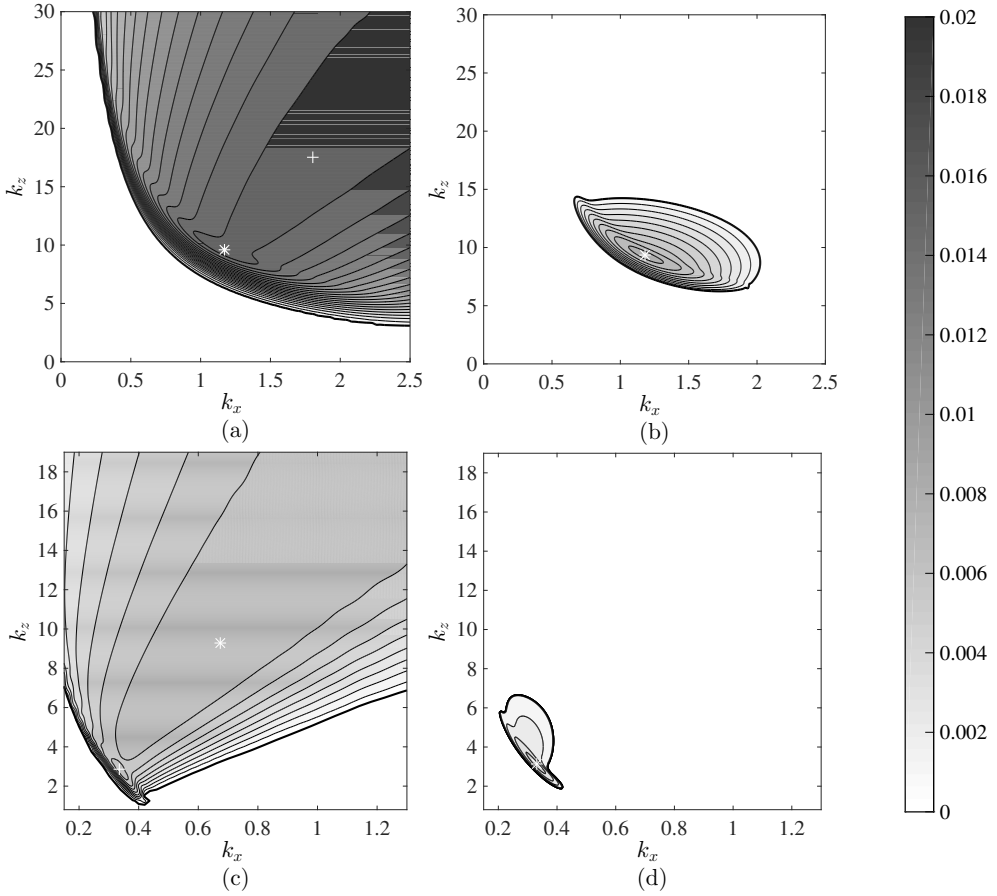

FIGURE 3.5 – Growth rate contours of the radiative mode in the (k_x, k_z) plane for several sets of Froude and Reynolds numbers. (a) $Re = 10^7$, $F = 0.5$; (b) $Re = 10^4$, $F = 0.5$; (c) $Re = 10^7$, $F = 3$; (d) $Re = 10^4$, $F = 3$. White crosses indicate local maxima of the growth rate, the largest maximum being shown with an asterisk. Contours are every 0.001 from 0.001 to 0.02.

is given in figure 3.4 which is an extension in a larger (k_x, k_z) domain of the growth rate contours. We clearly see the presence of 3D modes which are more unstable than all the 2D modes. These 3D unstable modes are associated with another instability, the so-called radiative instability, analysed in the next section.

3.2.2 Radiative instability

The radiative instability is inviscid in nature and results from the coupling between shear and internal gravity waves associated with the fluid stratification. The inviscid characteristics of this instability have been obtained for the tanh boundary layer profile in Candelier *et al.* (2012).

In figure 3.5, we have plotted the growth rate of the (most unstable) radiative mode in the (k_x, k_z) plane for various Froude and Reynolds numbers (Several unstable radiative modes may exist for a given set of parameters (k_x, k_z, Re, F). We always keep the mode with the largest growth rate even if we do not systematically mention that it is the most unstable radiative mode). We clearly see that viscous effects reduce the domain of

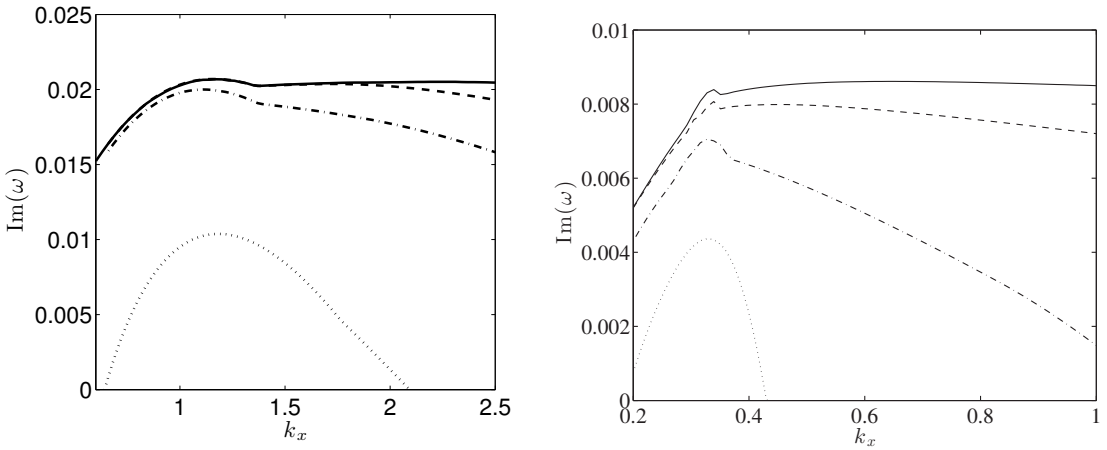

(a) (b)

FIGURE 3.6 – Maximum growth rate $\max_{k_z}[\mathrm{Im}(\omega)]$ of the radiative modes versus k_x for $F = 0.5$ (a) and $F = 3$ (b). Solid line : $Re = 10^7$, Dashed line : $Re = 10^6$, Dash-dot line : $Re = 10^5$, Dotted line : $Re = 10^4$.

instability. In the inviscid limit, the maximum growth rate is obtained for infinite k_x and k_z (Candelier *et al.* 2012). As soon as viscous effects are present, the maximum growth rate is reached for finite k_x and finite k_z. In figure 3.6, we have plotted the maximal value of the growth rate over all k_z as a function of k_x for various Reynolds numbers and $F = 0.5$ and 3. The viscous damping of higher wave numbers is also clearly seen on these plots. It should be noticed that there are the two local peaks of the growth rate curve for $Re = 10^6$ and 10^7. These peaks have also been indicated by symbols in figure 3.5(a,c). While the first peak remains almost fixed, the location of the second peak strongly varies with Reynolds number. This strong variation can be associated with the extremely broad character of this peak and the fact that it goes to infinity as $Re \to \infty$.

In figure 3.7, we have plotted the characteristics of the most unstable radiative mode (growth rate maximized over all the possible wavenumbers (k_x, k_z)) as a function of the Froude number for different Reynolds numbers. As expected, viscous results tend to inviscid results as Re increases. Note however that the convergence is slow, especially for small Froude numbers. This can be explained by the fact that even for $Re = 10^7$, the most unstable wavenumbers are still of order 1 (Remember, they should go to infinity in the inviscid limit). For this Reynolds number, the most unstable wavenumbers correspond to the first peak of the growth rate curve in the (k_x, k_z) plane for all Froude number $F < 1$ [see figure 3.5(a)]. It jumps to the second local peak of larger wavenumbers for higher Reynolds numbers, or for larger Froude numbers [see figure 3.5(c)]. This change of modes as Froude or Reynolds number increases generates the jump observed in figure 3.7(c-f).

The results for the radiative instability are summarized in figure 3.8. In this figure, we have displayed the characteristics of the most unstable radiative mode as a function of both parameters Re and F. Only the growth rate contours are expected to be smoothed. Frequency, wavenumbers and phase velocities exhibit discontinuities which are associated

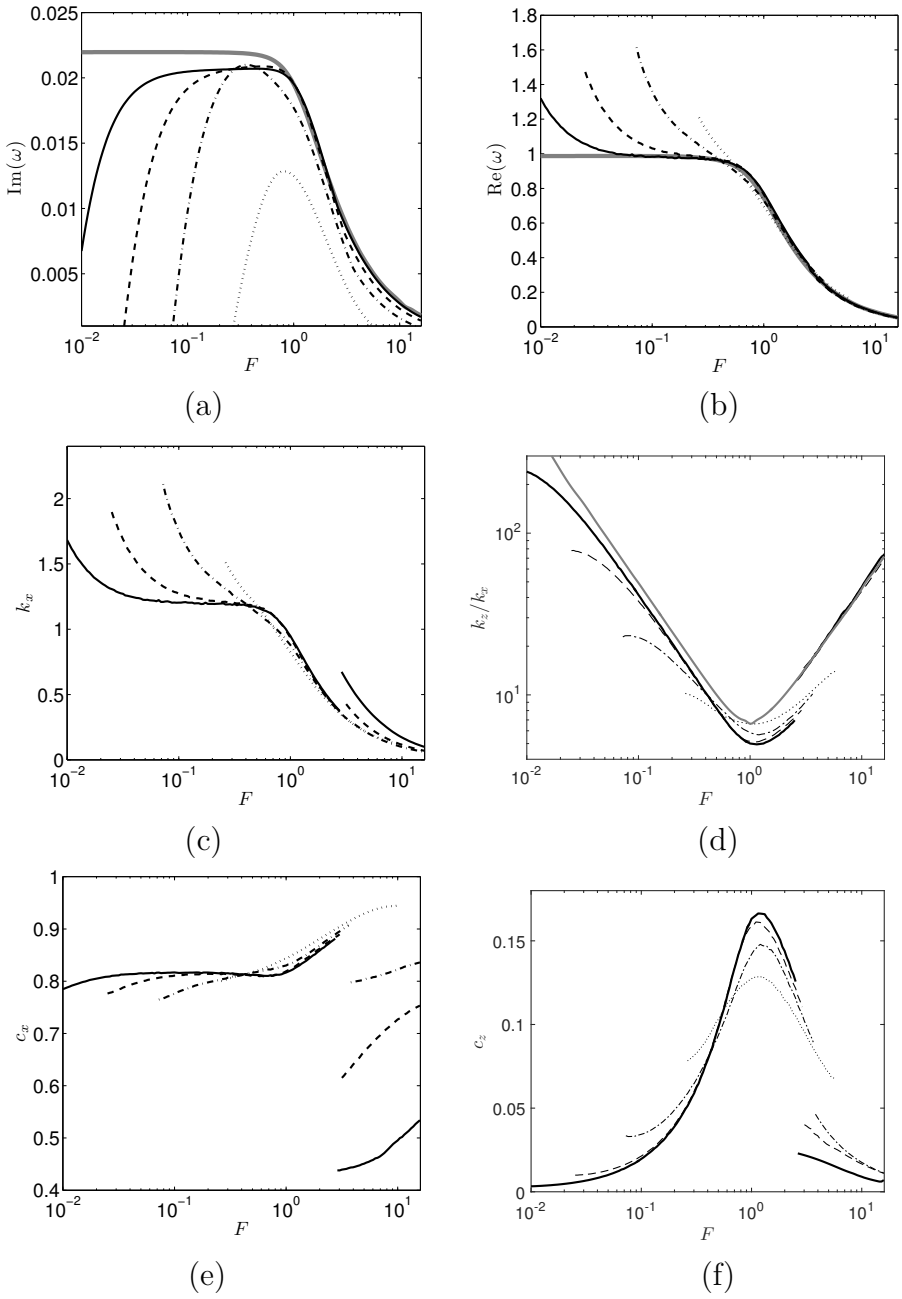

FIGURE 3.7 – Characteristics of the most unstable radiative mode (obtained by maximizing the growth rate over all k_x and k_z) as a function of the Froude number F for different Reynolds numbers. $Re = 10^4$ (dotted line), 10^5 (dash-dot line), 10^6 (dashed line), 10^7 (solid line), ∞ (thick grey line). (a) Growth rate $\mathrm{Im}(\omega)$; (b) Oscillation frequency $\mathrm{Re}(\omega)$; (c) Streamwise wavenumber k_x ; (d) Wavenumber ratio k_z/k_x ; (e) Phase velocity $\mathrm{Re}(\omega)/k_x$ along x ; (f) Phase velocity $\mathrm{Re}(\omega)/k_z$ along z.

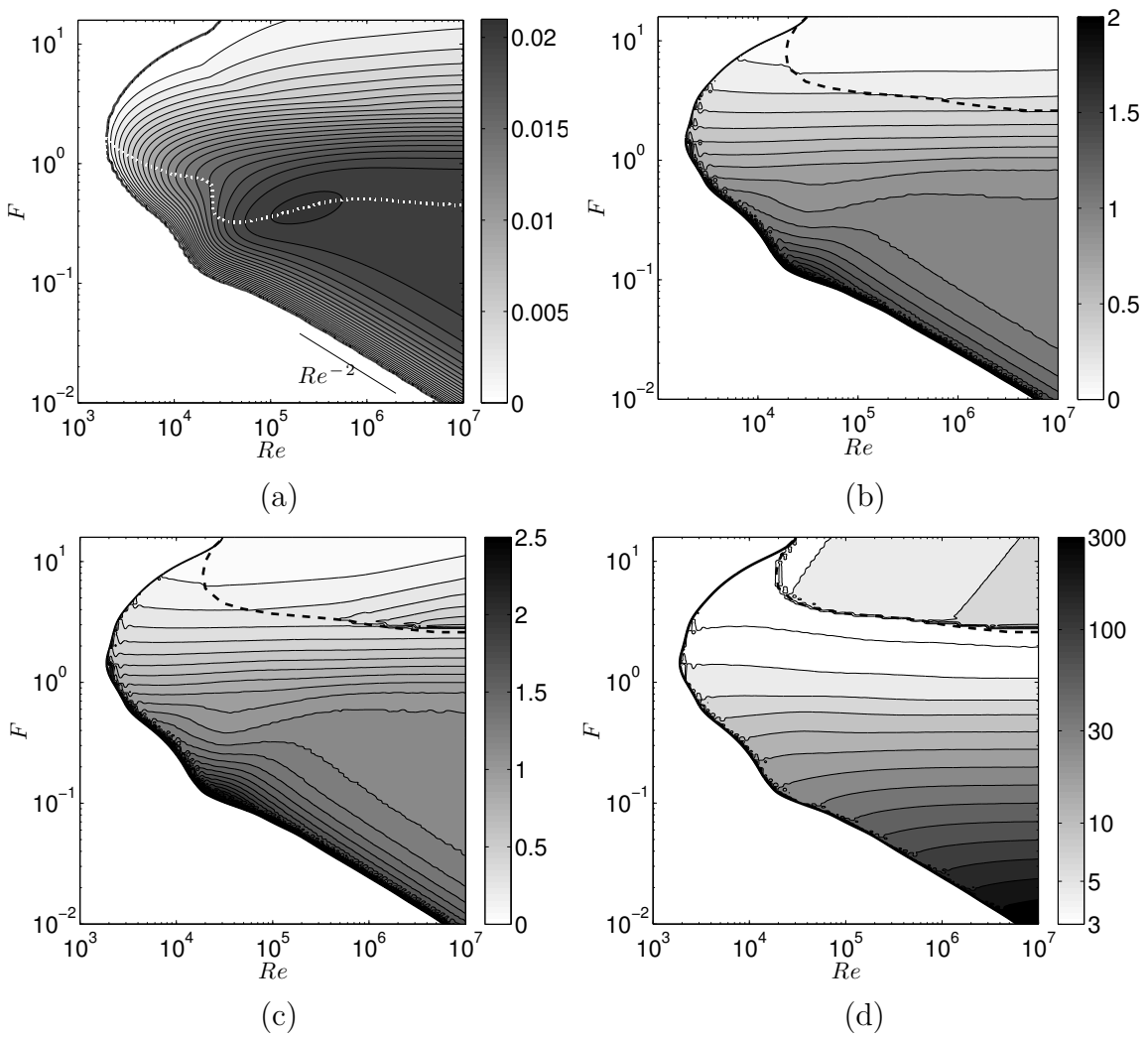

FIGURE 3.8 – Characteristics of the most unstable radiative mode (obtained by maximizing the growth rate over all k_x and k_z) in the (Re, F) plane. (a) Growth rate (Im(ω))contours ; (b) Oscillation frequency (Re(ω)) contours (in the unstable region) ; (c) Streamwise wavenumber (k_x) contours ; (d) : Transverse wavenumber (k_z) contours. The black dashed line indicates a discontinuity. The white dotted line in (a) gives the value of F which maximizes the growth rate for a fixed Re.

with the local growth rate peak jumps discussed above. We have observed a single jump which is indicated by the dashed line in figure 3.8(b-d).

The critical Reynolds number for the radiative instability is found to be $Re_c^{(r)} \approx 1995$ and is reached for $F_c^{(r)} \approx 1.51$. The characteristics of the critical radiative mode are $k_x \approx 0.615$, $k_z \approx 4.236$, $\omega \approx 0.535$. As expected, the Froude number instability range increases with the Reynolds number, but the most unstable growth rates are obtained for strongly stratified configurations for which F is smaller than 1. In figure 3.8(a), the white dotted line gives the Froude number which maximizes the radiative instability for a prescribed Reynolds number.

The behaviour of constant growth rate curves for small Froude and large Reynolds numbers can be obtained by adding the viscous corrections to the non-viscous estimate. In

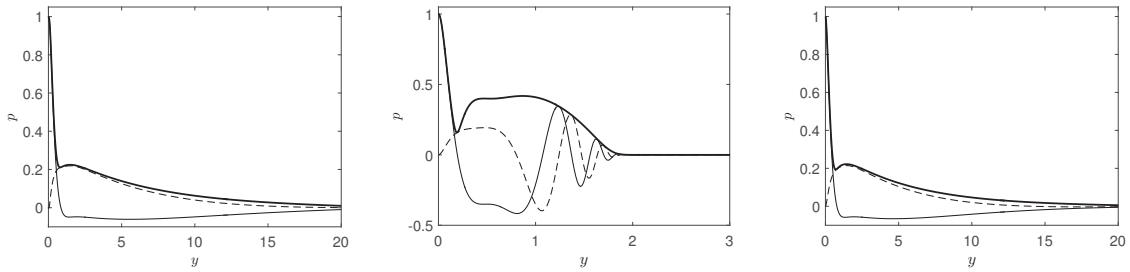

FIGURE 3.9 – Pressure eigenfunction of distinguished radiative modes for $F = 3$ and two Reynolds numbers (corresponding to the symbols of figure 3.5(c,d)). (a) Most unstable mode for $Re = 10^4 : k_x = 0.33$, $k_z = 3.13$, $\omega = 0.2971 + 0.0043i$; (b) Most unstable mode for $Re = 10^7 : k_x = 0.64$, $k_z = 8.75$, $\omega = 0.2817 + 0.0086i$; (c) Less unstable mode corresponding to the first local peak of the growth rate curves for $Re = 10^7 : k_x = 0.34$, $k_z = 2.75$, $\omega = 0.3023 + 0.0084i$. Thick solid lines, solid lines and dashed lines represent absolute value, real part and imaginary part, respectively.

this limit, Candelier *et al.* (2012) have indeed shown that the most unstable inviscid mode was obtained for $k_z/k_x \sim 4.9/F$. This means that for small F, k_z is much larger than k_x as well as the wavenumber based on the characteristic scale in the normal direction (y) which varies as k_x. The viscous damping of the mode is then expected to be just $-k_z^2/Re$. If we assume that k_x is approximatively constant, this gives a viscous growth rate which is constant on the line ReF^2 =Cst, as approximatively observed in figure 3.8(a).

The eigenfunctions of the distinguished radiative modes marked by symbols in figure 3.5 are shown in figures 3.9 and 3.10. Figures 3.9(a,b) show the pressure eigenfunction of the most unstable mode for a weakly stratified configuration ($F = 3$) at $Re = 10^4$ and 10^7. The pressure eigenfunction for $Re = 10^7$ strongly resembles the inviscid eigenfunction obtained by Candelier *et al.* (2012) for large Froude numbers and large wavenumbers. For smaller Reynolds numbers, the eigenfunction is by contrast different. These differences are not due to a change of instability mode. The modes are on the same instability branch but they are associated with two different local peaks of the growth rate contours in the (k_x, k_z) plane. For $Re = 10^4$, the most unstable mode corresponds to the first peak, while it is the second peak for $Re = 10^7$ (see figure 3.5(c)). It should be noted that the mode associated with the first peak is still unstable for $Re = 10^7$, and its pressure eigenfunction is the same as for $Re = 10^4$, as seen in figure 3.9(c).

In figure 3.10, we have considered a strongly stratified case ($F = 0.5$). Figures 3.10(a) and 3.10(b) show the pressure eigenfunction of the most unstable radiative mode for two different Reynolds numbers. By comparing these two figures, we observe that the impact of the Reynolds number is much weaker than for the weakly stratified case, as the pressure eigenfunction is almost not modified. Besides, this eigenfunction is very similar to the eigenfunction of the most unstable mode obtained for $Re = 10^4$ and $F = 3$. However, it is very different from the most unstable inviscid eigenfunction obtained by Candelier

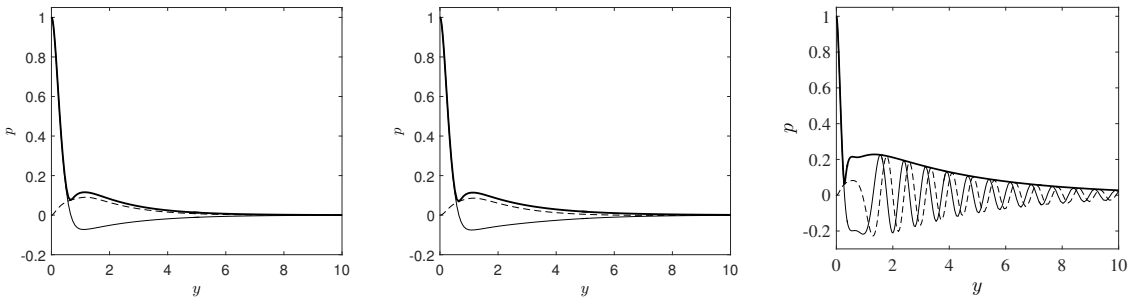

FIGURE 3.10 – Pressure eigenfunction of distinguished radiative modes for $F = 0.5$ and two Reynolds numbers (corresponding to the symbols of figure 3.5(a,b)). (a) Most unstable mode for $Re = 10^4 : k_x = 1.18$, $k_z = 9.34$, $\omega = 0.964 + 0.011i$; (b) Most unstable mode for $Re = 10^7 : k_x = 1.17$, $k_z = 9.58$, $\omega = 0.9499 + 0.0209i$; (c) Slightly less unstable mode for $Re = 10^7$ corresponding to the second local peak of the growth rate curves : $k_x = 1.80$, $k_z = 17.56$, $\omega = 0.928 + 0.0209i$. Thick solid lines, solid lines and dashed lines represent absolute value, real part and imaginary part, respectively.

et al. (2012) for small Froude numbers. The inviscid mode exhibits an oscillating structure which is not present in the viscous mode for $Re = 10^4$ and $Re = 10^7$ [see figure 3.10(a,b)]. This difference is mainly due to a property already mentioned above : the viscous mode is associated with the first peak and has a small streamwise wavenumber (as for the modes shown in figure 3.9(a,c)). We suspect that this peak could be of viscous nature. It indeed gives a mode with a non-oscillating structure which resembles that of 2D Tollmien-Schlichting waves (see figure 3.3). If we consider the mode associated with the second peak, we obtain an eigenfunction with an oscillatory tail [figure 3.10(c)] which resembles the inviscid eigenfunction obtained for small Froude numbers (see Candelier *et al.* 2012, figure 4). It is important to stress that this mode has almost the same growth rate as the most unstable mode.

Although the pressure eigenfunctions in figure 3.10(b) and (c) are quite different, these eigenfunctions are essentially associated with the same mode but for different wave numbers. Several internal cases between figure 3.10(b) and (c) are tested and their corresponding pressure eigenfunctions are illustrated in figure 3.11(a)-(d). The radiative phenomenon (oscillations far away from the wall) are increasing progressively. This is a gradual transition, rather than a "jump" from one mode to another.

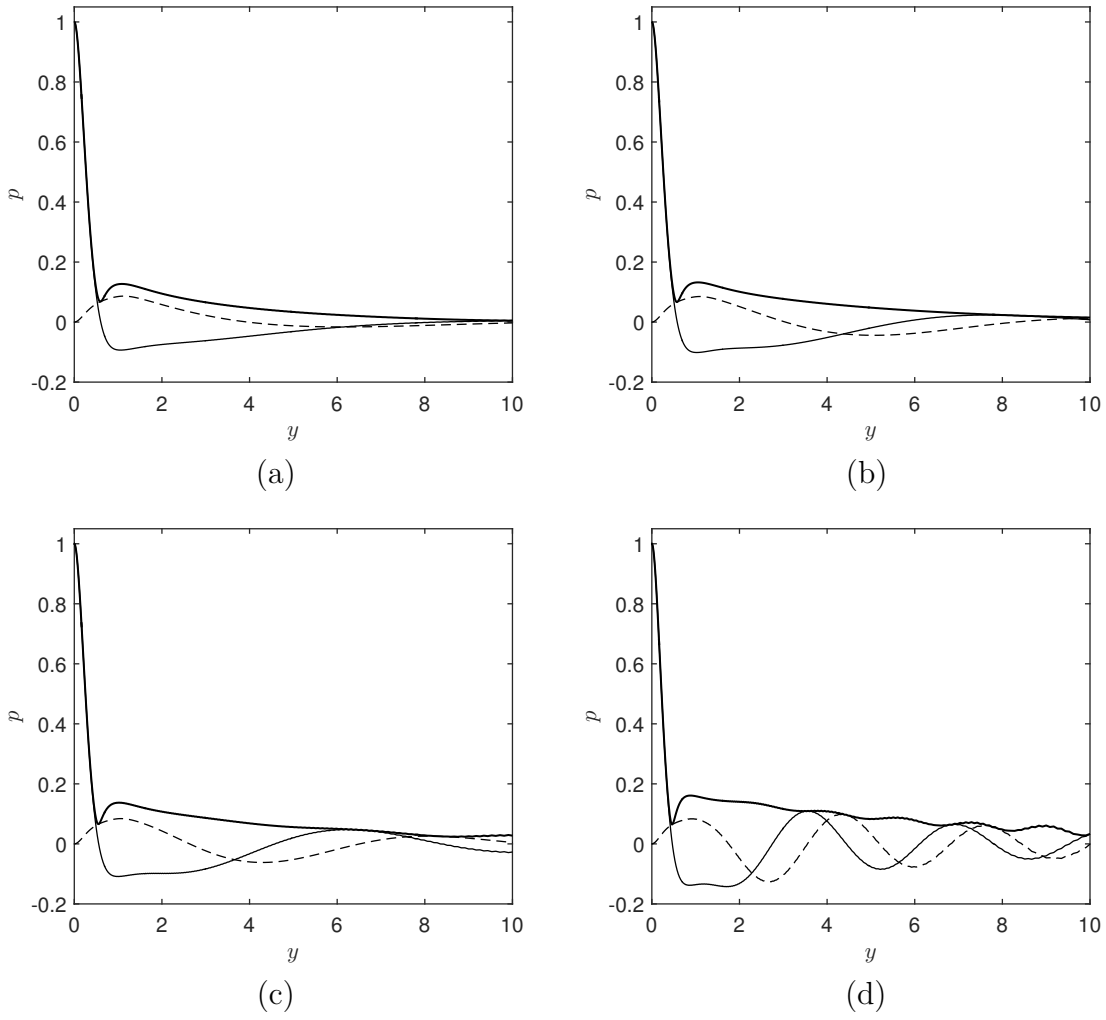

FIGURE 3.11 – Transition of the pressure eigenfunction of radiative modes for $Re = 10^7$, $F = 0.5$ (the internal cases between figure 3.10(b) and (c)). (a) $k_x = 1.191$, $k_z = 9.8466$, $\omega = 0.9488 + 0.0206i$; (b) $k_x = 1.211$, $k_z = 10.08$, $\omega = 0.9493 + 0.0204i$; (c) $k_x = 1.232$, $k_z = 10.31$, $\omega = 0.9499 + 0.0203i$; (d) $k_x = 1.342$, $k_z = 11.60$, $\omega = 0.9500 + 0.0205i$. Thick solid lines, solid lines and dashed lines represent absolute value, real part and imaginary part, respectively.

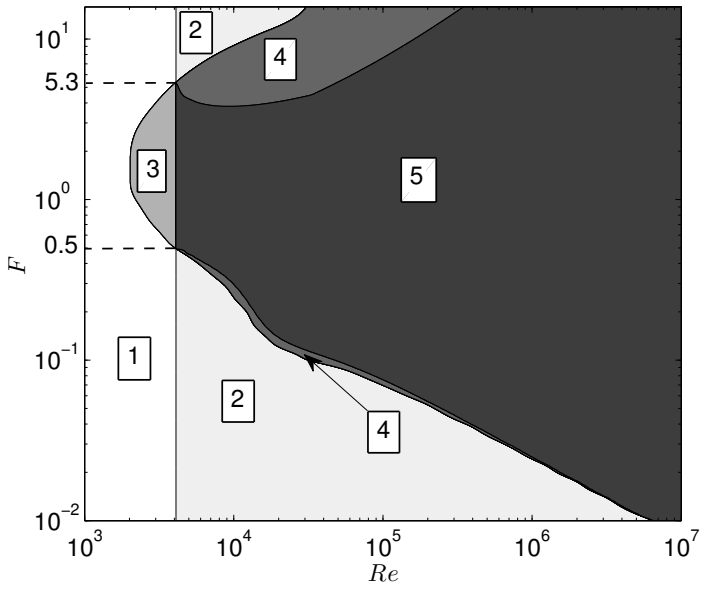

FIGURE 3.12 – Domains of instability in the (Re, F) plane. (1) No instability ; (2) Viscous instability without radiative instability ; (3) Radiative instability without viscous instability ; (4) Both instabilities present but viscous instability dominates radiative instability ; (5) Both instabilities present but radiative instability dominates viscous instability.

3.2.3 Competition between radiative instability and viscous instability

As shown above, the viscous instability is present as soon as $Re > 3981$ for any Froude number, while the radiative instability is active in a domain of the (Re, F) plane which has been displayed in figure 3.8(a). Both instabilities are then expected to be in competition in a large domain of the parameter space. In figure 3.12, we have provided a summary of this competition by indicating 5 different domains corresponding to a domain of no instability, 2 domains where there is a single instability active, 2 other domains where one instability dominates the other. This figure clearly demonstrates that the radiative instability is the dominant instability in a large domain of the parameter space. It is the first instability to appear as the Reynolds number increases in the range $0.5 < F < 5.3$. For $Re = 10^6$, it dominates the viscous instability in the large range $0.03 < F < 30$.

3.3 Discussion

In this article, we have demonstrated that a stably stratified boundary layer flow on a vertical wall is affected by two instabilities : a classical 2D viscous instability and a three-dimensional non-viscous radiative instability. We have shown that the radiative instability is the first instability to appear as the Reynolds number increases for $0.5 < F < 5.3$, and is the dominant instability in a large Froude number interval around $F = 1$ for large Reynolds numbers. In the domain of parameters where the instability growth rate is the

largest (large Reynolds numbers, small Froude numbers), the instability is characterized by a streamwise wavelength scaling with the boundary layer thickness and a small transverse wavelength proportional to F. The radiative instability is oscillatory with a frequency close to 1 (that is U/L in dimensional form). The most unstable mode extends up to a few boundary layer thickness.

The work has focused on the temporal stability property of a local boundary layer profile. We have found that the streamwise wavenumbers of the most unstable radiative mode increases with the Reynolds number and remains always larger than 0.1 for $F < 16$. For TS waves, we have obtained that the streamwise wavenumber weakly decreases with the Reynolds number but is still larger than 0.05 for $Re = 10^7$. For both types of modes, there is then a clear separation of scales between the instability wavelength and the $O(Re)$ spatial evolution length of the boundary layer flow. This justifies a posteriori the local parallel-flow assumption that we have made in neglecting the spatial development of the flow. Nevertheless, it would be interesting to perform a spatial stability analysis (in which the frequency is fixed, and one of the wavenumbers unknown) to get some information on the spatial development of the instability from a localized excitation, as done in Wu & Zhang (2008*b*).

It may be useful to apply the present results to experimental facilities such as the large stratified water flume of CNRM at Toulouse (Paci *et al.* 2011) to determine whether the radiative instability could develop on the side wall. Toulouse facility is 30 m long and 1.6 m deep. In normal conditions of use, it typically generates on the side walls a boundary layer flow of characteristics $U = 0.1\ \mathrm{m\,s^{-1}}$, $L = 10$ cm and $N = 1\ \mathrm{rad\,s^{-1}}$ which gives $Re = 10000$ and $F = 1$. The most unstable mode of such a flow has the characteristics $k_x = 0.83$, $k_z = 5.47$, $\omega = 0.7 + 0.012i$. It gives a period $T = 2\pi L/(U\mathrm{Re}(\omega)) \approx 9$ s, a growth time $\tau = L/(U\mathrm{Im}(\omega)) \approx 80$ s, a streamwise wavelength 75 cm, and a transverse wavelength 12 cm. Such a perturbation clearly fits within the channel. It is much stronger than the viscous instability of the boundary layer which has a growth time ten times larger for this Reynolds number. We believe that this instability could be present on the side wall of the channel. We suspect that it could affect the quality of the flow within the channel.

The radiative instability could also be present in real geophysical flows. Consider a stably stratified nocturnal atmospheric boundary layer, as reported in Frehlich *et al.* (2008). The velocity and thickness of this boundary layer flow is $U = 10\ \mathrm{m\,s^{-1}}$, and $L = 100$ m, respectively. The buoyancy frequency associated with the stratification is approximatively $N = 0.031\ \mathrm{rad\ s^{-1}}$ while the kinematic viscosity is $\nu = 10^{-5}\ \mathrm{m^2\,s^{-1}}$. This gives $F = 3.2$, and $Re = 10^8$. If such a flow was present on a vertical cliff, it would be unstable with respect to a radiative instability by a mode of characteristics $k_x = 0.95$, $k_z = 13.84$, $\omega = 0.27 + 0.0083i$. This would give a perturbation period $T \approx 3.5$ mn and

a characteristic growth time $\tau \approx 20$ mn. The streamwise and transverse wavelengths of this perturbation would be 660 m and 45 m, respectively.

The deep ocean is stably stratified. If we assume a buoyancy frequency approximatively equal to 0.01 rad s^{-1} (Alford & Gregg 2006) and a kinematic viscosity $\nu = 10^{-6}$ m^2 s^{-1}, a boundary layer flow of velocity $U = 0.15$ m s^{-1} and thickness $L = 10$ m would correspond to the parameters $Re = 1.5 \times 10^6$ and $F = 0.15$. On a vertical ridge or a very steep slope, such a flow would be unstable with respect to the radiative instability by a mode of characteristics $k_x = 1.23$, $k_z = 33$, $\omega = 1 + 0.02i$. This would give a period $T \approx 7$ mn, a growth time $\tau \approx 1$ h, and a spatial structure of wavelength 51 m in the streamwise direction and 1.9 m in the transverse direction.

We have analysed the stability of a boundary layer flow on a vertical wall. For oceanic applications, it would be more relevant to consider inclined slopes. In that case, the radiative instability is still present but with a weaker growth rate (Candelier *et al.* 2012). However, the radiative instability disappears on a horizontal surface. For the flow on a surface of moderate slope, a stronger competition could exist between viscous and radiative instability, but for large Reynolds numbers, the radiative instability is always expected to dominate as its growth rate does not decrease with the Reynolds number.

Note finally that we have not considered the effect of density diffusion. For both the atmosphere and the ocean, one should consider the temperature diffusion, for which the equivalent Schmidt number (Prandtl number) is of order 1. This stronger diffusion is expected to enhance the damping of the mode but this effect should remain small for the Reynolds numbers relevant to the geophysical applications (typically $Re > 10^6$).

The impact of the radiative instability on the dynamics of the atmosphere or the ocean remains unknown. When it is present, does it only contribute to the local mixing in the boundary layer, or does it induce a mixing further away from the boundary due to the radiative extension of the instability mode are among the interesting questions that have to be addressed. Answering these questions would require an understanding of the nonlinear evolution of the instability. This could constitute a nice objective for the future numerical or experimental works on the subject.

Chapitre 4

Instability of plane Poiseuille flow in a stably stratified fluid

4.1 Introduction

The famous pipe flow experiment conducted by Reynolds (1883) showed that a laminar flow could break down and turn into complicated spatial and temporal behaviours. To illustrate underlying mechanisms in the fluid motions, researchers have used different prototypes in both theoretical and experimental studies. Plane Poiseuille flow is one of the simplest parallel shear flows that satisfy the Navier-Stokes equations and its stability and transition to turbulence is subtle. This flow is proved to be unstable when the Reynolds number exceeds a critical value. However, as stratification is ubiquitous in nature, it is of fundamental interest to investigate the stability and related properties of stratified plane Poiseuille flow.

In this chapter, we examine the modal and non-modal stability of a plane Poiseuille flow in the presence of stable density stratification, under the Boussinesq approximation. The various mechanisms of exponential and transient growth are identified and characterised. Mathematically, the exponentially growing instability can be investigated through modal stability analysis, and the transient growth can be evaluated with the non-modal analysis (Schmid 2007).

As we have shown in chapter 3, stable stratification can induce radiative instability in the boundary layer, it is natural to study the stratification effects on the stability of plane Poiseuille flow. Both the exponential and transient growth should be examined. It is the main objective of this chapter to illustrate the influence of stratification on the instabilities and fundamental mechanisms.

4.1.1 Modal stability of stratified Poiseuille flow

Modal stability analysis has been developed for a long time and has been used to predict the critical Reynolds number for instability.

The method of normal modes has been adopted to identify the exponential growth in the fluid. The earliest known stability analysis of a homogeneous plane Poiseuille flow is due to Heisenberg (1924), who first demonstrated that the instability responsible for transition is a viscous instability, which is also referred to as Tollmien-Schlichting (TS) waves. Orszag (1971) solved the Orr-Sommerfeld stability equation and showed that the unstratified plane Poiseuille flow become unstable to the viscous mode if the Reynolds number, non-dimensionalised by the half-width of the channel, exceeds the critical value $Re_c^{(v)}(\approx 5772.2)$. The argument of the critical value is also based on the Squire's theorem (Squire 1933), which predicts that the most unstable mode is two-dimensional. However, in the presence of stratification, the Squire's theorem is not applicable. Miles (1961); Howard (1961) showed the Kelvin-Helmholtz instability is diminished by stable stratification, but the effect of vertical stratification on a viscous instability is less known.

The results in Chapter 3 have shown that on a vertical wall, the stratification can induce the radiative instability in the boundary layer. The radiative instability is also obtained by Le Dizès & Riedinger (2010) in the Taylor-Couette system in the limit of an infinite gap. When the size of the gap is finite, Le Dizès & Riedinger (2010) showed that the radiative instability changes into a so-called strato-rotational instability, which is associated with a mechanism of resonance. A similar resonance phenomenon will be shown to be active in the present study. The modes involved in the resonance are associated with the stratification, we shall refer to this instability as a "gravity mode".

4.1.2 Non-modal stability of stratified Poiseuille flow

In many experiments on channel flows, the transition to turbulence can occur at a Reynolds numbers which is much smaller than the critical value for instability. In addition to that, experiments about boundary layers (Klebanof 1971; Kendall 1985; Matsubara & Alfredsson 2001) show that the transition is usually preceded by the appearance of streamwise motion in the form of streaks rather than the TS waves. The reason for this phenomenon is that any initial disturbance has the potential to grow transiently whether or not the base flow is exponentially unstable.

As explained above, the transient growth derives from the non-normality of the Navier-Stokes operator and can occur without non-linear effects (Butler & Farrell 1992; Reddy & Henningson 1993). The combination of non-orthogonal eigenfunctions may lead to large transient growth even if every component decays exponentially at its own growth rate. Although the combination eventually decreases at a rate associated with its least

stable component, it could produce large enough transient growth that can excite the transition process. Three basic mechanisms are identified for the transient growth : Orr mechanism (Orr 1907), lift-up mechanism (Ellingsen & Palm 1975; Landahl 1980), and the combination of them (Farrell & Ioannou 1993*a*; Arratia *et al.* 2013). Physically, the increase of the total perturbation energy is related to vortex tilting and stretching in the finite time intervals.

Non-modal stability has proved to be an important complementary part for the modal stability, because the modal stability analysis fails to explain many experimental results (Klebanof 1971; Kendall 1985; Matsubara & Alfredsson 2001). The transition shown in these experiments is preceded by the streamwise streaks instead of the viscous instabilities. However, in the non-modal analysis, it is illustrated that the streamwise-uniform optimal initial perturbations can lead to large transient growth in streamwise motions through the lift-up mechanism (Ellingsen & Palm 1975; Landahl 1980).

In the unstratified plane Poiseuille flow, Butler & Farrell (1992) showed that the three-dimensional initial disturbance gains the most energy over a finite time interval. Reddy & Henningson (1993) also demonstrated that the maximal energy gain can achieve $\mathcal{O}(Re^2)$ at a time that is proportional to Re. The amplified perturbations can facilitate the transition from laminar to turbulent flow (Butler & Farrell 1992; Reddy & Henningson 1993).

As the plane Poiseuille flow is one of the representative prototypes which is sensitive to the initial conditions and the background disturbance, it is of fundamental interest to study its linear stability in the presence of vertical stratification.

4.1.3 Effect of horizontal shear and vertical stratification

As discussed by Basak & Sarkar (2006), many observations and various situations in the geophysical background, such as complex topography interacting with ocean currents, motivate the interest to study the stably stratified, horizontal shear flow. Dynamic evolutions including the selection of vertical structures are described in the DNS study of Basak & Sarkar (2006). Deloncle *et al.* (2007) showed that the Kelvin-Helmholtz instability is modified by the stratification. Subsequent works about the transient growth are conducted by Arratia (2011).

According to the studies of Bakas & Farrell (2009*a*,*b*), horizontal shear flow can excite internal gravity waves in the presence of a vertical stratification. They discussed the spontaneous gravity wave generation and gave the analytic expressions for unbounded constant shear in their works. Gravity waves are also found to be generated by large transient growth in inviscid horizontal shear layers (Arratia *et al.* 2016).

The previous works mainly focus on the unbounded shear flows, in the present study, we examine the instability of plane Poiseuille flow bounded by two vertical walls in a stably stratified fluid. The remainder of this chapter is organised as follows. In section 4.2, modal stability analysis is conducted on the stratified plane Poiseuille flow. We compare the viscous mode and the gravity mode, and also analyse the resonance mechanism for the gravity mode. In section 4.3, the non-modal stability analysis is performed, and the transient growth is evaluated. In section 4.4, we discuss the stratification effects on exponential and transient growth and draw some conclusion.

4.2 Modal stability analysis

We consider a horizontal channel flow in a vertically stratified fluid (see figure 2.1). As derived in chapter 2, the governing equations of the disturbance fields for the base flow are obtained by linearising the Navier-Stokes and the density equations under the Boussinesq approximation. By solving the general eigenvalue problem (2.23), the complex frequency ω can be obtained as a function of k_x, k_z, Re and F, namely $\omega(k_x, k_z, Re, F)$.

Two kinds of exponential growing instabilities are found in the vertically stratified plane Poiseuille flow. First, the viscous mode (TS wave) should be active. Second, a three-dimensional mode associated with stratification is found to be unstable, even in the region where $Re < Re_c^{(v)}$. This mode is the "gravity mode", as named in section 4.1.1.

4.2.1 Tollmien-Schlichting waves

The viscous instability associated with TS waves is active in a plane Poiseuille flow. It corresponds to the unstable mode shown in figure 2.3. The instability in plane Poiseuille flow has been known for a long time (e.g. Reid 1965). Those early studies are performed in unstratified fluid ($F = \infty$), wherein the Squire's theorem can draw the conclusion that the two-dimensional (2D) disturbance is the most unstable mode. The 2D mode is obtained for $k_z = 0$ and thus has no variation in the direction of stratification (z-axis). Although the 2D mode still exists in the fluid in the presence of stratification, it cannot be guaranteed to be the most unstable one, because the Squire's theorem is not applicable in a stratified fluid.

In figure 4.1 and 4.2, the growth rate contours of TS waves are plotted for $Re = 10^4$ and different Froude numbers. The effect of stratification on the growth rate contours in (k_x, k_z) plane is illustrated. The unstable domains associated with viscous instability are also determined. Moreover, from figure 4.1(a-c), we can tell that the instability domain shrinks as the stratification increases for a given Reynolds number in the limit of weak stratification. As shown in figure 4.2(a-c), this trend continues in the strongly stratified limit. However, there is a sudden expansion of the unstable domain between $F = 2$ and

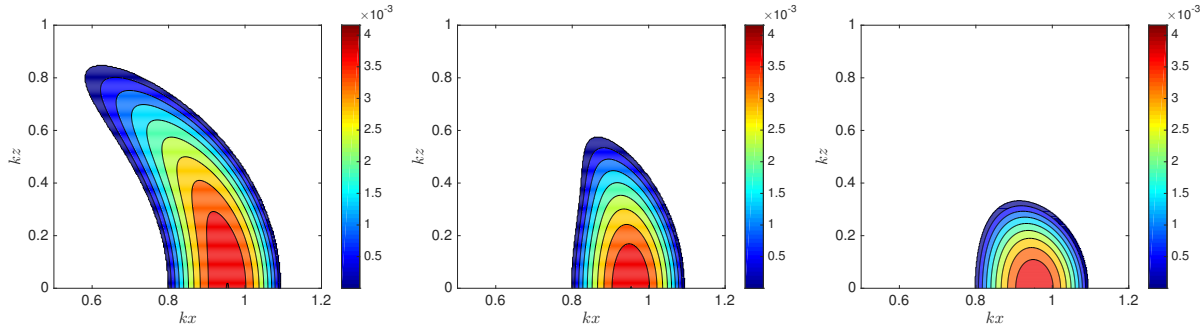

(a) (b) (c)

FIGURE 4.1 – Growth rate contours in (k_x, k_z) plane for $Re = 10^4$ and large and moderate Froude numbers. (a) $F = \infty$ (unstratified); (b) $F = 20$; (c)$F = 2$. Contours are every 0.0004 from 0 to 0.0042. It should be noted that the k_z intervals here are $[0, 1]$.

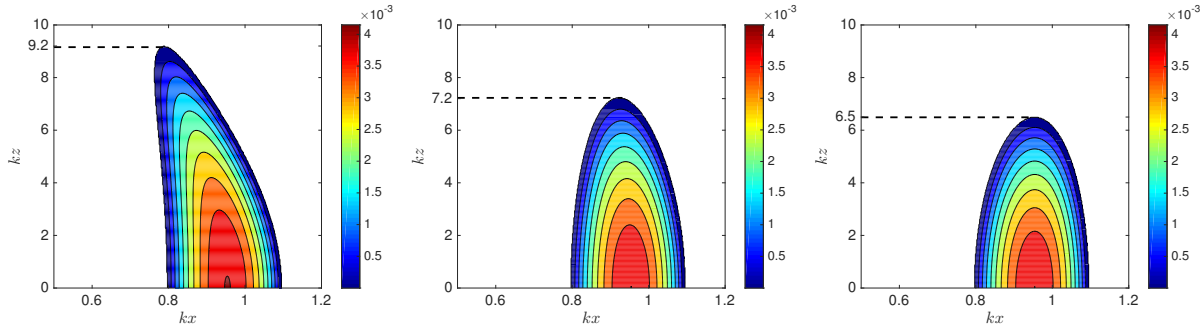

(a) (b) (c)

FIGURE 4.2 – Growth rate contours in (k_x, k_z) plane for $Re = 10^4$ and small Froude numbers. (a) $F = 0.2$; (b) $F = 0.1$; (c)$F = 0.01$; Contours are every 0.0004 from 0 to 0.0042. It should be noted that the k_z intervals here are $[0, 10]$.

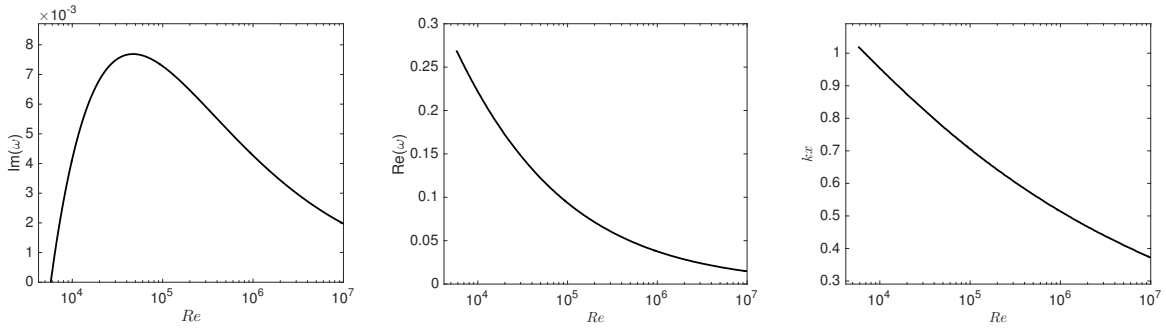

(a) (b) (c)

FIGURE 4.3 – Viscous instability (TS waves). Characteristics of the most unstable TS wave as a function of Re. (a) Growth rate $\mathrm{Im}(\omega)$; (b) Oscillation frequency $\mathrm{Re}(\omega)$; (c) Wavenumber k_x.

$F = 0.2$. Indeed, it should be noted that the k_z interval is $[0, 1]$ for figure 4.1, but the k_z interval for figure 4.2 is $[0, 10]$. This indicates that the modes might be different with weak and strong stratifications, except the 2D modes ($k_z = 0$). The expansion of the unstable domain from figure figure 4.1(c) to figure 4.2(a) will be explained below.

In figure 4.1 and 4.2, the most unstable viscous mode is independent of the Froude number and stays at the same position ($k_x = 0.955, k_z = 0$) in the (k_x, k_z) plane. For other Reynolds numbers and Froude numbers, the most unstable TS wave among all possible wavenumbers remains two-dimensional ($k_z = 0$) and independent of the stratification. The characteristics of the most unstable TS waves are shown in figure 4.3 as functions of the Reynolds number since they are free from the influence of Froude number.

In figure 4.3, the critical Reynolds number of TS waves in a plane Poiseuille flow is found to be $Re_c^{(v)} \approx 5772$, and the characteristics of the critical TS wave are $k_x = 1.02$, $\omega = 0.269$. These values are defined by the left-most tip of the lines in figure 4.3 and agree with the ones found by Orszag (1971), who calculated the eigenvalues of Orr-Sommerfeld stability equations. The maximal exponential growth rate of TS wave in plane Poiseuille flow is achieved for a Reynolds number of $Re_m^v \approx 4.75 \times 10^4$ and a streamwise wavenumber $k_x = 0.7798$, the corresponding complex frequency is $\omega \approx 0.1244 + 0.007689i$. These values may be compared to the ones found by Schmid & Henningson (2001), whose results (on page 71) are not exactly the same but are very close : $Re \approx 46950$, $k_x \approx 0.782$, $\mathrm{Im}(\omega) \approx 0.007688$.

The eigenfunctions of TS waves for the critical Reynolds number and the most dangerous Reynolds number are presented in figure 4.4. The eigenfunctions of both modes are very similar and the difference between them is the maximum absolute value of streamwise velocity. Normalised by the normal velocity at the centre $v(0)$, the maximum absolute value of streamwise velocity for the most dangerous Reynolds number are larger than the one for the critical Reynolds number.

4.2.2 The gravity mode in the presence of stratification

In the unstratified plane Poiseuille flow ($F = \infty$), the critical Reynolds number is $Re_c^{(v)} \approx 5772$. However, in the presence of stratification, the critical Reynolds number is smaller. Examples of eigenvalue spectrum for $Re = 5000$ are shown in figure 4.5. Without stratification, all the modes shown in figure 4.5(a) are stable ($\omega_i < 0$), because the Reynolds number is below the critical one $Re_c^{(v)}$. The spectrum in figure 4.5(a) can be compared to the eigenvalues found previously by Butler & Farrell (1992), the Orr-Sommerfeld modes are the same and the extra branch is the Squire mode. But with the effect of stratification, there exists an unstable mode in figure 4.5(c) for $F = 2$, the corresponding eigenvalue is $\omega = 0.6987 + 0.03906i$. The eigenfunctions associated with this mode is presented in figure 4.6. The eigenvalues for the same wavenumbers ($k_x = 0.986, k_z = 3.615$)

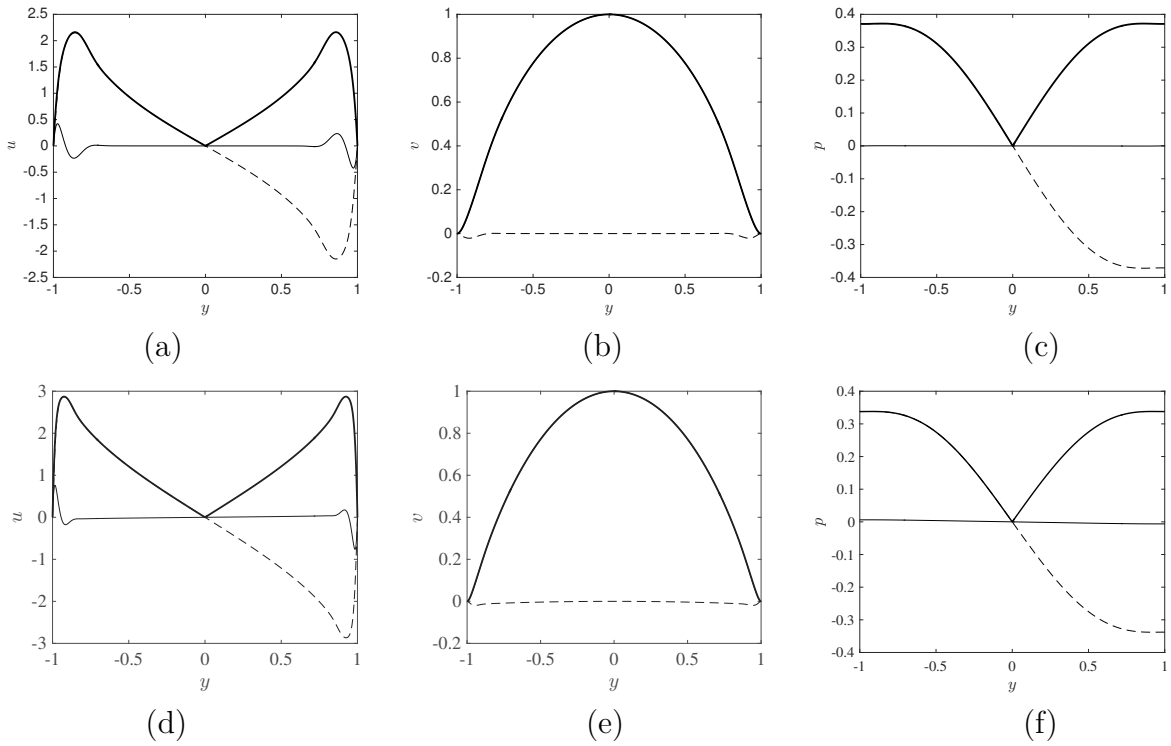

FIGURE 4.4 – Eigenfunctions of TS waves (left : streamwise velocity u ; middle : normal velocity v ; right : pressure p) for the critical Reynolds number $Re = Re_c^v \approx 5772$ (top) and the most dangerous Reynolds number $Re = Re_m^v \approx 4.75 \times 10^4$ (bottom). Thick solid lines, thin solid lines and dashed lines represent absolute value, real part and imaginary part, respectively. All eigenfunctions are normalized by v(0).

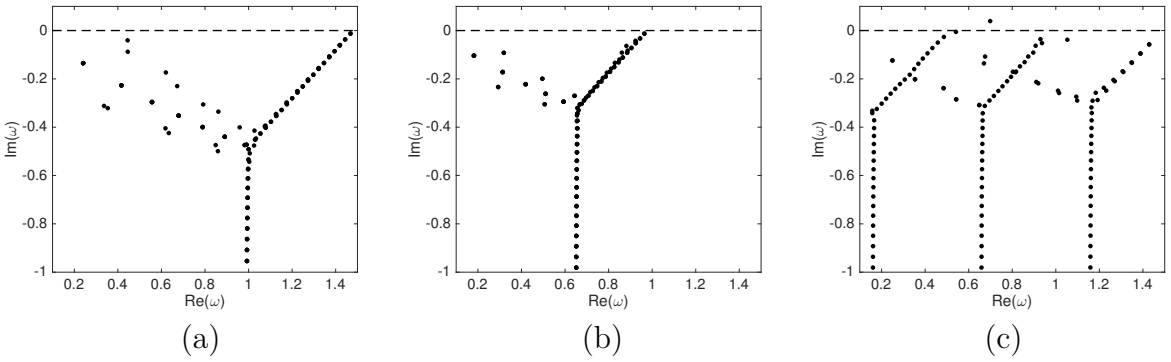

FIGURE 4.5 – Eigenvalues of plane Poiseuille flow for $Re = 5000$. (a) $F = \infty, k_x = 1.48, k_z = 0$; (c) $F = \infty, k_x = 0.986, k_z = 3.615$; (c) $F = 2, k_x = 0.986, k_z = 3.615$. The horizontal dashed line is $\mathrm{Im}(\omega) = 0$.

in the unstratified case are displayed in figure 4.5(b), which is similar to what is shown in figure 4.5(a). Therefore, the form of three groups are the result of stratification. The appearance of three Y-shaped branches agrees with the analytic modes obtained by Bakas & Farrell (2009*b*).

The eigenfunctions shown in figure 4.6 are different to those of the viscous mode shown in figure 4.4. More variations of normal velocity are observed in figure 4.6(b). The values close to the boundaries are raised compared to the structure in 4.4(b). The eigenfunctions in figure 4.6 are inviscid in nature because similar structures are observed in the inviscid case ($Re = \infty$). The eigenfunctions in the inviscid case are illustrated in figure 4.7 for the same Froude number ($F = 2$) and wavenumbers ($k_x = 0.986, k_z = 3.615$). The structures of normal velocity and pressure in figure 4.6(b,d) and figure 4.7(b,d) are very similar. Critical layers where the intrinsic frequency approaches the buoyancy frequency (at $y = y_{c1}$, $\omega_r - k_x U_0(y_{c1}) = 1/F$) can be observed in figure 4.7(c,e). In the inviscid limit, the eigenfunctions of transverse velocity and buoyancy are peaked at the critical layer level. Although these critical layers are believed to be stabilising (Riedinger *et al.* 2010*a*), their influence is not strong enough to stabilize the flow.

Another group of critical levels at $y = y_{c2}$ where $\omega_r - k_x U_0(y_{c2}) = 0$ are shown in figure 4.7(a,c). As discussed in the introduction, these critical levels forms the 'quantization' conditions. Similar to their roles in the over-reflection process, the critical levels and the 'quantization' zone make the mode become unstable.

This kind of instability results from a mechanism of resonance, as it will be explained in details in Section 4.2.3.

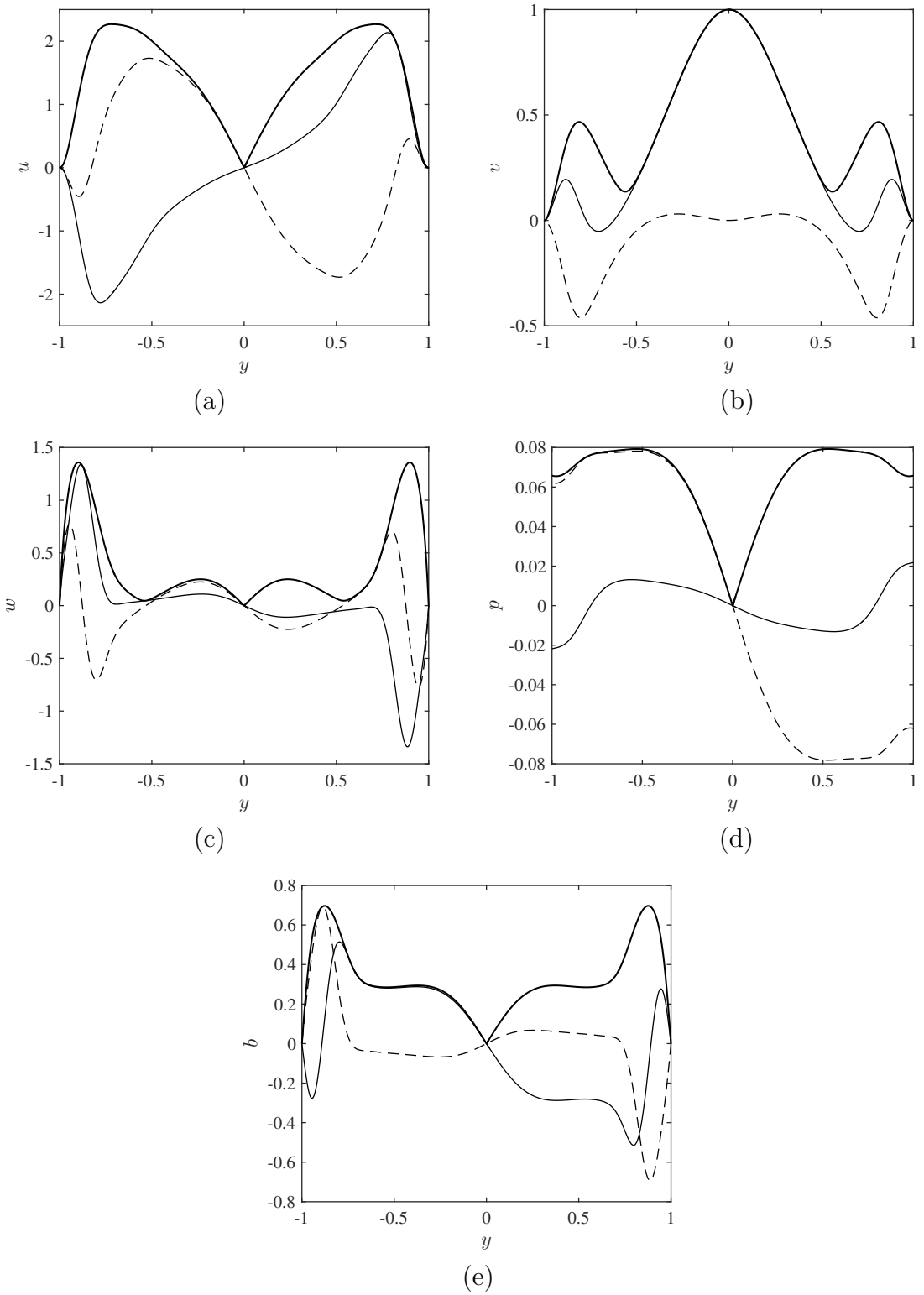

FIGURE 4.6 – Eigenfunctions associated with the unstable mode for the parameters $Re = 5000, F = 2, k_x = 0.986, k_z = 3.615, \omega = 0.6987 + 0.03906i$. (a) streamwise velocity u ; (b) normal velocity v ; (c) transverse velocity w ; (d) pressure p ; (e) buoyancy b ; Thick solid lines, thin solid lines and dashed lines represent absolute value, real part and imaginary part, respectively. All eigenfunctions are normalized by v(0).

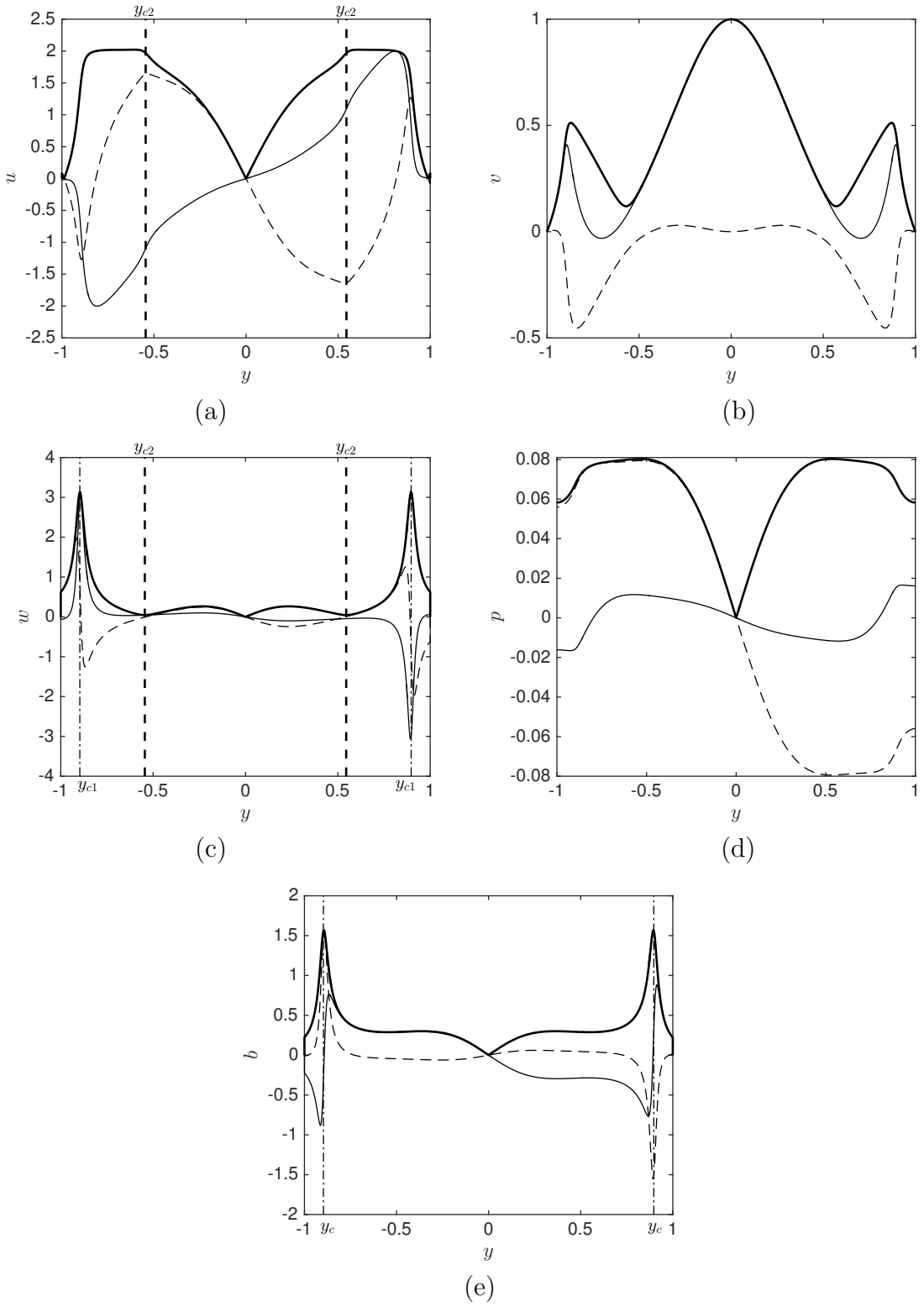

FIGURE 4.7 – Eigenfunctions associated with the unstable mode for the parameters $Re = \infty, F = 2, k_x = 0.986, k_z = 3.615, \omega = 0.6930 + 0.0391i$. (a) streamwise velocity u ; (b) normal velocity v ; (c) transverse velocity w ; (d) pressure p ; (e) buoyancy b ; Thick solid lines, thin solid lines and dashed lines represent absolute value, real part and imaginary part, respectively. All eigenfunctions are normalized by v(0). The dash-dotted lines in (c,e) describe the critical levels, where $\omega_r - k_x U_0(y_{c1}) = 1/F$. The vertical dashed lines in (a,c) represent the critical levels $\omega_r - k_x U_0(y_{c2}) = 0$.

4.2.3 Resonance mechanism

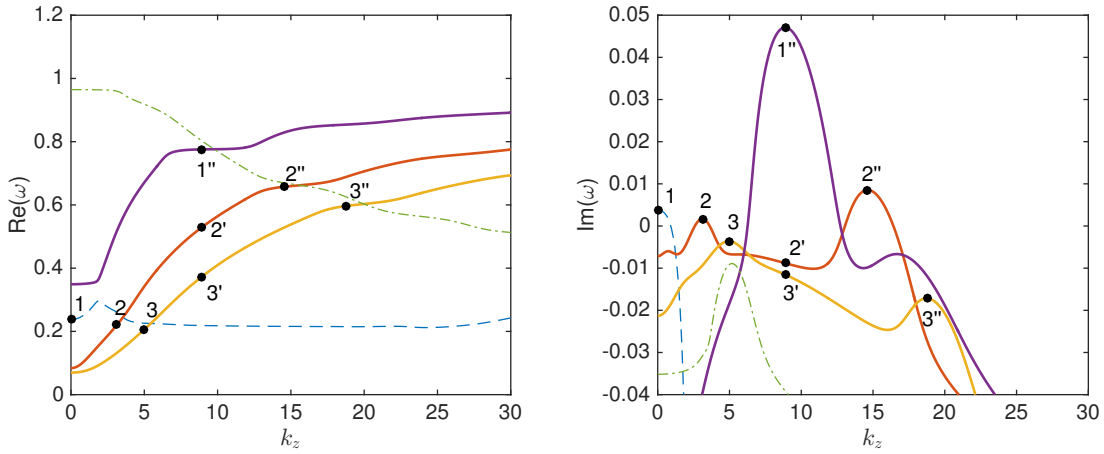

(a) (b)

FIGURE 4.8 – Frequency ω_r (a) and growth rate ω_i (b) versus transverse wavenumber k_z. The streamwise wavenumber is $k_x = 1$, and the other associated parameters are $Re = 10^4$, $F = 1.1$. The thick solid lines are inviscid modes. The dashed lines and the dash-dotted line are viscous modes.

Mode	Transverse wavenumber k_z	Eigenvalue ω
1	0	$\omega_1 = 0.2375 + 0.0037i$
$1''$	8.873	$\omega_{1''} = 0.7756 + 0.0471i$
2	3.133	$\omega_2 = 0.2204 + 0.0017i$
$2'$	8.873	$\omega_{2'} = 0.5273 - 0.0088i$
$2''$	14.56	$\omega_{2''} = 0.6575 + 0.0085i$
3	4.940	$\omega_3 = 0.2035 - 0.0036i$
$3'$	8.873	$\omega_{3'} = 0.3710 - 0.0115i$
$3''$	18.77	$\omega_{3''} = 0.5967 - 0.0172i$

TABLE 4.1 – Corresponding parameters of the marked modes in figure 4.8. The common parameters are $Re = 10^4$, $F = 1.1$, $k_x = 1$.

In the stratified plane Poiseuille flow, two families of modes exist at the same time. In figure 4.8, eigenvalues (ω) of the modes are traced by varying the transverse wavenumber k_z. Two series of frequency curves are shown in figure 4.8(a). The three branches, which have an increasing behaviour with respect to k_z, correspond to the inviscid modes mentioned in section 4.2.2, except Mode 1. The pressure eigenfunctions associated with these modes are displayed in figure 4.9. The other series of curves represent the viscous modes. Different branches correspond to the number of oscillations in the wall-normal direction. For example, for Mode $1''$, $2''$ and $3''$, complexity of their spatial structures increases with the label number, as shown in figure 4.9(b,e,h). Similar behaviour appears for Mode 1, 2, 3 in figure 4.9(a,c,f), half a wavelength for Mode 1, one wavelength for Mode 2, one and a half wavelength for Mode 3. Resonance occurs at the crossing points of the frequency curves. As correspondingly displayed in figure 4.8(b), the growth rate curves are peaked

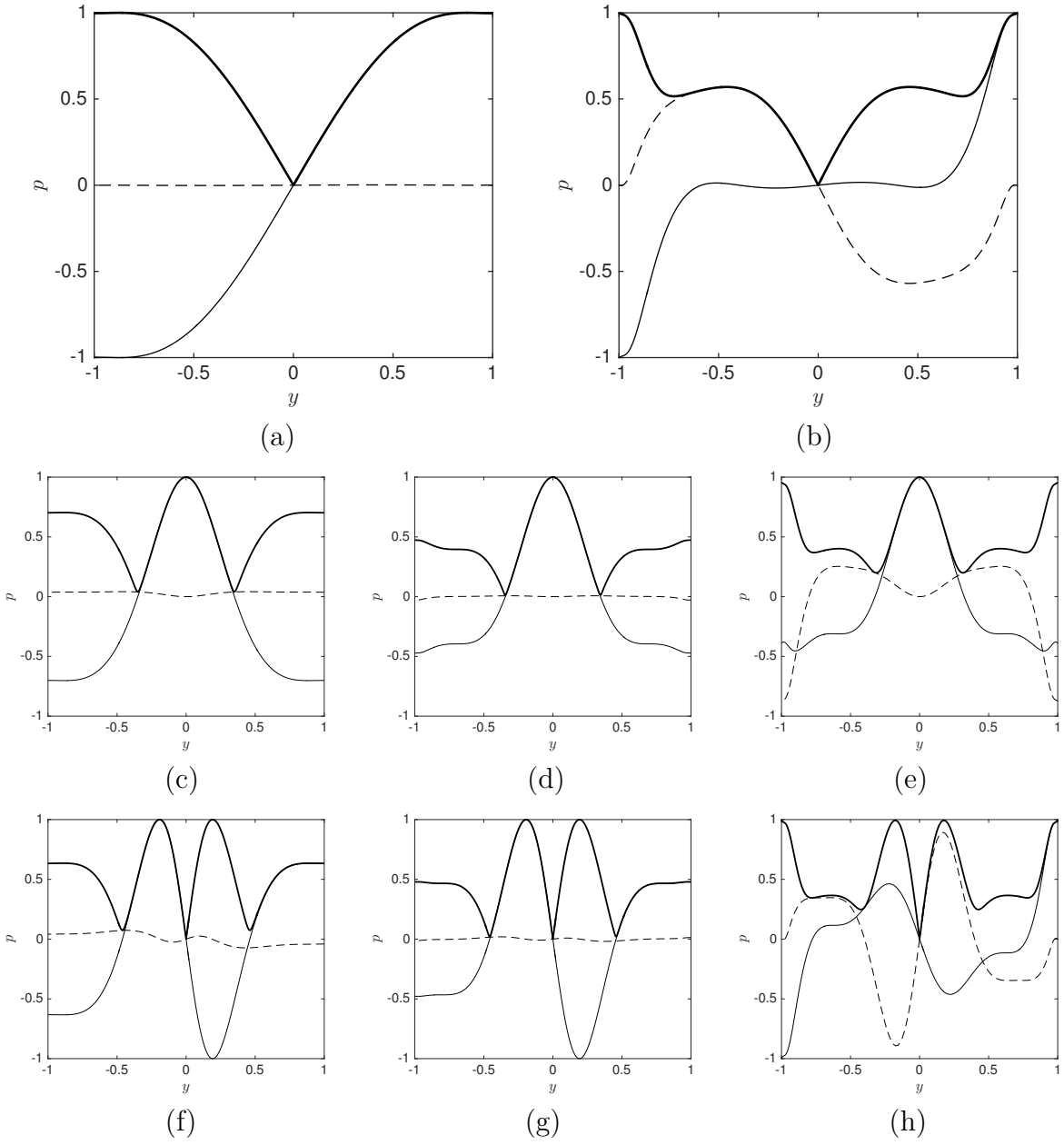

FIGURE 4.9 – Pressure eigenfunctions associated with the eigenvalues marked in figure 4.8. The common parameters are $Re = 10^4$, $F = 1.1$, $k_x = 1$. (top) Branch 1 : Mode 1 and $1''$; (middle) Branch 2 : Mode 2, $2'$ and $2''$; (bottom) Branch 3 : Mode 3, $3'$ and $3''$. Each eigenfunction is normalized by its maximum p_m, which satisfies $|p_m| = \max_{-1 \leqslant z \leqslant 1} |p(z)|$. Thick solid lines, thin solid lines and dashed lines represent absolute value, real part and imaginary part, respectively.

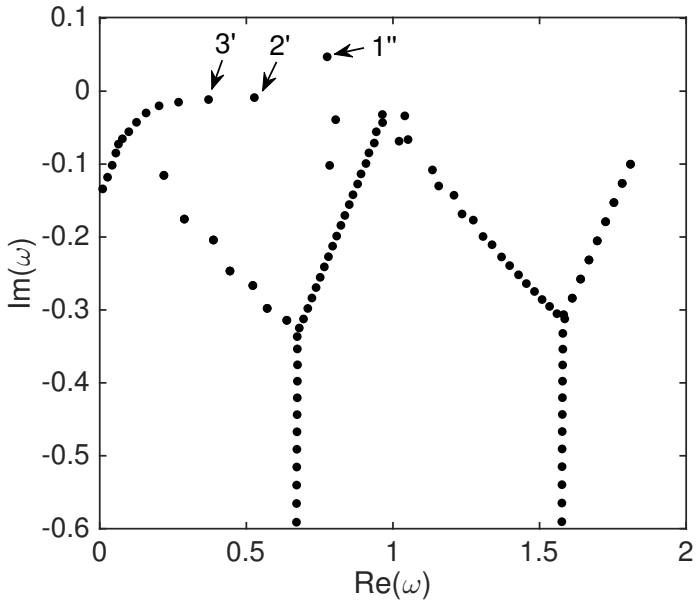

FIGURE 4.10 – Spectrum for the case $Re = 10^4$, $F = 1.1$, $k_x = 1$, $k_z = 8.873$. The eigenvalues marked as $1''$, $2'$, $3'$ are the inviscid modes marked in figure 4.8.

around each crossing point (Mode $1''$, 2, $2''$, 3, $3''$). This mechanism of resonance has been discovered in several other context (e.g. Satomura 1981; Le Dizès & Riedinger 2010).

With the same transverse wavenumber $k_z = 8.873$, two other modes (Mode $2'$ and $3'$) are also marked to demonstrate the effect of resonance. As shown in figure 4.10, sharing the same set of parameters (Re, F, k_x, k_z), the eigenvalues of mode ($1''$, $2'$, $3'$) are quite different, especially the imaginary parts (i.e. the growth rates). Increased by the resonance phenomenon with the viscous modes, the growth rate of Mode $1''$ is greatly larger than those of the other modes.

Table 4.1 classifies the corresponding parameters of these modes, including the specific transverse wavenumbers k_z and eigenvalues ω.

In figure 4.9, the shape of the eigenfunctions clearly explains the essential resonance mechanism. The increasing complexity of the structures for Branch 1-3 comes form the inviscid modes. The pressure structure of Mode 1 in figure 4.9(a) shows that it is a viscous mode and the maximum absolute values is located at the boundaries. The maxima in figure 4.9(c-e) are located at the centre part of the channel and this characteristic also comes from the inviscid modes. In figure 4.9(c,e) the feature of the viscous mode is still kept through the resonance process, especially in the regions close to the walls. Similar behaviours of the pressure eigenfunctions can also be found in figure 4.9(f,h) as these modes are also the results of resonance between viscous and inviscid modes.

The modes (Mode $2'$ and $3'$) without resonance phenomenon are away from the crossing points of the frequency curves in figure 4.8(a). The shapes of pressure eigenfunctions in figure 4.9(d,g) are similar to those of the modes on the same frequency branch (see

figure 4.8(a)). The notable difference is the values at the boundaries. Without resonance phenomenon, the absolute values at the boundaries in figure 4.9(d,g) are less than 0.5 when normalised by the maxima of the eigenfunction. However, in figure 4.9(c,e,f,h), the corresponding values are more than 0.6 with the same normalisation. These facts also indicate that the enhancement of the absolute values at boundaries in figure 4.9(c,e,f,h) derives from the the viscous mode, because this feature is the same as the structures shown in figure 4.9(a). Located on the same frequency branch, the structure of Mode $2'$ is similar to Mode 2 and $2''$ (figure 4.9(middle)), and Mode $3'$ is similar to Mode 3 and $3''$ (figure 4.9(bottom)).

In figure 4.10, the eigenvalues of Mode $(1'', 2', 3')$ are displayed in the same spectrum with the help of their common parameters (Re, F, k_x, k_z). The resonance with the viscous mode enhances the growth rate of Mode $1''$. In the spectrum, these three modes are located on the same branch in figure 4.10, representing the same inviscid nature.

4.2.4 Instability contours in wavenumber plane

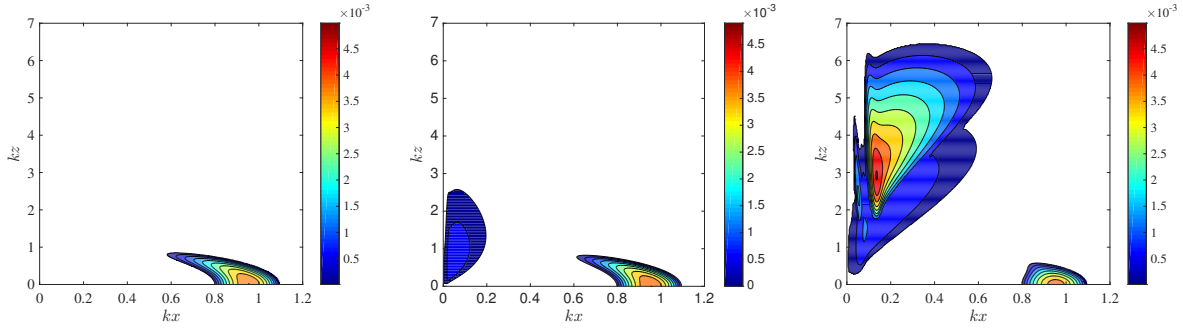

FIGURE 4.11 – Growth rate contours in (k_x, k_z) plane for $Re = 10^4$ and different Froude numbers. (a) $F = \infty$ (unstratified) ; (b) $F = 100$; (c) $F = 20$. Contours are every 5×10^{-4} from 0 to 5×10^{-3}.

As for the boundary layer flow, Squire's theorem does not apply for the plane Poiseuille flow in the presence of stratification. This is shown in figure 4.11. In that figure, the unstable region inside the intervals $0.6 \leqslant k_x < 1.2$ and $0 \leqslant k_z < 1$ relates to the TS waves. The most unstable viscous mode for this Reynolds number $Re = 10^4$ is : $k_x = 0.955,\ k_z = 0,\ \omega = 0.2221 + 0.0042i$, which is independent of the Froude number. For a moderate stratification ($F = 20$), the most unstable mode is the "gravity mode" in figure 4.11(c), and the corresponding parameters are : $k_x = 0.1345,\ k_z = 2.928,\ \omega = 0.0948 + 0.0050i$. This 3D unstable mode is generated by the resonance mechanism discussed in section 4.2.3. The effects of stronger stratifications on the gravity modes are shown in figure 4.12.

In figure 4.12(a), four separate continuous regions represent unstable modes, including the TS waves. Hence, there exist four different local peaks, and each of them stands for the most unstable mode in each region. As the Froude number decreases, the first region

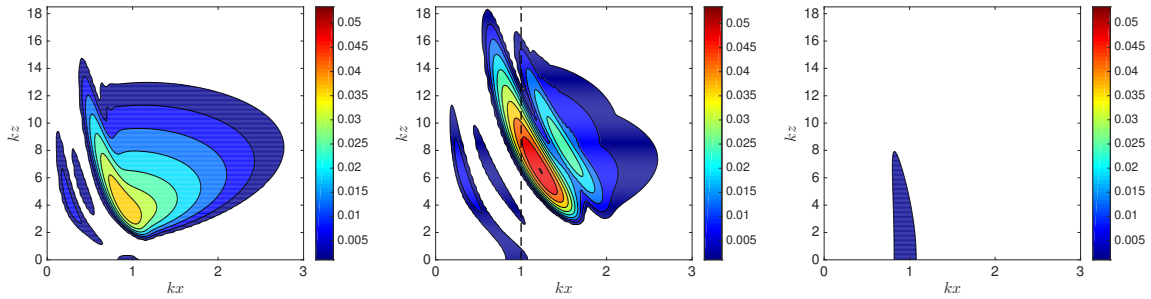

(a) (b) (c)

FIGURE 4.12 – Growth rate contours in (k_x, k_z) plane for $Re = 10^4$ and different Froude numbers. (a)$F = 2$; (b)$F = 1.1$; (c) $F = 0.2$, the same domain as figure 4.2(a). Contours are every 0.005 from 0.001 to 0.053. The dashed line $k_x = 1$ in (b) represents the cross-section made by figure 4.8.

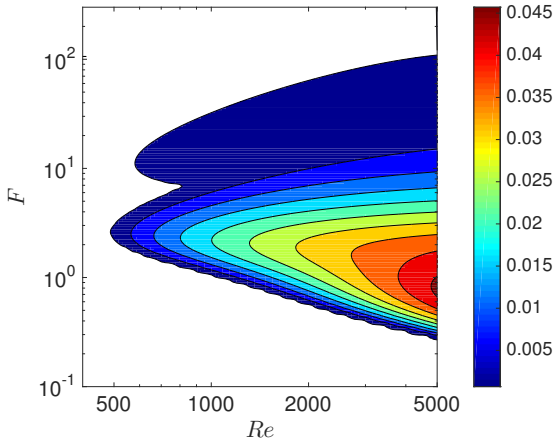

FIGURE 4.13 – Contours of the growth rates in (Re, F) plane. Contours are every 0.005 from 0.001 to 0.045.

(the left-most region with small streamwise wavenumbers $0.1 < k_x < 0.7$) merges with the area of the TS waves (the region with the smallest transverse wavenumber $0 \leqslant k_z < 0.5$). The eigenfunctions related to the modes in these two areas are similar. In figure 4.12(b), these two regions become connected for $F = 1.1$. Eventually, in a strongly stratified fluid ($F = 0.2$), they merge into one continuous region with only one local peak, as shown in figure 4.12(c). This phenomenon explains the sudden extension of the unstable domain from figure 4.1(c) to figure 4.2(a) as the associated Froude numbers change from $F = 2$ to $F = 0.2$.

With stronger stratification effects, the growth rate of the most unstable mode in figure 4.12(b) is larger than the one shown in figure 4.12(a). Mathematically, the imaginary part of the corresponding eigenvalues grows as the Froude number decreases. However, in a strongly stratified fluid (e.g. $F = 0.2$), the gravity modes become stable, but the viscous modes can remain unstable in this case, and the most unstable one becomes 2D again. For example, in figure 4.12(c) where $Re = 10^4$ and $F = 0.2$, only the region associated with viscous instability remains unstable in the wavenumber plane.

Depending on the change of Reynolds number and Froude number, the growth rates of the most unstable mode in different cases are summarised in figure 4.13. The growth rate contours are shown for the intervals $400 \leqslant Re \leqslant 5000$ and $0.1 \leqslant F \leqslant 300$ in (Re, F) plane. The critical Froude number for $Re = 5000$ is $F \approx 0.259$ and $F \approx 256$, which represent the extent from the strong stratification to the weak stratification. For a fixed Reynolds number, an extremum is achieved around $F \approx 1$, as shown in figure 4.13.

4.3 Non-modal stability analysis

To have a better understanding of the stability in a stratified Poiseuille flow, we investigate the transient growth in this section. Depending on the equation (2.9), the total energy of the perturbation is measured in the form of

$$E(t) = \int_{-1}^{1} \frac{1}{2} \left(|u|^2 + |v|^2 + |w|^2 + \frac{|b|^2}{F^2} \right) dy \tag{4.1}$$

The total energy is defined as a sum of kinetic and potential energy.

By solving equation (2.19), the evolution and transient growth characteristics can be obtained for an initial condition $\boldsymbol{f}(0)$, which can give rise to the total energy $E(t)$ in the process. The growth of the total energy is evaluated by the energy gain $G(T)$. For a finite time interval ($t \in [0, T]$), the optimal energy gain $G(T)$ is defined as equation (4.2)

$$G(T) = \max_{\forall \boldsymbol{f}(0) \neq \boldsymbol{0}} \left[\frac{E(T)}{E(0)} \right]. \tag{4.2}$$

The optimal initial conditions (also called optimal perturbations) are the fastest growing perturbations that achieves the maximal energy gain over a prescribed time T. Usually, they are a linear combination of different eigenfunctions, whether the corresponding eigenmodes are stable or not.

4.3.1 Verification for unstratified fluid

Over finite time intervals, the behaviour of the plane Poiseuille flow is not primarily influenced by the unstable modes we mentioned in section 4.2. The optimal response approaches the dominant eigenfunctions when $T \to \infty$, hence the eigenvalue of the most unstable mode can only determine the long-time optimal response. In a homogeneous fluid, the short-time response is usually governed by the Orr mechanism (Orr 1907), lift-up mechanism (Ellingsen & Palm 1975; Landahl 1980) and the combination of these two mechanisms (Farrell & Ioannou 1993*a*; Arratia 2011). These three mechanisms can be differentiated by the wavenumbers, $k_z = 0$ for the Orr mechanism, $k_x = 0$ for the lift-up mechanism and $k_x k_z \neq 0$ for the combination. However, in the presence of stratification, since we have demonstrated that 3D gravity modes are active in the plane Poiseuille flow,

it is necessary to quantify the effect of stratification and examine whether there are other mechanisms in the transient growth process.

Lift-up mechanism ($k_x = 0$)

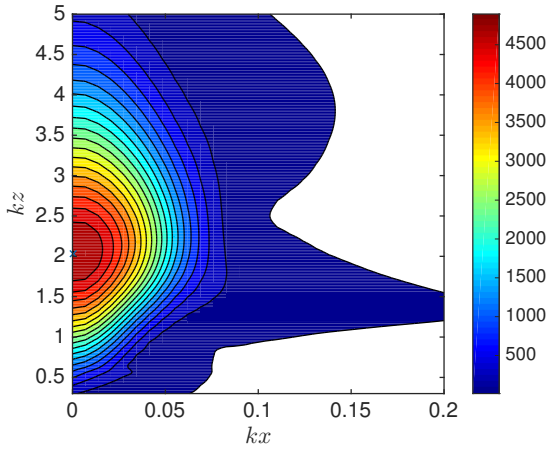

FIGURE 4.14 – Energy gain contours in (k_x, k_z) plane for $Re = 5000$, $F = \infty$ and $T = 379$. Contours are every 257 from 10 to 4895.

According to equation (4.2), the energy gain eventually becomes a function of various parameters through our derivation $G(Re, F, k_x, k_z, T)$. As illustrated in figure 4.14, the energy gain are demonstrated in the wavenumber plane for fixed basic parameters (Re, F, T). The maximal energy gain G_m is defined as

$$G_m = \max_{\forall k_x, k_z} G(k_x, k_z) \tag{4.3}$$

In figure 4.14, the maximal energy gain $G_m|_{T=379} = 4895$ at $(k_x, k_z) = (0, 2.04)$. The lift-up mechanism dominates in this case as the maximum is located on the k_z-axis. The transient growth of perturbation energy is substantial even though the Reynolds number ($Re = 5000$) is below the critical value. This result agrees with the result in the previous works about 3D unstratified plane Poiseuille flow (Butler & Farrell 1992; Reddy & Henningson 1993). Determined by the lift-up mechanism, the initial perturbations are streamwise-uniform vortices ($k_x = 0$) and the streamwise velocity u greatly grows as time evolves. In the evolution process, the variation of v in the wall-normal direction (y-axis) is believed to "lift-up" low-speed fluid parcels from the wall so that the streamwise momentum is conserved (in the direction of x-axis).

Combination of Orr and lift-up mechanisms ($k_x, k_z \neq 0$)

Further results for a short time interval ($T = 20$) are illustrated in figure 4.15(a), the maximal energy gain is $G_m|_{T=20} = 510$ at $(k_x, k_z) = (0.90, 3.15)$. The position of the

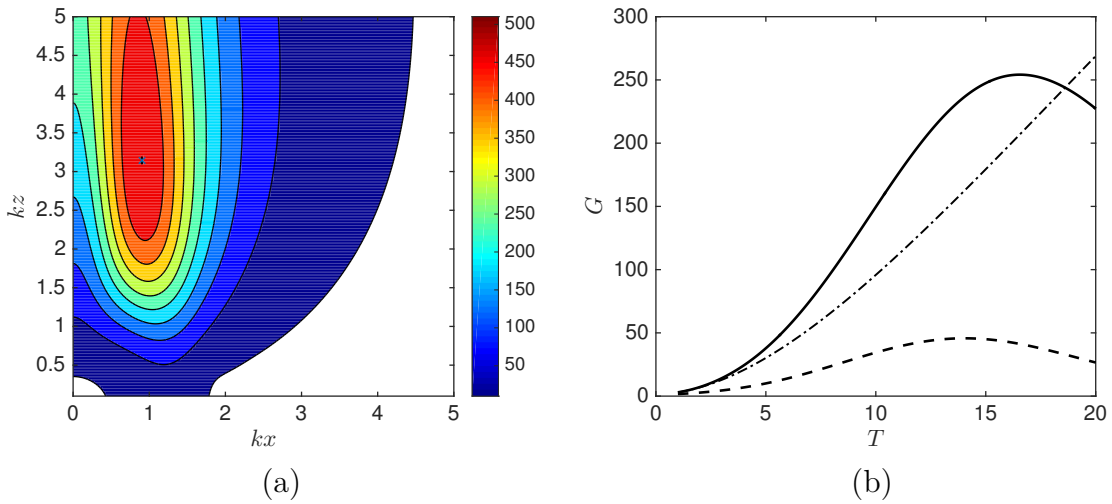

(a) (b)

FIGURE 4.15 – Energy gain G for unstratified plane Poiseuille flow ($Re = 5000,\ F = \infty$). (a) Contours in (k_x, k_z) plane for $T = 20$. The contours are every 56 from 10 to 510. (b) $G(T)$ at different wavenumbers. The associated wavenumbers are : $(k_x, k_z) = (1.48, 0)$ for the dashed line, $(k_x, k_z) = (0, 7.3)$ for the dash-dotted line, and $(k_x, k_z) = (1.48, 7.3)$ for the solid line.

maximum in the wavenumber plane is away from both axes ($k_x k_z \neq 0$). The reason for this energy gain is identified as the combination of Orr and lift-up mechanisms (Farrell & Ioannou 1993*a*; Arratia 2011). Farrell & Ioannou (1993*b*) showed that it is universal in shear flows, the wall-normal velocity v, raised by the Orr mechanism, can give rise to the streamwise velocity u through the lift-up mechanism. The energy gain is maximised by the combination process, especially for short time intervals.

The comparison between Orr and lift-up mechanisms is shown in figure 4.15(b). In unstratified plane Poiseuille flow, the growth of spanwise-uniform perturbations is much smaller than that of oblique and streamwise-uniform perturbations nearly for all times. Three-dimensional perturbations grow faster over shorter time intervals than the two-dimensional ones, meaning that the Orr mechanism is less efficient than the lift-up mechanism for transient grow in the three-dimensional shear flow. However, the growth of oblique wave, which results from the combination of the two fundamental mechanisms, dominates in the short time interval $T \in [1, 18.5]$ in figure 4.15(b). Reddy & Henningson (1993) also noted that this combination process is important because the transition to turbulence usually occurs earlier than the time when $G_m(T)$ achieves its maximum (Henningson *et al.* 1993), and there are more nonlinear interactions for this kind of oblique waves.

It should be noted that the k_x interval in figure 4.14 is $[0, 0.2]$, while $k_x \in [0, 5]$ in figure 4.15. This may explain the long branch in the right part of figure 4.14, and this branch is connected to the region associated with the TS wave. This region is revealed in figure 4.15 due to the extension of k_x interval. Approximately, the wavenumber intervals for the region associated with viscous modes are $k_x \in [0, 2]$ and $k_z \in [0, 0.5]$, which is the

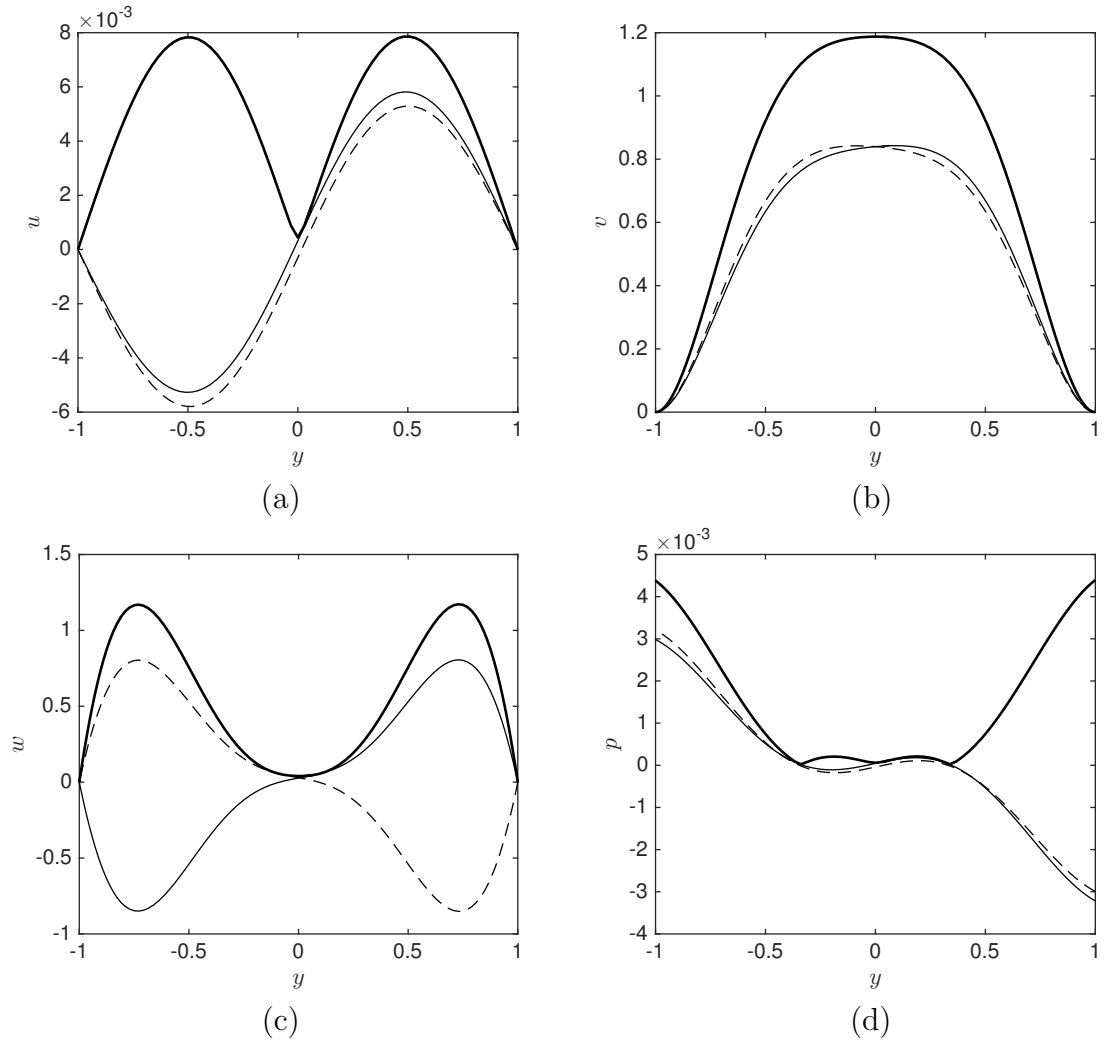

FIGURE 4.16 – Structures of the optimal initial conditions for the parameters $Re = 5000$, $F = \infty$, $k_x = 0$, $k_z = 2.044$, $t = 0$, (terminal time $T = 379$). (a) streamwise velocity u; (b) normal velocity v; (c) transverse velocity w; (d) pressure p; Thick solid lines, thin solid lines and dashed lines represent absolute value, real part and imaginary part, respectively. All variables are normalized by the total energy E_0 at the initial time.

same region as the least stable eigenmodes.

The maximal energy gain results shown in figure 4.14 and 4.15 are consistent with the values obtained by Butler & Farrell (1992). The spatial structures of the optimal initial conditions are shown in figure 4.16, which is associated with the maximal energy gain G_m in figure 4.14. Moreover, the corresponding optimal response at the terminal time $T = 379$ are illustrated in figure 4.17.

As illustrated in figure 4.16, the optimal initial conditions contain very small streamwise velocity u when normalized by the initial total perturbation energy E_0, while the maximum absolute values of normal velocity v and transverse velocity w are of the same order. The velocity field of the initial disturbances represents streamwise-uniform vortices. However, at terminal time $T = 379$, the maximum absolute value of u is nearly 200 times larger than v and w (see figure 4.17). The formation of the initial disturbances and large

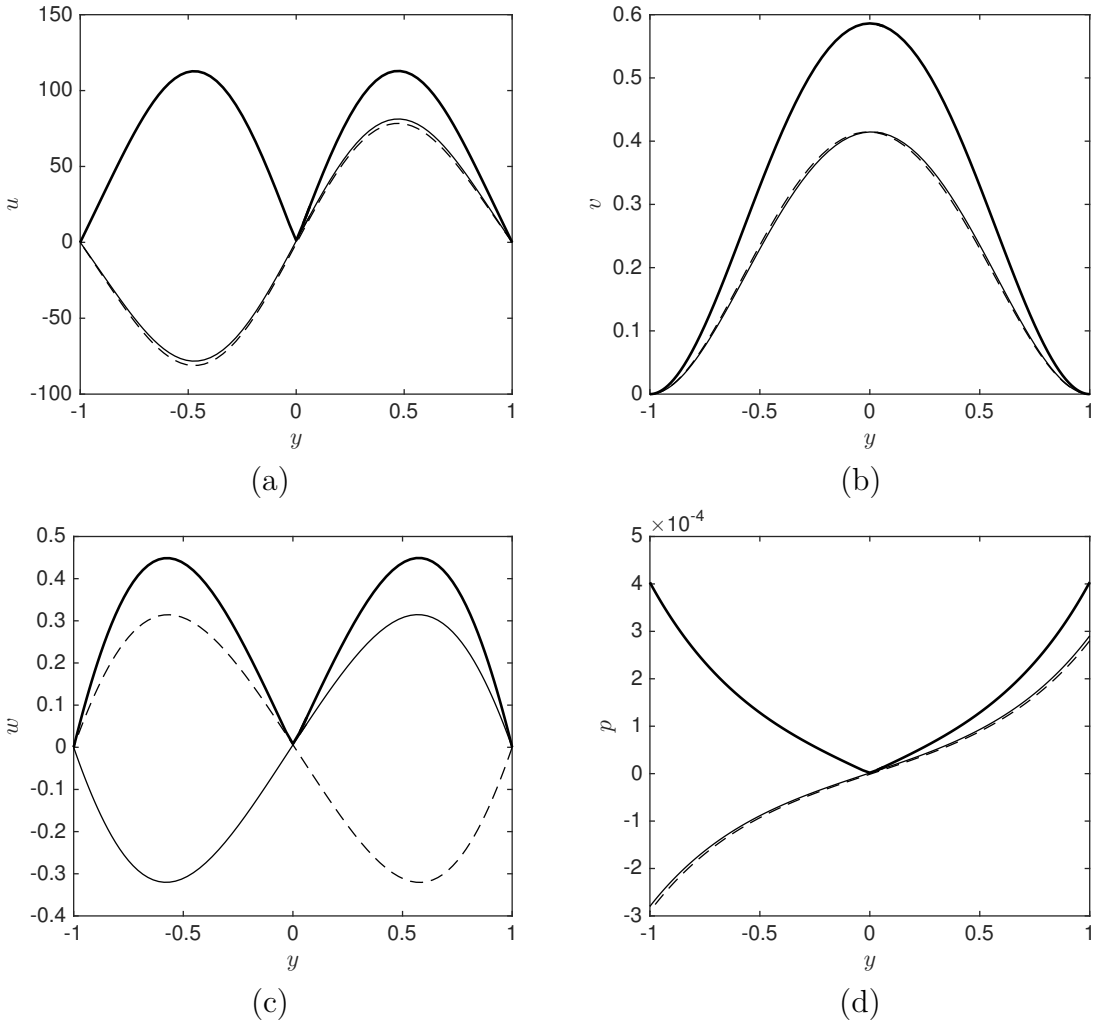

FIGURE 4.17 – Structures of the physical variables at terminal time for the parameters $Re = 5000,\ F = \infty,\ k_x = 0,\ k_z = 2.044,\ T = 379$. (a) streamwise velocity u; (b) normal velocity v; (c) transverse velocity w; (d) pressure p; Thick solid lines, thin solid lines and dashed lines represent absolute value, real part and imaginary part, respectively. All variables are normalized by the total energy E_0 at the initial time.

growth in the streamwise velocity agree with the characteristics expected for the lift-up mechanism (Ellingsen & Palm 1975; Landahl 1980).

4.3.2 Eigenfunctions and optimal perturbations

The correlation between eigenvalues and the structure of physical perturbations are verified in this part. Farrell (1988) showed that the unstable mode does not gain the most perturbation energy and the initial conditions that grow fastest in the short-time transient phase is a linear combination of different eigenfunctions. However, for long-time evolutions in the fluid, the optimal spatial structures of the physical perturbations should be determined by the dominant eigenmode and the adjoint of it. The 'direct' and 'adjoint' eigenfunctions set the optimal response at terminal time ($t = T$) and the initial disturbances at the start ($t = 0$), respectively.

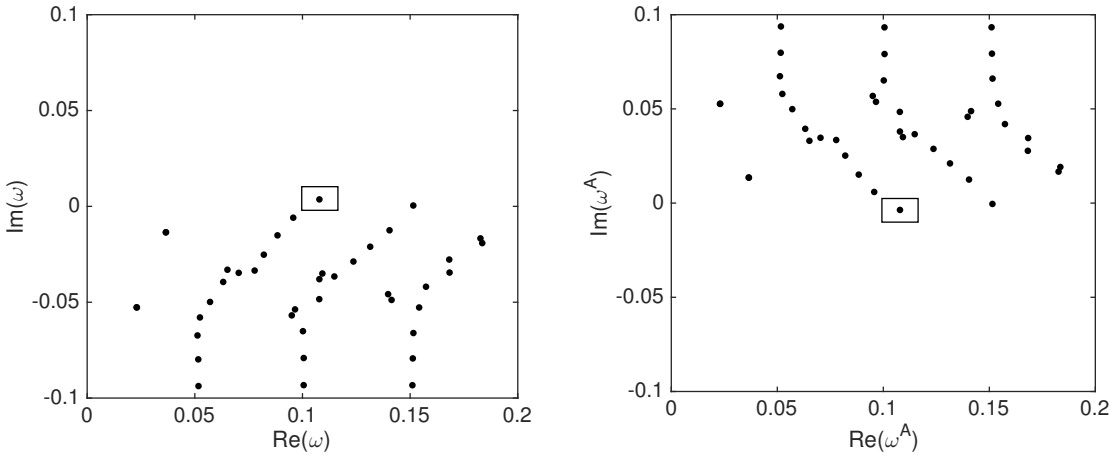

FIGURE 4.18 – Spectrum of the eigenvalues for the parameters $Re = 5000,\ F = 20,\ k_x = 0.1507,\ k_z = 2.888$. (a) 'Direct' spectrum, the eigenvalue marked in the small rectangle is $\omega = 0.1079 + 0.0036i$; (b) 'Adjoint' spectrum, the eigenvalue marked in the small rectangle is $\omega^A = 0.1079 - 0.0036i$. The most unstable 'direct' mode and the 'adjoint' mode marked in rectangles are the modes that determine the structures of the perturbations at terminal time and initial time.

The 'direct' spectrum of the eigenvalues for an exponentially unstable stratified fluid ($Re = 5000,\ F = 20$) is illustrated in figure 4.18(a). The 'adjoint' eigenvalues are the complex conjugate of the 'direct' ones, as seen in figure 4.18.

The most unstable mode in the direct spectrum determines the behaviour of the fluid when $T \to \infty$. When the time interval for the transient phase is long enough (e.g. T=379 for this case), this phenomenon can also be verified by the physical structures of the optimal response at the terminal time. The spatial structure of the most unstable mode and of the optimal perturbation at final time $T = 379$ are shown in figure 4.19 and figure 4.20, respectively. As we have expected, there is little difference between the spatial structures in these two figures. Similarly, the spatial structures of the most unstable adjoint mode and of the initial optimal perturbations are shown in figure 4.21 and 4.22. Again, we obtain a good agreement of these two structures.

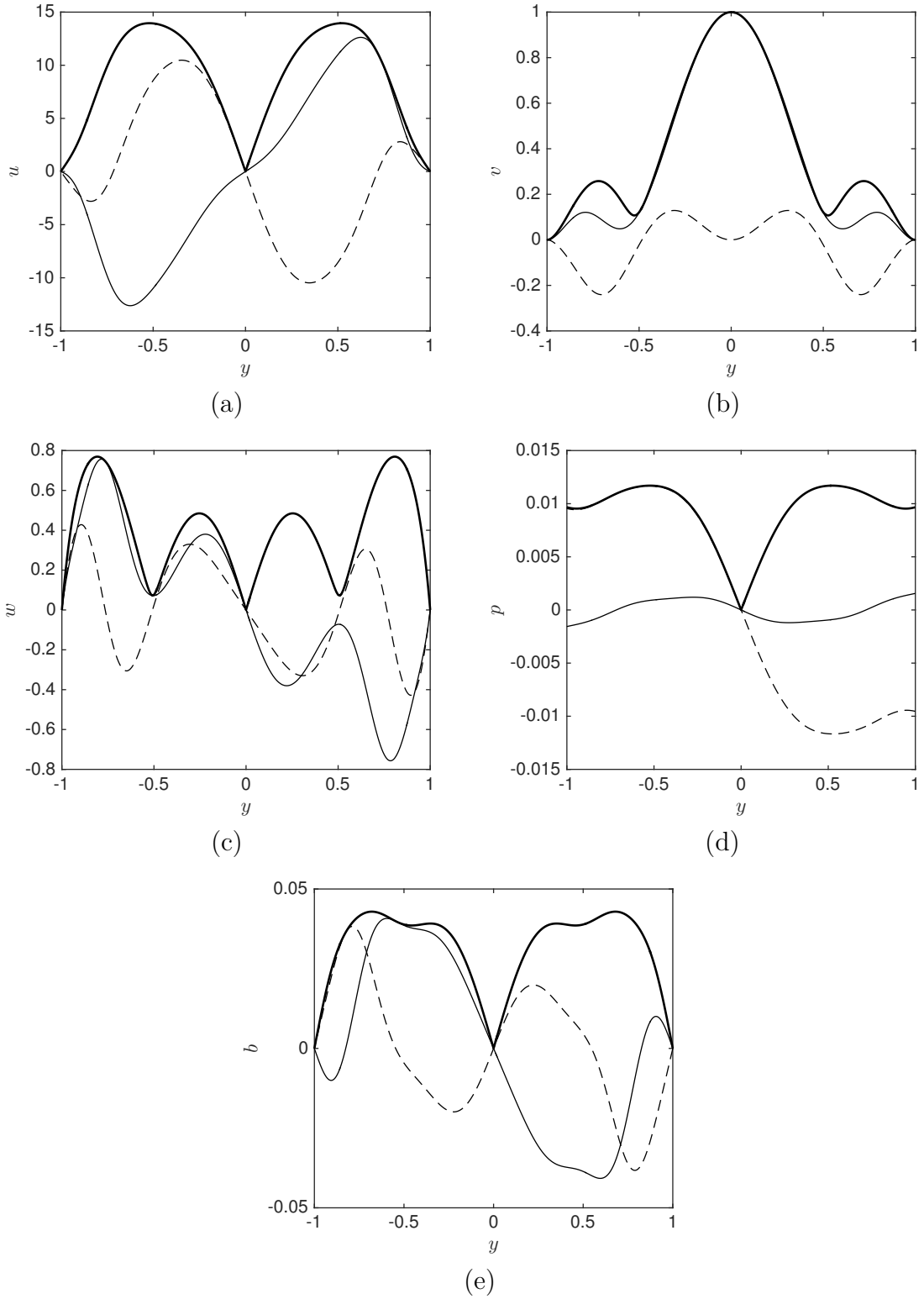

FIGURE 4.19 – Eigenfunctions associated with the unstable mode for the parameters $Re = 5000,\ F = 20,\ k_x = 0.1507,\ k_z = 2.888,\ \omega = 0.1079 + 0.0036i$. (a) streamwise velocity u; (b) normal velocity v; (c) transverse velocity w; (d) pressure p; (e) buoyancy b; Thick solid lines, thin solid lines and dashed lines represent absolute value, real part and imaginary part, respectively. All eigenfunctions are normalized by v(0).

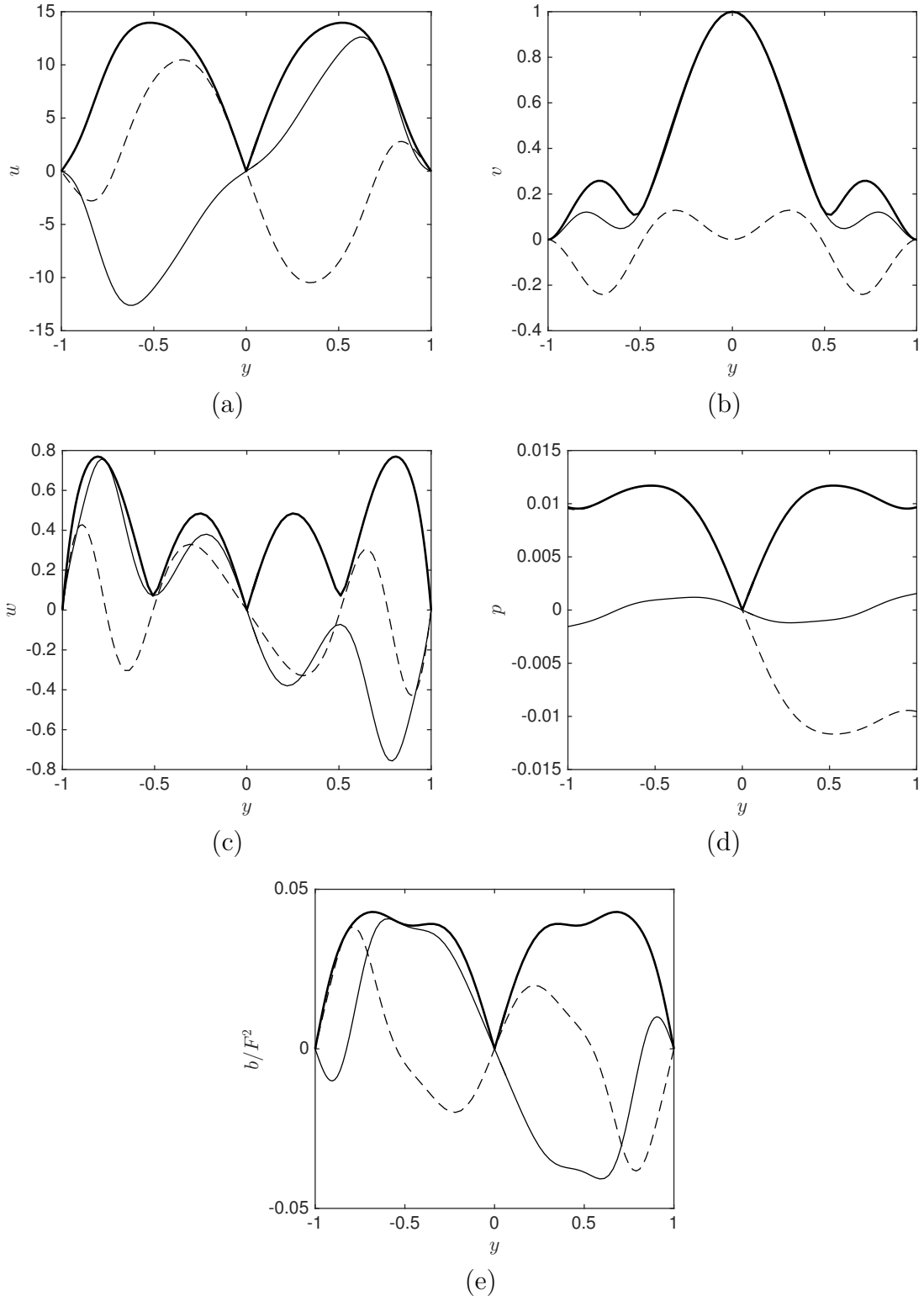

FIGURE 4.20 – Structures of the physical variables at terminal time, the associated parameters are $Re = 5000,\ F = 20,\ k_x = 0.1507,\ k_z = 2.888,\ T = 379$. (a) streamwise velocity u ; (b) normal velocity v ; (c) transverse velocity w ; (d) pressure p ; (e) buoyancy b/F^2 (the definitions of b for eigenvalues and optimal perturbations are slightly different, see Chapter 2 for details). Thick solid lines, thin solid lines and dashed lines represent absolute value, real part and imaginary part, respectively. All variables are normalized by v(0).

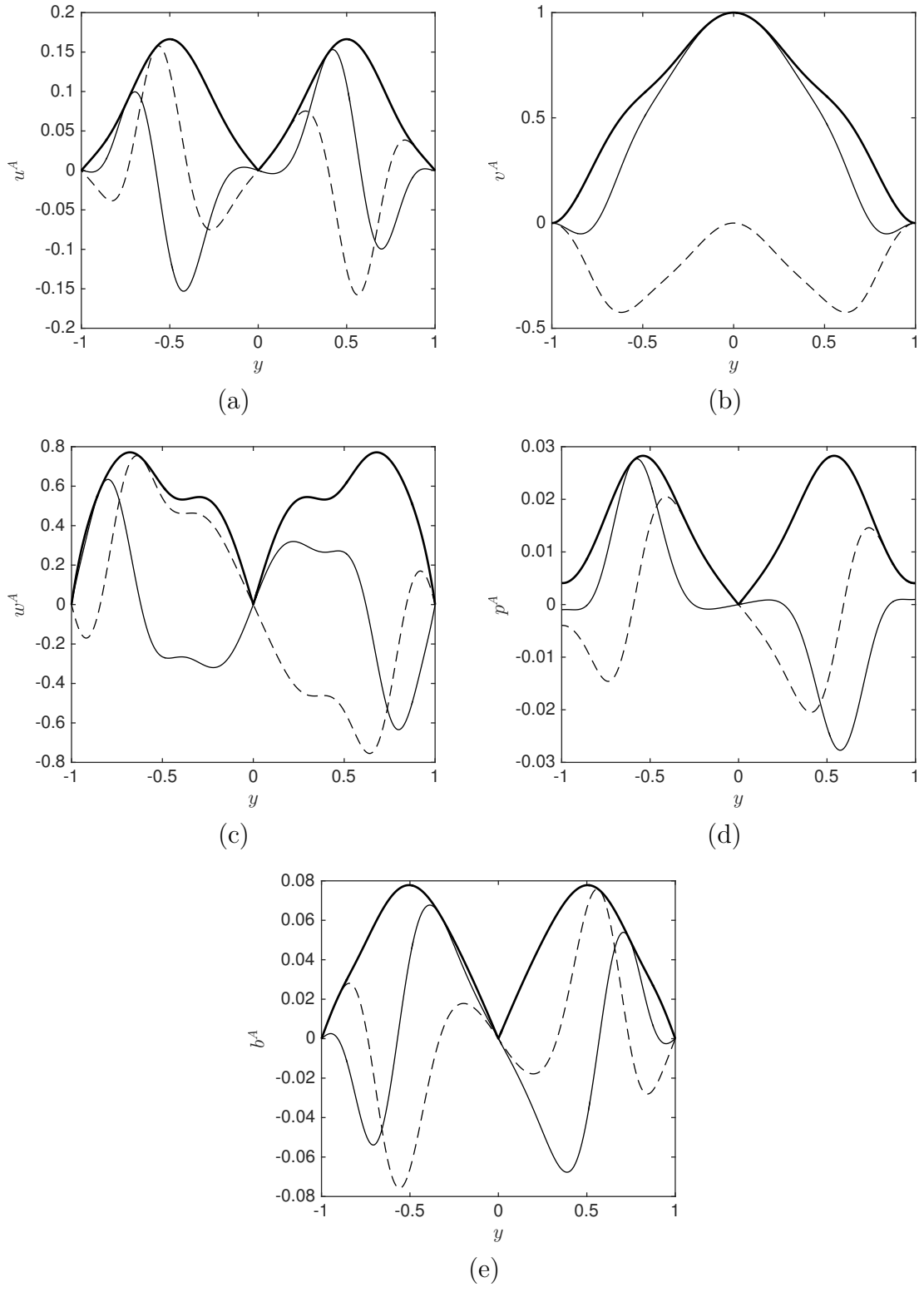

FIGURE 4.21 – Eigenfunctions associated with the adjoint mode for the parameters $Re = 5000,\ F = 20,\ k_x = 0.1507,\ k_z = 2.888,\ \omega^A = 0.1079 - 0.0036i$. (a) adjoint streamwise velocity u^A ; (b) adjoint normal velocity v^A ; (c) adjoint transverse velocity w^A ; (d) adjoint pressure p^A ; (e) adjoint buoyancy b^A ; Thick solid lines, thin solid lines and dashed lines represent absolute value, real part and imaginary part, respectively. All eigenfunctions are normalized by $v^A(0)$.

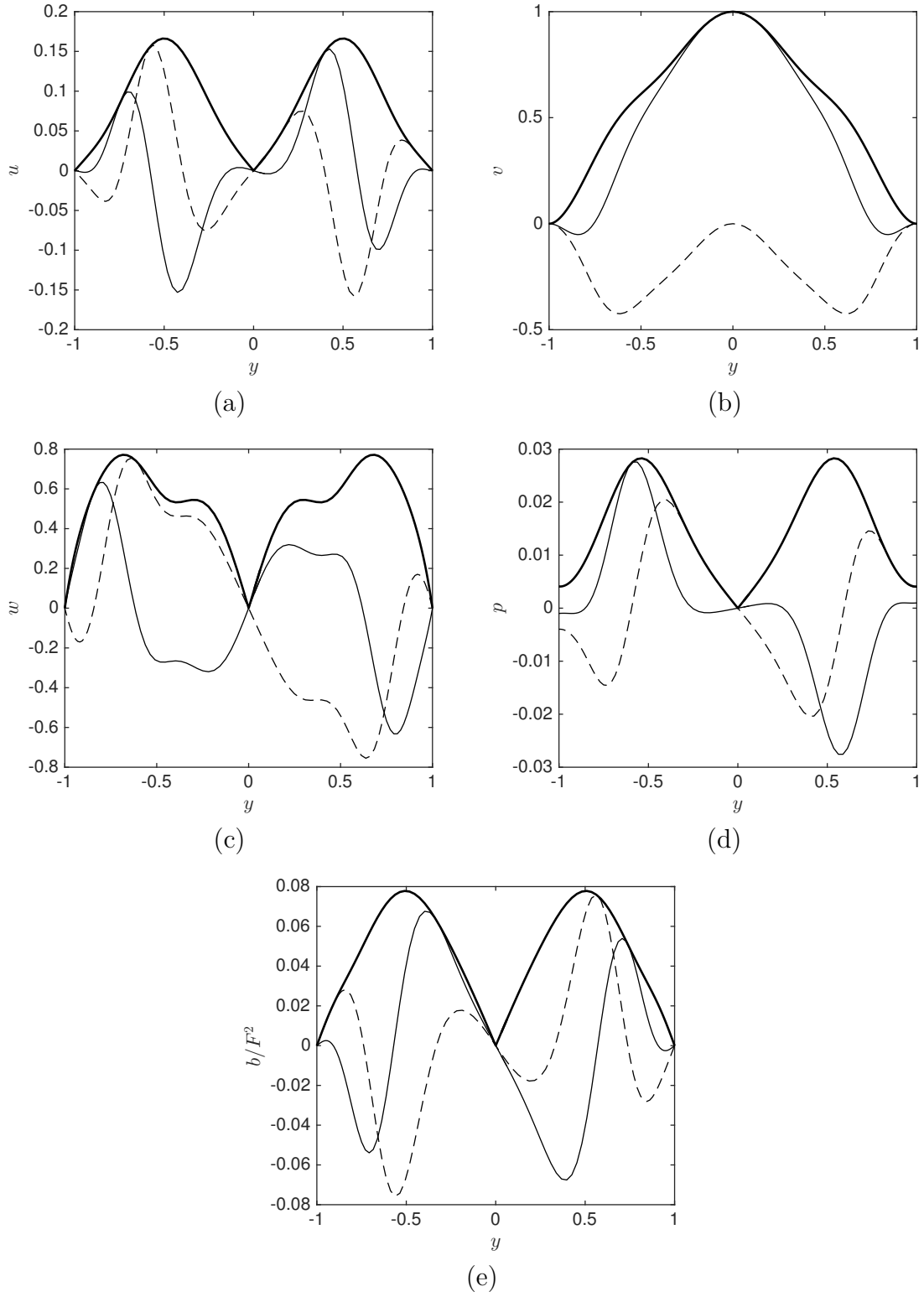

FIGURE 4.22 – Structures of the optimal perturbations at initial time, the associated parameters are $Re = 5000,\ F = 20,\ k_x = 0.1507,\ k_z = 2.888,\ t = 0$, (terminal time $T = 379$). (a) streamwise velocity u ; (b) normal velocity v ; (c) transverse velocity w ; (d) pressure p ; (e) buoyancy b/F^2 (the definitions of b for eigenvalues and optimal perturbations are slightly different, see Chapter 2 for details). Thick solid lines, thin solid lines and dashed lines represent absolute value, real part and imaginary part, respectively. All variables are normalized by $v(0)$.

4.3.3 Velocity field of transient growth

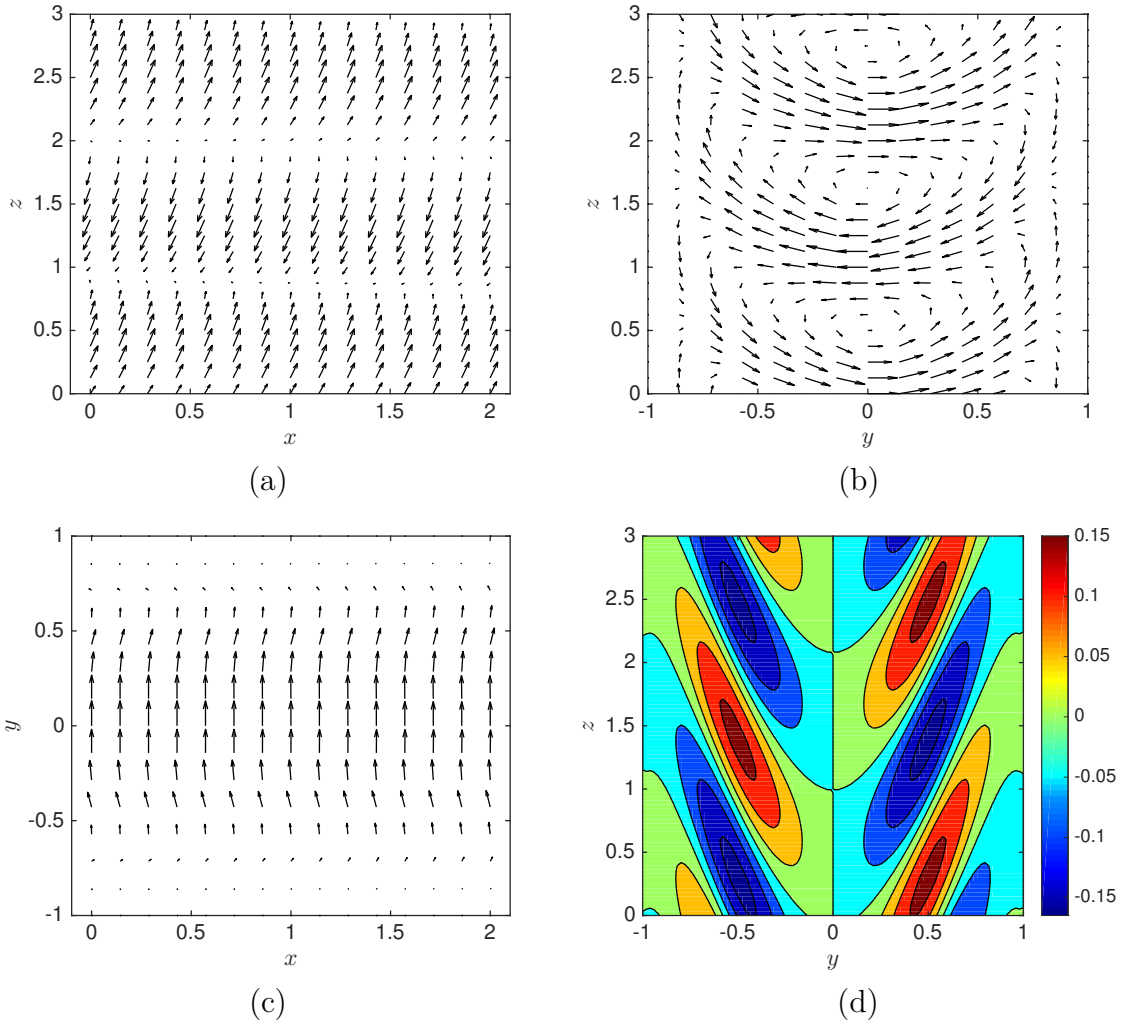

FIGURE 4.23 – Velocities of the optimal perturbations at initial time, the associated parameters are $Re = 5000$, $F = 20$, $k_x = 0.1507$, $k_z = 2.888$, $t = 0$, (terminal time $T = 379$). (a) Projections on the $x - z$ plane (streamwise velocity u and transverse velocity w on the plane $y = 0.5$); (b) Projections on the $y - z$ plane (normal velocity v and transverse velocity w on the plane $x = 0$); (c) Projections on the $x - y$ plane (streamwise velocity u and normal velocity v on the plane $z = 0$); (d) streamwise velocity u contours on plane $x = 0$, $|u|_{max} = 0.1572$. All velocities are normalized by $v(0)$ at initial time $t = 0$.

The velocity field of the optimal initial conditions is shown in figure 4.23 for the perturbations of figure 4.22. We observe that the streamwise velocity u is quite small compared to the velocities oriented in the other directions. Normalized by $v(0)|_{t=0}$, the contours of u in the $(y - z)$ plane is shown in figure 4.23(d) and the maximum absolute value is $|u|_{max} = 0.1572$. Thus, the optimal perturbations correspond to the nearly streamwise-uniform vortices, as shown in figure 4.23(b).

The structures of the corresponding optimal responses are illustrated in figure 4.24. The streamwise velocity u becomes dominant in figure 4.24(a,c) and the vortices are stretched in figure 4.24(b,d). The maximum absolute value in figure 4.24(d) is up to

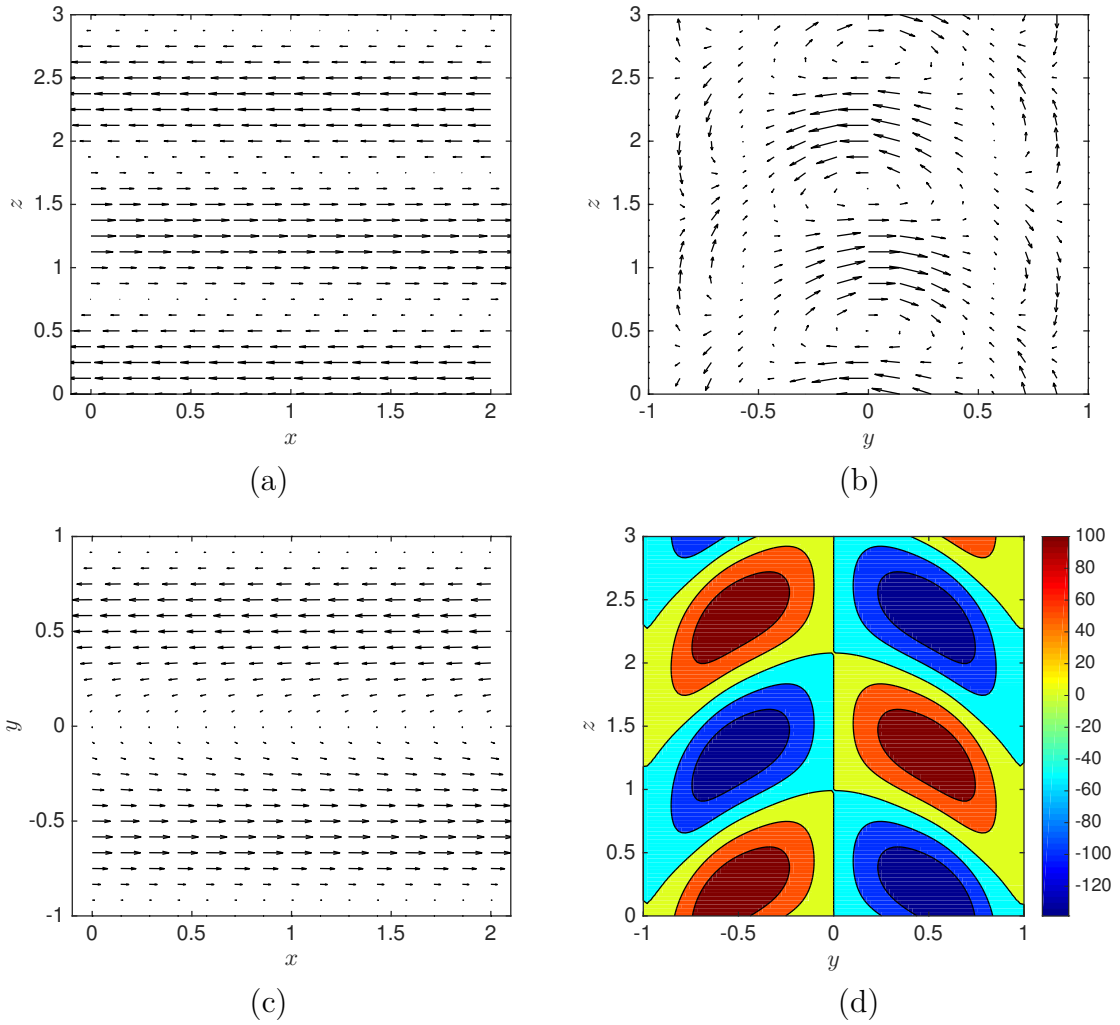

FIGURE 4.24 – Velocities of the optimal responses at terminal time ($t = T$), the associated parameters are $Re = 5000,\ F = 20,\ k_x = 0.1507,\ k_z = 2.888,\ T = 379$. (a) Projections on the $x-z$ plane (streamwise velocity u and transverse velocity w on the plane $y = 0.5$) ; (b) Projections on the $y-z$ plane (normal velocity v and transverse velocity w on the plane $x = 0$) ; (c) Projections on the $x-y$ plane (streamwise velocity u and normal velocity v on the plane $z = 0$) ; (d) streamwise velocity u contours on plane $x = 0$, $|u|_{max} = 138.7$, $G = 5524$. All velocities are normalized by $v(0)$ at initial time $t = 0$.

$|u|_{max} = 138.7$, which is approximately 882 times larger than the value at $t = 0$. The large growth in u could therefore correspond to the formulation of streamwise streaks.

As demonstrated by figure 4.19-4.22, the physical structures of the optimal initial conditions and responses for the long time interval ($T = 379$) are determined by the adjoint and direct eigenmode. However, the characteristics of the evolution in time present a behaviour that resembles the lift-up mechanism. Although Ellingsen & Palm (1975) and Landahl (1980) described the optimal initial conditions for the lift-up mechanism as streamwise-uniform vortices, in the presence of stratification, the streamwise wavenumber for the perturbations in figure 4.23 and 4.24 is non-zero ($k_x = 0.1507$). The features of the most unstable mode is similar to that of the lift-up mechanism : nearly streamwise vortices and the greatly amplified velocity u. In the following parts, we have shown that,

in the presence of stratification, the eigenmodes play an important role in the transient growth process, even if the time interval is finite.

4.3.4 Stratification effects on transient growth

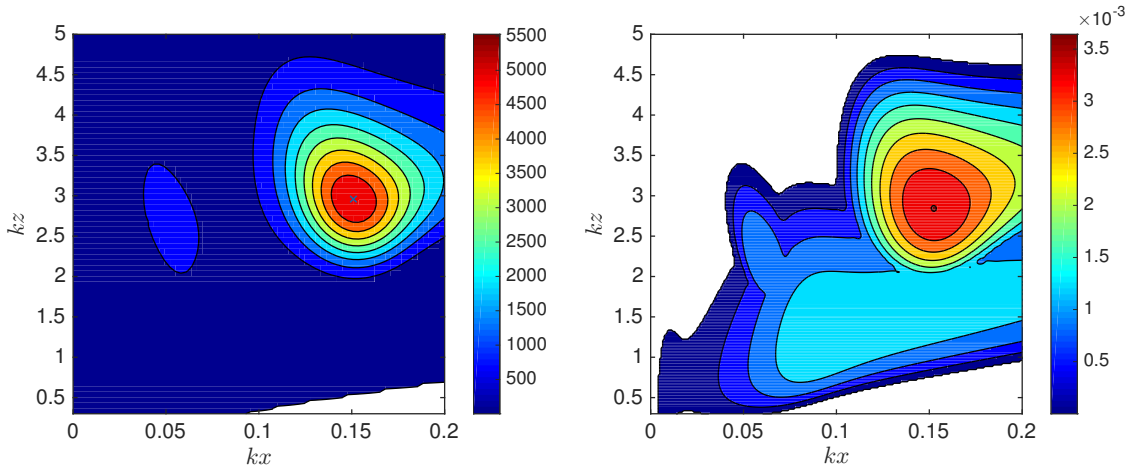

(a) (b)

FIGURE 4.25 – Contours in (k_x, k_z) plane for $Re = 5000$ and $F = 20$. (a) Energy gain $G(T)$ at $T = 379$. Contours are every 615 from 1 to 5524. (b) Growth rate ω_i. Contours are every 5×10^{-4} from 0 to 3.6×10^{-3}.

In this section, we focus on a region where viscous modes are stable ($Re \leqslant 5000$) in order to highlight the effect of the stratification which causes unstable gravity modes. We know that as $T \to \infty$, the transient growth analysis is equivalent to a modal analysis. For a finite time interval $T = 379$, there are differences between the results of modal and non-modal analysis, which are qualified in figure 4.25. The transient growth is thought to approach the exponentially unstable mode as $T \to \infty$, but in the presence of stratification, the unstable modes are shown to be important at finite times much earlier than those expected in the unstratified fluid.

The effect of the stratification on the energy gain can also be analysed by comparing figure 4.25(a) and 4.14. The comparison shows that the energy gain in stratified flow is slightly larger than that in the unstratified case for the same Reynolds number and time interval ($Re = 5000,\ T = 379$). The maximum in figure 4.25(a) is located at $(k_x, k_z) = (0.1507, 2.9565)$ and $G_m = 5524$. On the other side, in figure 4.25(b), the eigenvalue with the largest growth rate is $\omega = 0.1091 + 0.0036i$ and the corresponding wavenumbers are $(k_x, k_z) = (0.1526, 2.848)$. This set of wavenumbers is very close to that of the maximum energy gain G_m in the (k_x, k_z) plane, meaning that G_m is mainly determined by the most unstable mode. The other local peaks in figure 4.25(a) with non-zero streamwise wavenumbers are also believed to result from an unstable eigenmode visible in figure 4.25(b).

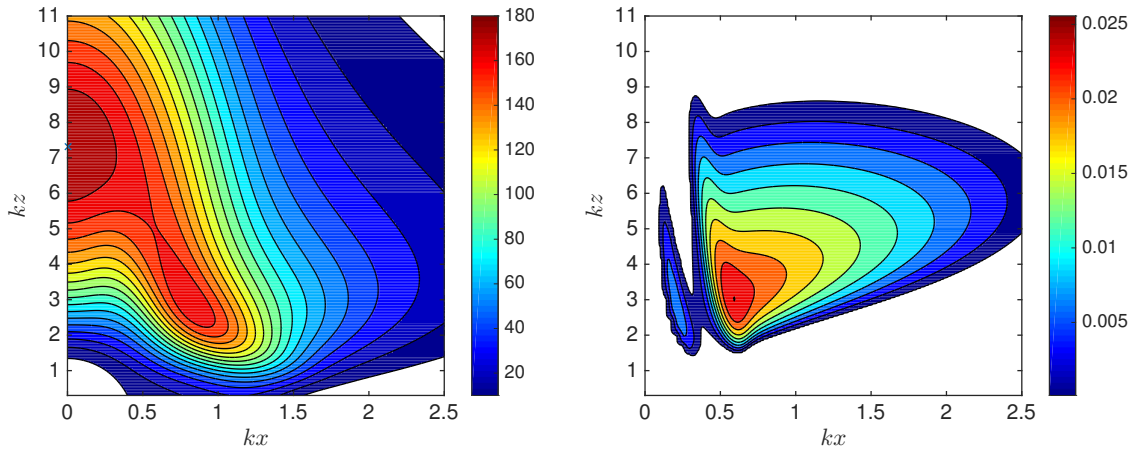

(a) (b)

FIGURE 4.26 – Contours in (k_x, k_z) plane for $Re = 5000$ and $F = 4$. (a) Energy gain $G(T)$ at $T = 25$. Contours are every 10 from 10 to 180. (b) Growth rate ω_i. Contours are every 2.5×10^{-3} from 0 to 2.5×10^{-2}.

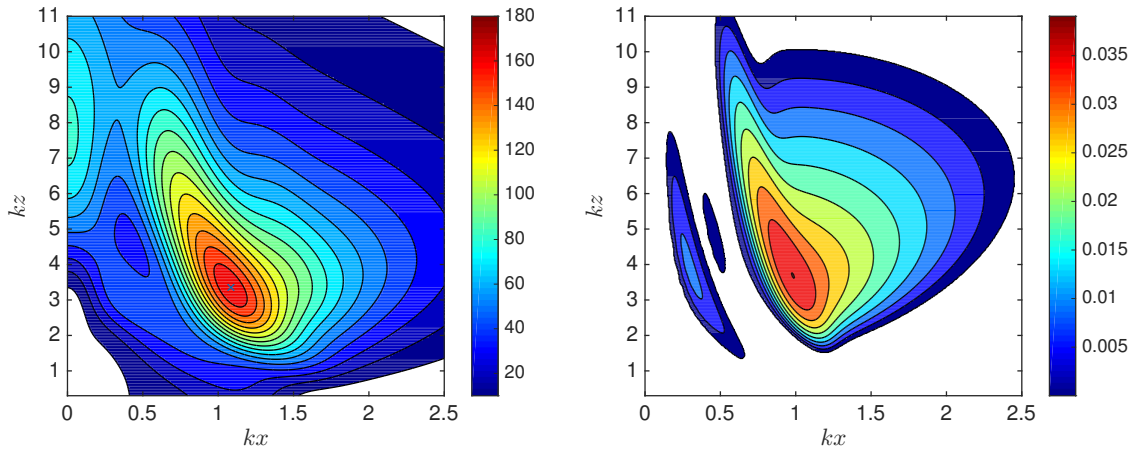

(a) (b)

FIGURE 4.27 – Contours in (k_x, k_z) plane for $Re = 5000$ and $F = 2$. (a) Energy gain $G(T)$ at $T = 25$. Contours are every 10 from 10 to 167.5. (b) Growth rate ω_i. Contours are every 4×10^{-3} from 0 to 4×10^{-2}.

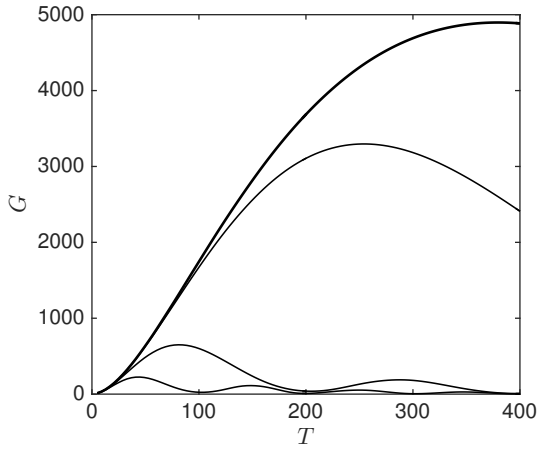

FIGURE 4.28 – Energy gain $G(T)$ for $Re = 5000$, $k_x = 0$, $k_z = 2.04$ and various Froude numbers (from up to down $F = \infty,\ 100,\ 20,\ 10$).

If the time interval is short, the influence of unstable modes is less visible so that the energy gain at $k_x = 0$ can become the maximum, as in the unstratified case. This case is illustrated in figure 4.26(a) for $F = 4$. The maximal energy gain is $G_m = 179.7$, and the wavenumbers that maximize the energy gain are $(k_x, k_z) = (0, 7.304)$. This energy gain is due to the lift-up mechanism. The second highest peak of energy gain in figure 4.26(a) gives $G = 167.3$ at $(k_x, k_z) = (0.8133, 2.921)$. It results from the influence of unstable gravity modes. This influence can be proved by the comparison to growth rate contours for the same basic parameters, which are illustrated in figure 4.26(b). The maximum growth rate is $\omega_i = 0.0256$ at $(k_x, k_z) = (0.5924, 3.007)$. The comparison displayed in figure 4.26(a,b) suggests that, for short time intervals (e.g. $T = 25$), the lift-up mechanism can dominate the influence of unstable modes, but the transient growth of unstable modes have already become essential.

The influence of unstable modes becomes more obvious with stronger stratification (e.g. $F = 2$). As illustrated in figure 4.27(a), the maximal energy gain, $G_m = 167.5$ at $(k_x, k_z) = (1.084, 3.351)$, corresponds to the largest growth rate $\omega_i = 0.0391i$ at $(k_x, k_z) = (0.974, 3.74)$ in figure 4.27(b). The second highest peak of the energy gain in figure 4.27(a) is $G_m = 82.6$ at $(k_x, k_z) = (0, 7.648)$. It is located on the k_x-axis, as for the lift-up mechanism, and in the same region of spanwise/transverse wavenumbers (k_z) as figure 4.26(a). However, the gain is weaker than the one in the previous two cases ($F = \infty$ and $F = 4$), meaning that the stratification has a stabilising effect on the lift-up mechanism.

This stabilising effect is clearly seen in figure 4.28. The maximum of the energy gain is achieved earlier as the stratification becomes stronger, while the value of the maximal energy gain becomes smaller. Stratification hinders vertical displacement. It is thus quite intuitive that it will not favour the formulation of the streamwise vortices involved in the lift-up mechanism.

Compared to the unstratified case (figure 4.15), the combination of Orr and weakened

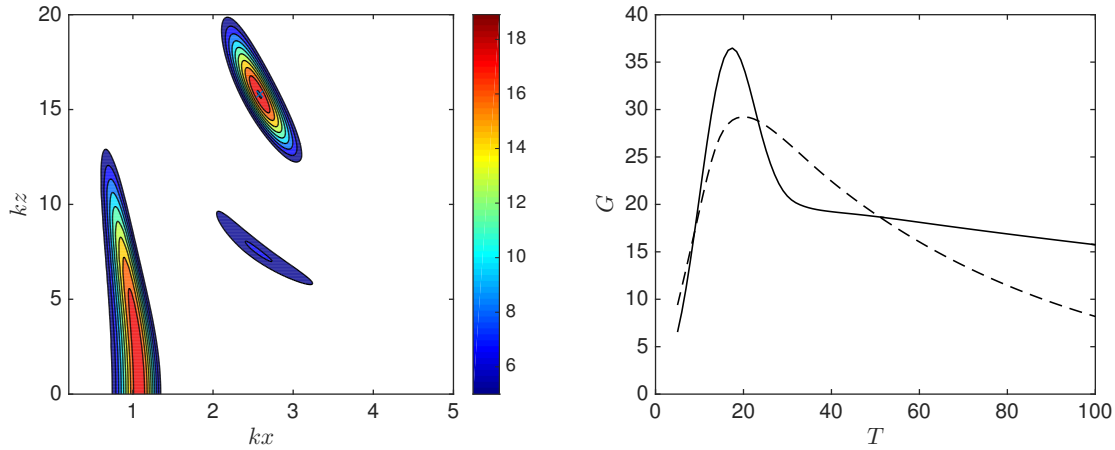

(a) (b)

FIGURE 4.29 – Energy gain G for strongly stratified plane Poiseuille flow, the associated parameters are $Re = 5000$, $F = 0.259$. (a) Contours in (k_x, k_z) plane with $T = 50$. Contours are every 1.55 from 5 to 19. (b) Comparison of $G(T)$ for two different sets of wavenumbers. $(k_x, k_z) = (1.075, 0)$ for the solid line, and $(k_x, k_z) = (2.586, 15.75)$ for the dashed line.

lift-up mechanism is not strong enough to be dominant (see figure 4.26 and 4.27). However, in the region of non-zero wavenumbers ($k_x k_z \neq 0$), the combination is amplified by the 3D gravity mode (relative to the other regions). Therefore, in figure 4.26 and 4.27, another peak appears in the contours of G in the (k_x, k_z) plane. This peak becomes more important as the stratification becomes stronger.

The transient growth for a strongly stratified Poiseuille flow without unstable eigenvalues are also examined. The energy gain contours for $Re = 5000$ and $F = 0.259$ are shown in figure 4.29(a).

There are three separate regions and each contains a local peak. These regions can mainly be associated with eigenvalues. The eigenvalues of TS waves mainly contribute to the left-most part. The other two parts are the results of 3D gravity modes in the presence of stratification. We also compared the energy growth of 2D ($k_z = 0$) and 3D ($k_x k_z \neq 0$) perturbations as functions of T in figure 4.29(b). The 2D transient growth reaches its maximum earlier, but the growth of the 3D perturbations becomes larger for a short period ($T \in [23, 50]$). The steep peak demonstrated by the curve of 2D perturbations can be explained by the deformation process of the Orr mechanism. When the spanwise-uniform vortices are sheared into the downstream direction, the energy gain G reaches its maximum at the time when the vortices are in the cross-stream direction, and soon decreases after that moment.

The energy gains G for various Froude numbers are represented as functions of transverse wavenumber k_z in figure 4.30(a). The unchanged values $G(k_z = 0) = 45.7$ shows that the transient growth of the two-dimensional disturbances ($k_z = 0$) are independent of the vertical stratification. The Orr mechanism is also proved to be unaffected. However, the

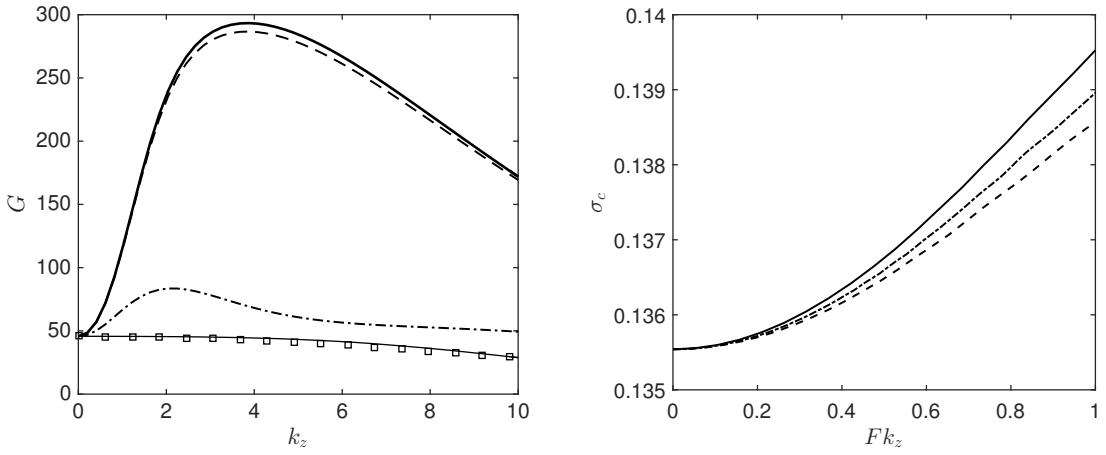

(a) (b)

FIGURE 4.30 – Energy gain G as a function of spanwise wavenumber k_z and the self-similarity in strongly stratified flow. (a) Energy gain for various Froude numbers (from up to down $F = \infty,\ 20,\ 2,\ 0.2$). The markers '□' represent $F = 0.1$. (b)The corrected mean growth rate σ_c. The solid, dash-dotted, dashed lines represent $F = 0.05,\ 0.1,\ 0.2$ respectively. The associated parameters are $Re = 5000, k_x = 1.48, T = 14.1$

energy gains associated with non-zero transverse wavenumbers ($k_x k_z \neq 0$) are reduced as the Froude number decreases. As this transient growth is associated with a combination of Orr and lift-up mechanisms, the reduction in G can thus be explained by the weakening of the lift-up mechanism.

In the limit of strong stratification ($F \to 0$), Billant & Chomaz (2001) demonstrated the self-similarity of strongly stratified inviscid flows. Accounting for the viscosity, Arratia (2011) showed that the self-similar form is

$$\sigma_m\left(k_x, k_z, T, Re, F\right) \approx \sigma_c\left(k_x, Fk_z, T\right) - \frac{k_z^2}{Re} \tag{4.4}$$

where σ_m is the mean growth rate defined by

$$\sigma_m = \frac{\ln G}{2T}. \tag{4.5}$$

The equation (4.4) is the corrected form of the self-similarity found by Deloncle *et al.* (2007) and Arratia (2011) for the inviscid flows in the presence of strong stratification ($F \ll 1$). The corrected mean growth rate σ_c is shown as a function of Fk_z in figure 4.30(b). We can see that the curves of $F = 0.05,\ 0.1,\ 0.2$ are close to each other.

To illustrate the effect of viscosity, we examined some highly viscous cases. As we have shown above, the associated eigenvalues highly influence the contours of the energy gain, and there is a 'valley' shown by the growth rate contours in figure 4.13. The parameters $Re = 686.6$ and $F = 5.969$ form an interesting case as it corresponds to a point in this 'valley'. The energy gain contours for this case are illustrated in figure 4.31(a). Only one peak appears at the line $k_x = 0$ and the maximal energy gain is $G_m = 40.94$, the associated wavenumbers are $(k_x, k_z) = (0, 3.05)$. The energy gain contours in figure 4.31(a)

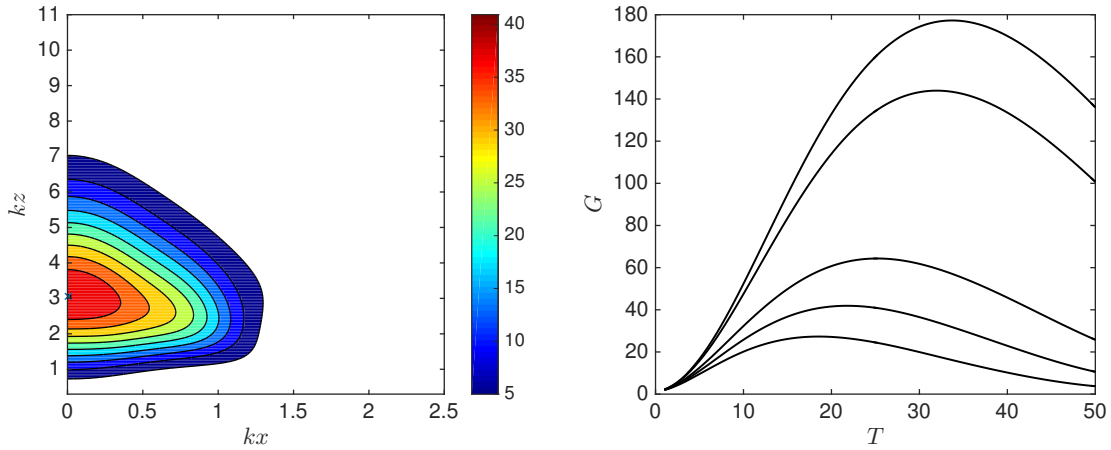

FIGURE 4.31 – Energy gain G for different Reynolds numbers with $F = 5.969$. (a)Energy gain contours in (k_x, k_z) plane for $Re = 686.6$ at time $T = 25$. Contours are every 4 from 5 to 41. (b)Energy gain for different Reynolds numbers (from up to down $Re = 5000,\ 3000,\ 1000,\ 686.6,\ 500$) at constant F. The associated wavenumbers are $(k_x, k_z) = (0, 3.05)$.

shows that the total perturbation energy grows via the lift-up mechanism. The effect of viscosity is shown in figure 4.31(b). As Re grows, the maximal energy gain increases and so does the terminal time for the maximum growth. Although Biau & Bottaro (2004) and Jerome *et al.* (2012) showed that the maximum energy gain in the plane Poiseuille flow is proportional to Re^2 and the corresponding time increases as Re under both stable and unstable temperature gradient, the scaling law presented by Gustavsson (1991), Butler & Farrell (1992) and Reddy & Henningson (1993) is for the global maximum $G_{global} = \max_{\forall k_x, k_z, T} G$ in unstratified fluid. The growth displayed in figure 4.31(b) is not optimised over all wavenumbers, and only the tendency of the scaling law is kept by the curves of $G(T)$.

4.4 Discussion

In this chapter, we have performed a modal and non-modal analysis of a plane Poiseuille flow with stable stratification in the vertical direction. In the modal analysis, we have shown that in the presence of stratification, the plane Poiseuille flow is unstable to two-dimensional viscous instability and three-dimensional instability. The generation of the three-dimensional instability derives from the resonance of inviscid modes and viscous modes. The resonance mechanism is similar to that involved in the strato-rotational instability (Le Dizès & Riedinger 2010). The three-dimensional instability is shown to exist in the region $480 \leqslant Re \leqslant 5000$, which is a subcritical interval for the viscous instability. The largest growth rate ($\omega_i \approx 0.05$) appears around $F = 1$ for large Reynolds numbers ($Re = 5000$). The unstable interval of the Froude number is $0.27 \leqslant F \leqslant 258$ for $Re = 5000$.

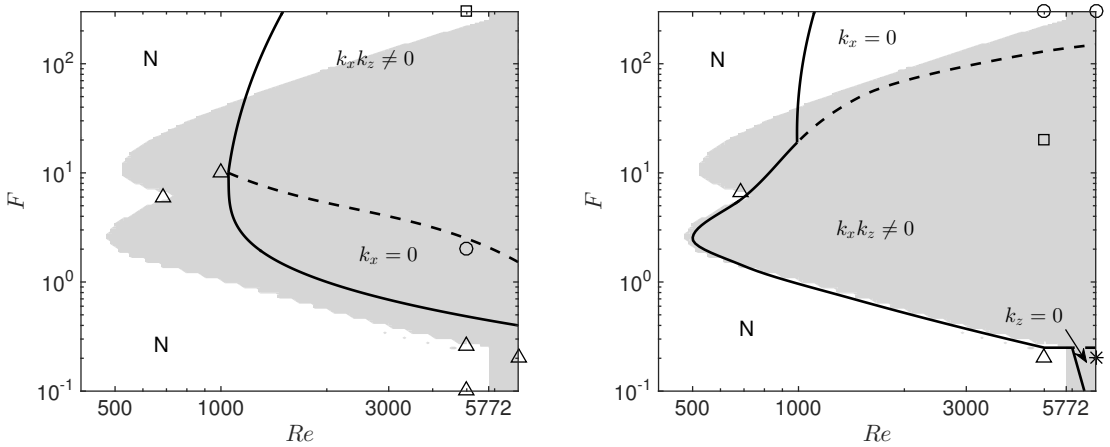

FIGURE 4.32 – Description of the optimal perturbations in the (Re, F) plane for a short time interval $T = 25$ (a) and a long time interval $T = 379$ (b). Three regions are identified according to the wavenumbers $k_x = 0$, $k_z = 0$, $k_x k_z \neq 0$. The regions are delimited by dashed lines. The solid line delimits the region with sufficiently large growth (typically $G(T) > 100$). The region in grey is the unstable region predicted by the modal analysis. Markers : 'N' represents 'No significant energy growth'. The symbols '$\circ$', '$\triangle$', '$\square$' and '$*$' correspond to the verified cases in different regions.

The non-modal analysis has been performed using the conventional 'Direct-Adjoint-Loop' method (Schmid 2007). We have described the effects of stratification on the transient growth and on the selection of optimal initial perturbations. The unstable eigenmodes we found in the modal analysis have been shown to have a significant influence on the transient growth. The optimal perturbations for the unstratified flows presented in this chapter agree with results obtained by Butler & Farrell (1992) and Reddy & Henningson (1993). The three fundamental mechanisms discussed in these papers have been examined in the presence of stratification. For short time intervals, the Orr mechanism (Orr 1907), which leads to the growth of spanwise-uniform vortices through the action of the Reynolds stress, is not affected by the stable stratification in the vertical direction. The expression of equation (2.10) also explains this fact. The lift-up mechanism (Ellingsen & Palm 1975; Landahl 1980) that leads to substantial growth of streamwise velocity perturbations and the formulation of streamwise-uniform vortices is weakened by the stable stratification. The combination of these two mechanisms (Farrell & Ioannou 1993*a*; Arratia *et al.* 2013), which leads to the growth of tilted roll vortices, is amplified by the 3D unstable modes (the 'gravity mode') in the presence of stratification. For long time intervals, the transient growth is mainly dominated by the most unstable eigenmodes.

The results of transient growth are consistent with what we have demonstrated in equation (2.10). Viscosity and stratification dissipate the perturbation energy. The contributor to the growth of the total energy is related to the Reynolds stress, and the energy is extracted from the mean shear, which is also universal in inviscid and unstratified fluids (Butler & Farrell 1992).

Figure 4.32(a) $T = 25$				
Marker	Re	F	$G(k_x, k_z)$	Region
◯	5000	4	$G(0, 7.2) = 179.6$	$k_x = 0$
□	7000	0.2	$G(1.0, 6.3) = 43.0$	$k_x k_z \neq 0$
	5000	300	$G(0.7, 2.9) = 699.5$	
△	5000	0.1	$G(1.1, 0) = 26.1$	No significant energy growth
	5000	0.26	$G(1.0, 6.8) = 30.9$	
	1000	10	$G(0.4, 2.9) = 96.7$	
	686.6	6	$G(0, 3.0) = 40.9$	

Figure 4.32(b) $T = 379$				
Marker	Re	F	$G(k_x, k_z)$	Region
◯	5000	300	G(0,2.1)=4568	$k_x = 0$
	7000	300	$G(0, 2.3) = 8412$	
$*$	7000	0.2	$G(1.0, 0) = 86.6$	$k_z = 0$
□	5000	20	$G(0.2, 3.0) = 5523$	$k_x k_z \neq 0$
△	5000	0.2	$G_m < 1$	No significant energy growth
	686.6	6.65	$G_m < 10$	

TABLE 4.2 – Positions of the markers in figure 4.32

The different regimes for the optimal perturbation are summarised in figure 4.32. The corresponding parameters and values are presented in table 4.2. Note that for short time intervals (e.g. $T = 25$), the transient growth is $\mathcal{O}(10 - 100)$ in strongly stratified flows or highly viscous flows, even if they are expected to be exponentially stable. The reasons for the growth are the three-dimensional eigenmode ($k_x k_z \neq 0$) or lift-up mechanism ($k_x = 0$). Since the result is not optimised over all the terminal time, the global maximum growth could be larger than the values we have shown.

As demonstrated in figure 4.32, the optimal initial disturbances in most regions are tilted roll vortices ($k_x k_z \neq 0$). The nonlinear effects on these perturbations are expected to be richer (Reddy & Henningson 1993) than those on the streamwise-uniform perturbations. Moreover, nonlinear effects can be destabilizing and provides even larger energy gain (Schmid 2007; Luchini & Bottaro 2014). It is therefore possible that a faster transition to a strongly nonlinear regime is reached in the the presence of stratification.

Chapitre 5

Conclusion and perspective

Stratification effects have been analysed in the context of boundary layer and channel flows.

In chapter 3, we have examined the stability of a stratified, viscous boundary layer using modal analysis. Various aspects of the instability have been analysed as functions of the Reynolds number and the Froude number. We have shown that there are two kinds of instabilities. The first one is the classical viscous instability and the second is the radiative instability, which is inviscid in nature and closely related to the stratification. For the Froude number interval $0.5 < F < 5.3$, the radiative instability is the first to appear as the Reynolds number increases. It starts to appear at $Re > Re_c^{(r)} \approx 1995$ for $F \approx 1.5$. For large Reynolds numbers, the radiative instability dominates in a large Froude number interval. For example, it is more unstable than the viscous instability in the interval $0.03 < F < 30$ for $Re = 10^6$. On the other side, the most unstable viscous instability remains two-dimensional in the presence of stratification. The critical Reynolds number for the viscous mode is $Re > Re_c^{(v)} \approx 3980$. Non-dimensionalised by the main mean velocity U and boundary layer thickness L, the oscillation frequency of the radiative modes is close to 1. The region covered by the most unstable mode can be as large as several times the boundary thickness. We have also shown that the growth rate of the radiative instability scales as ReF^2 in the parameter domain (large Re and small F) where the growth rate is the largest.

Applied to some practical examples, we believe that this instability could be present in experimental facilities and geophysical flows like ocean and atmosphere. However,as long as this instability has not been evidenced in the atmosphere and ocean, the impact of radiative instability remains unclear. Whether it contributes to the local mixing or the mixing far away from the boundary layer are interesting topics for further studies. The knowledge of nonlinear evolution of the radiative instability is also required to answer these questions and thus can become the subject of future works.

In chapter 4, we have performed modal and non-modal stability analysis of a stratified plane Poiseuille flow. A new exponential growing instability is obtained through modal

analysis, which behaves similarly to the radiative instability found in stratified boundary layers. The three-dimensional instability, which is referred to as the gravity mode in the present study, can be viewed as a version of the radiative instability in the finite domain or another version of strato-rotational instability in a parallel shear system. In the Reynolds number range that we have considered ($Re \leqslant 10^4$), this gravity mode turns out to be the result of a resonance between an inviscid mode and a viscous mode. The critical Reynolds number can be as small as $Re_c^{(p)} \approx 494$ for $F \approx 2.5$. The classical viscous instability preserves its property by remaining two-dimensional and thus independent of F. For $Re = 5000$, the viscous mode is stable whereas the gravity mode is unstable in a large Froude number interval $0.27 \leqslant F \leqslant 258$. The plane Poiseuille flow which is stable to viscous instability can then become exponentially unstable in the presence of a very weak stratification.

In Chapter 3 and 4, we have demonstrated that in the presence of stratification, stratified flows are more likely to become unstable because of the 3D radiative instability and the gravity modes. A resonance mechanism between the inviscid modes and viscous modes is demonstrated to be a source of modal instability. However, in terms of transient growth, the stably stratified flows are less sensitive. On the other side, the link between the eigenvalues and transient growth is strengthened by the stratification. The fundamental mechanisms of transient growth can also help to describe the growth of unstable mode in finite time intervals.

In the presence of stratification, the largest energy gain is associated with non-zero wavenumbers ($k_x k_z \neq 0$) for most cases in the (Re, F) plane. In exponentially stable flows with small Reynolds number or small Froude number, the transient growth can still reach $\mathcal{O}(10 - 100)$ for short time intervals (e.g. $T = 25$). The global maximum can be larger thus possibly exciting the nonlinear effects and transition to turbulence.

The nonlinear evolutions of the optimal perturbations can be interesting because the related nonlinear effects of these tilted roll vortices ($k_x k_z \neq 0$) are rich (Reddy & Henningson 1993). Experimental research are needed about the transient growth in stratified fluid in order to verify these effects. The influence of the transient growth with stratification is also an interesting topic for geophysical flows like oceans and the atmosphere.

As only the result of the modal analysis is provided in Chapter 3, one potential extension is the non-modal analysis of stratified boundary layer flows. The mathematical framework to search for the optimal perturbations is the same. However, as we discussed in Chapter 2, the standard pseudo-spectral method cannot precisely capture the eigenmodes, further treatment on the spatial discretization operator is required. One possible solution is to extend the method of the complex path, which is the method we have used for the modal analysis. A potential difficulty in this solution is the influence of meaningless numerical eigenmodes, which is a common problem encountered when using the spectral method. Another possible solution is to apply a numerical non-reflection boundary layer

conditions. This solution may provide a clean spectrum of the eigenmodes and avoid the weakness of pseudo-spectral method.

Another interesting topic is the Direct Numerical Simulation (DNS). The effects of non-linear terms can indeed be considered by DNS. Based on our primary result of oscillation frequencies and wavenumbers in Chapter 3 and 4, small time steps and fine meshes are required for the simulation. These simulations would contribute to a better understanding of the stability in a stratified fluid.

Although the transient growth is optimised mathematically, background or white noise may select different structures. The perturbations which grow robustly rather than optimally may become dominant in the experiment, as suggested by Butler & Farrell (1992) for the unstratified cases. Experiments about stratified flows can experience same problems, but the transient growth result can give fundamental evaluations and suggestions for these studies.

In the field of geophysical flows, our results can help to explain the generation of instabilities and turbulence mixing in stably stratified fluids, especially in the context of complicated geometry. Internal gravity waves can be produced due to the radiative instability, which can exhibit far away from the boundary layers on the cliffs. The transient growth analysis can also be regarded as a preliminary study about the stabilities of realistic stratified flows in nature.

Bibliographie

Acheson, D. J. 1976 On over-reflexion. *Journal of Fluid Mechanics* **77** (03), 433.

Alavyoon, F., Henningson, D. S. & Alfredsson, P. H. 1986 Turbulent spots in plane Poiseuille flow–flow visualization. *Physics of Fluids* **29** (4), 1328.

Alford, M. & Gregg, M. 2006 Structure, propagation, and mixing of energetic baroclinic tides in Mamala Bay, Oahu, Hawaii. *Journal of Physical Oceanography* **36**, 997–1018.

Apel, J. R., Holbrook, J. R., Liu, A. K. & Tsai, J. J. 1985 The Sulu Sea Internal Soliton Experiment. *Journal of Physical Oceanography* **15** (12), 1625–1651.

Arratia, C. 2011 Non-modal instability mechanisms in stratified and homogeneous shear flow. PhD thesis, Ecole Polytechnique.

Arratia, C., Caulfield, C. P. & Chomaz, J.-M. 2013 Transient perturbation growth in time-dependent mixing layers. *Journal of Fluid Mechanics* **717**, 90–133.

Arratia, C., Ortiz, S. & Chomaz, J.-M. 2016 Inviscid Transient Growth on Horizontal Shear Layers with Strong Vertical Stratification. In *Nonlinear Dynamics : Materials, Theory and Experiments* (ed. Mustapha Tlidi & Marcel G. Clerc), pp. 199–206. Springer International Publishing.

Augier, P., Billant, P., Negretti, M. E. & Chomaz, J. M. 2014 Experimental study of stratified turbulence forced with columnar dipoles. *Physics of Fluids* **26**, 046603.

Bakas, N. a. & Farrell, B. F. 2009*a* Gravity Waves in a Horizontal Shear Flow. Part I : Growth Mechanisms in the Absence of Potential Vorticity Perturbations. *Journal of Physical Oceanography* **39**, 497–511.

Bakas, N. a. & Farrell, B. F. 2009*b* Gravity Waves in a Horizontal Shear Flow. Part II : Interaction between Gravity Waves and Potential Vorticity Perturbations. *Journal of Physical Oceanography* **39**, 497–511.

Balmforth, N. J. 1999 Shear instability in shallow water. *Journal of Fluid Mechanics* **387**, 97–127.

Basak, S. & Sarkar, S. 2006 Dynamics of a stratified shear layer with horizontal shear. *Journal of Fluid Mechanics* **568**, 19–54.

Betchov, R. & Criminale, W. O. 1967 *Stability of Parallel Flows*. New York : Academic Press.

Biau, D. & Bottaro, A. 2004 The effect of stable thermal stratification on shear flow stability. *Journal of Fluid Mechanics* **16**, 4742–4745.

Billant, P. & Chomaz, J. M. 2001 Self-similarity of strongly stratified inviscid flows. *Physics of Fluids* **13** (6), 1645–1651.

Billant, P. & Le Dizès, S. 2009 Waves on a columnar vortex in a strongly stratified fluid. *Physics of Fluids* **21**, 106602.

Broadbent, E. G. & Moore, D. W. 1979 Acoustic destabilization of vortices. *Philosophical Transactions of the Royal Society of London A : Mathematical, Physical and Engineering Sciences* **290**, 353–371.

Butler, K. B. & Farrell, B. F. 1993 Optimal perturbations and streak spacing in wall bounded shear flow. *Phys. Fluids A* **5**, 774.

Butler, K. M. & Farrell, B. F. 1992 Three-dimensional optimal perturbations in viscous shear flow. *Physics of Fluids* **4** (8), 1637–1650.

Candelier, J. 2010 Instabilités radiatives des couches limites atmosphériques. PhD thesis, Aix-Marseille Université, Marseille.

Candelier, J., Le Dizès, S. & Millet, C. 2011 Shear instability in a stratified fluid when shear and stratification are not aligned. *Journal of Fluid Mechanics* **685**, 191–201.

Candelier, J., Le Dizès, S. & Millet, C. 2012 Inviscid instability of a stably stratified compressible boundary layer on an inclined surface. *Journal of Fluid Mechanics* **694**, 524–539.

Carlson, D. R., Widnall, S. E. & Peeters, M. F. 1982 A flow-visualization study of transition in plane Poiseuille flow. *Journal of Fluid Mechanics* **121**, 487–505.

Churilov, S. M. 2005 Stability analysis of stratified shear flows with a monotonic velocity profile without inflection points. *Journal of Fluid Mechanics* **539**, 25–55.

Churilov, S. M. 2008 Stability analysis of stratified shear flows with a monotonic velocity profile without inflection points. Part 2. Continuous density variation. *Journal of Fluid Mechanics* **617**, 301–326.

Corbett, P. & Bottaro, A. 2000 Optimal perturbations for boundary layers subject to stream-wise pressure gradient. *Physics of Fluids* **12** (1), 120.

Deloncle, A., Chomaz, J.-M. & Billant, P. 2007 Three-dimensional stability of a horizontally sheared flow in a stably stratified fluid. *Journal of Fluid Mechanics* **570**, 297.

Drazin, P. & Reid, W. 1981 *Hydrodynamic Stability*. Cambridge University Press.

Ellingsen, T. & Palm, E. 1975 Stability of linear flow. *Physics of Fluids* **18** (4), 487–488.

Farrell, B. F. 1988 Optimal excitation of perturbations in viscous shear flow. *Physics of Fluids* **31** (8), 2093–2102.

Farrell, B. F. & Ioannou, P. J. 1993*a* Optimal excitation of three-dimensional perturbations in viscous constant shear flow. *Physics of Fluids* **5**, 1390–1400.

Farrell, B. F. & Ioannou, P. J. 1993*b* Perturbation growth in shear flow exhibits universality. *Phys. Fluids* **5** (9), 2298–2300.

Farrell, B. F. & Moore, A. M. 1992 An Ajoint Method for Obtaining the Most Rapidly Growing Perturbation to Oceanic Flows. *Journal of Physical Oceanography* **22**, 338–349.

Fernando, H. J. 1991 Turbulent Mixing in Stratified Fluids. *Annual Review of Fluid Mechanics* **23**, 455–93.

Fjørtoft, R. 1950 Application of integral theorems in deriving criteria of stability for laminar flows and for the baroclinic circular vortex. *Geofysiske Publikasjoner* **17**, 1–28.

Frehlich, R., Meillier, Y. & Jensen, M. L. 2008 Measurements of Boundary Layer Profiles with In Situ Sensors and Doppler Lidar. *Journal of Atmospheric and Oceanic Technology* **25** (8), 1328–1340.

Fritts, D. C. & Alexander, M. J. 2003 Gravity wave dynamics and effects in the middle atmosphere. *Reviews of Geophysics* **41** (1), 1003.

Garrett, C. 2003 Oceanography : Mixing with latitude. *Nature* **422** (6931), 477–477.

Gossard, E. E. & Hooke, W. H. 1975 *Waves in the atmosphere : atmospheric infrasound and gravity waves-their generation and propagation*. Amsterdam : Elsevier Scientific Publishing Co.

Grimshaw, R. H. J. 1979 On resonant over-reflexion of internal gravity waves from a Helmholtz velocity profile. *J. Fluid Mech.* **90** (01), 161.

Gustavsson, L. H. 1991 Energy growth of three-dimensional disturbances in plane Poiseuille flow. *Journal of Fluid Mechanics* **224**, 241–260.

Heisenberg, W. 1924 Über stabilität und turbulenz von FlÜssigkeitsströmen. *Anndlen der Physik* **74**, 577–627.

Henningson, D. S., Lundbladh, A. & Johansson, A. V. 1993 A mechanism for bypass transition from localized disturbances in wall-bounded shear flows. *Journal of Fluid Mechanics* **250**, 169–207.

Henningson, D. S. & Reddy, S. C. 1994 On the role of linear mechanisms in transition to turbulence. *Physics of Fluids* **6** (3), 1396.

Howard, L. 1961 Note on a paper of John W. Miles. *Journal of Fluid Mechanics* **10** (04), 509–512.

Ivey, G., Winters, K. & Koseff, J. 2008 Density Stratification, Turbulence, but How Much Mixing ? *Annual Review of Fluid Mechanics* **40** (1), 169–184.

Jerome, J. J. S. & Chomaz, J.-M. 2014 Extended Squire's transformation and its consequences for transient growth in a confined shear flow. *Journal of Fluid Mechanics* **744**, 430–456.

Jerome, J. J. S., Chomaz, J. M. & Huerre, P. 2012 Transient growth in Rayleigh-Bénard-Poiseuille/Couette convection. *Physics of Fluids* **24**, 044103.

Kaminski, A. K., Caulfield, C. P. & Taylor, J. R. 2014 Transient growth in strongly stratified shear layers. *Journal of Fluid Mechanics* **758**, R4.

Kendall, J. M. 1985 Experimental Study of Disturbances Produced in a Pre-Transitional Laminar Boundary Layer by Weak Freestream Turbulence. *AIAA 18th Fluid Dynamics and Plasmadynamics and Lasers Conference* p. 1695.

Kerswell, R. R., Pringle, C. C. T. & Willis, a. P. 2014 An optimization approach for analysing nonlinear stability with transition to turbulence in fluids as an exemplar. *Reports on Progress in Physics* **77**, 085901.

Klebanof, P. S. 1971 Effect of free-stream turbulence on a laminar boundary layer. *Bulletin of the American Physical Society* **16**, 1323.

Klebanoff, P. S., Tidstrom, K. D. & Sargent, L. M. 1962 The three-dimensional nature of boundary-layer instability. *Journal of Fluid Mechanics* **12** (01), 1–34.

Kópev, V. & Leontev, E. 1983 Acoustic instability of an axial vortex. *Soviet physics acoustics* **29**, 111–115.

Kuhlbrodt, T., Griesel, A., Montoya, M., Levermann, A., Hofmann, M. & Rahmstorf, S. 2007 On the driving processes of the Atlantic meridional overturning circulation. *Reviews of Geophysics* **45**, RG2001.

Landahl, M. T. 1975 Wave Breakdown and Turbulence. *SIAM Journal on Applied Mathematics* **28** (4), 735–756.

Landahl, M. T. 1980 A note on an algebraic instability of inviscid parallel shear flows. *Journal of Fluid Mechanics* **98** (02), 243.

Le Dizès, S. & Billant, P. 2009 Radiative instability in stratified vortices. *Physics of Fluids* **21** (9), 096602.

Le Dizès, S. & Riedinger, X. 2010 The strato-rotational instability of Taylor–Couette and Keplerian flows. *Journal of Fluid Mechanics* **660**, 147–161.

Lindborg, E. 2006 The energy cascade in a strongly stratified fluid. *Journal of Fluid Mechanics* **550**, 207–242.

Lindzen, R. & Barker, J. 1985 Instability and wave over-reflection in stably stratified shear flow. *Journal of Fluid Mechanics* **151**, 189–217.

Lindzen, R. S. 1988 Instability of plane parallel shear flow (toward a mechanistic picture of how it works). *Pure and Applied Geophysics PAGEOPH* **126** (1), 103–121.

Lindzen, R. S., Farrell, B. & Tung, K.-K. 1980 The Concept of Wave Overreflection and Its Application to Baroclinic Instability. *Journal of the Atmospheric Sciences* **37** (1), 44–63.

Lindzen, R. S. & Rambaldi, S. 1986 A study of over-reflection in viscous Poiseuille flow. *Journal of Fluid Mechanics* **165**.

Lindzen, R. S. & Tung, K. K. 1978 Wave Over-reflection and Shear Instability. *Journal of the Atmospheric Sciences* **35** (9), 1626–1632.

Luchini, P. 2000 Reynolds-number-independent instability of the boundary layer over a flat surface : optimal perturbations. *Journal of Fluid Mechanics* **404**, 289–309.

Luchini, P. & Bottaro, A. 2014 Adjoint Equations in Stability Analysis. *Annual Review of Fluid Mechanics* **46**, 493–517.

Mack, L. M. 1976 A numerical study of the temporal eigenvalue spectrum of the Blasius boundary layer. *Journal of Fluid Mechanics* **73** (03), 497–520.

Mack, L. M. 1990 On the inviscid acoustic-mode instability of supersonic shear flows - Part 1 : Two-dimensional waves. *Theoretical and Computational Fluid Dynamics* **2** (2), 97–123.

Mack, S. A. & Schoeberlein, H. C. 2004 Richardson Number and Ocean Mixing : Towed Chain Observations. *Journal of Physical Oceanography* **34** (4), 736–754.

Mahrt, L. 2014 Stably Stratified Atmospheric Boundary Layers. *Annual Review of Fluid Mechanics* **46**, 23–45.

Matsubara, M. & Alfredsson, P. H. 2001 Disturbance growth in boundary layers subjected to free-stream turbulence. *Journal of Fluid Mechanics* **430**, 149–168.

McIntyre, M. E. & Weissman, M. a. 1978 On Radiating Instabilities and Resonant Overreflection. *Journal of the Atmospheric Sciences* **35** (7), 1190–1196.

Miles, J. W. 1957 On the Reflection of Sound at an Interface of Relative Motion **29**, 226–228.

Miles, J. W. 1961 On the stability of heterogeneous shear flows. *Journal of Fluid Mechanics* **16** (2), 496–508.

Mowbray, D. E. & Rarity, B. S. H. 1967 A theoretical and experimental investigation of the phase configuration of internal waves of small amplitude in a density stratified liquid. *Journal of Fluid Mechanics* **28** (01), 1–16.

Nishioka, M., A, S. I. & Ichikawa, Y. 1975 An experimental investigation of the stability of plane Poiseuille flow. *Journal of Fluid Mechanics* **72** (04), 731–751.

Nishioka, M. & Asai, M. 1985 Some observations of the subcritical transition in plane Poiseuille flow. *Journal of Fluid Mechanics* **150**, 441–450.

Ohya, Y. & Uchida, T. 2003 Turbulence structure of stable boundary layers with a near-linear temperature profile. *Boundary-Layer Meteorology* **108** (1), 19–38.

Orr, W. M. 1907 The Stability or Instability of the Steady Motions of a Perfect Liquid and of a Viscous Liquid. *Proceedings of the Royal Irish Academy* **27**, 9–68.

Orszag, S. a. 1971 Accurate solution of the Orr–Sommerfeld stability equation. *Journal of Fluid Mechanics* **50** (04), 689–703.

Paci, A., Knigge, C., Etling, D., Johnson, T., Esler, G., Cazin, S., Cid, E., Eiff, O. & Lacaze, L. 2011 Topographic internal waves in the laboratory : two recent experiments carried in the CNRM-GAME stratified water tank. *Geophysical Research Abstracts* **13** (February 2010), 30141–30141.

Park, J. & Billant, P. 2012 Radiative instability of an anticyclonic vortex in a stratified rotating fluid. *Journal of Fluid Mechanics* **707**, 381–392.

Park, J. & Billant, P. 2013*a* Instabilities and waves on a columnar vortex in a strongly stratified and rotating fluid. *Physics of Fluids* **25**, 086601.

Park, J. & Billant, P. 2013*b* The stably stratified Taylor–Couette flow is always unstable except for solid-body rotation. *Journal of Fluid Mechanics* **725**, 262–280.

Parras, L. & Le Dizès, S. 2010 Temporal instability modes of supersonic round jets. *Journal of Fluid Mechanics* **662**, 173–196.

Plougonven, R. & Zeitlin, V. 2002 Internal gravity wave emission from a pancake vortex : An example of wave-vortex interaction in strongly stratified flows. *Physics of Fluids* **14** (3), 1259–1268.

Polzin, K. & Ferrari, R. 2004 Isopycnal Dispersion in NATRE. *Journal of Physical Oceanography* **34** (1), 247–257.

Rayleigh, L. 1880 On the stability, or instability, of certain fluid motions. *Proc. London Math. Soc.* **11**, 57–70.

Reddy, S. C. & Henningson, D. S. 1993 Energy growth in viscous channel flows. *Journal of Fluid Mechanics* **252**, 209.

Reid, W. 1965 The stability of parallel flows. In *Basic Developments in Fluid Dynamics*. Academic Press.

Reynolds, O. 1883 An experimental investigation of the circumstances which determine whether the motion of water shall be direct or sinuous, and of the law of resistance in parallel channels. *Proceedings of the royal society of London* **35** (224-226), 84–99.

Ribner, H. S. 1957 Reflection, Transmission, and Amplification of Sound by a Moving Medium. *The Journal of the Acoustical Society of America* **29** (4), 435.

Riedinger, X. 2009 Instabilité radiative d'un tourbillon dans un fluide stratifié. PhD thesis, Universite de Provence, Aix-Marseille I.

Riedinger, X. & Gilbert, A. D. 2014 Critical layer and radiative instabilities in shallow-water shear flows. *Journal of Fluid Mechanics* **751**, 539–569.

Riedinger, X., Le Dizès, S. & Meunier, P. 2010*a* Viscous stability properties of a Lamb-Oseen vortex in a stratified fluid. *Journal of Fluid Mechanics* **645**, 255–278.

Riedinger, X., Le Dizès, S. & Meunier, P. 2011 Radiative instability of the flow around a rotating cylinder in a stratified fluid. *Journal of Fluid Mechanics* **672**, 130–146.

Riedinger, X., Meunier, P. & Le Dizès, S. 2010*b* Instability of a vertical columnar vortex in a stratified fluid. *Experiments in Fluids* **49** (3), 673–681.

Riley, J. J. & De Bruyn Kops, S. M. 2003 Dynamics of turbulence strongly influenced by buoyancy. *Physics of Fluids* **15** (7), 2047–2059.

Satomura, T. 1981 An investigation of shear instability in a shallow water. *J. Met. Soc. Japan* **59** (1), 148–167.

Schecter, D. a. & Montgomery, M. T. 2004 Damping and pumping of a vortex Rossby wave in a monotonic cyclone : Critical layer stirring versus inertia–buoyancy wave emission. *Physics of Fluids* **16** (5), 1334–1348.

Schlichting, H. 1933 Zur enstehung der turbulenz bei der plattenströmung. *Nachrichten von der Gesellschaft der Wissenschaften zu Göttingen, Mathematisch-Physikalische Klasse* **1933**, 181–208.

Schmid, P. J. 2007 Nonmodal Stability Theory. *Annual Review of Fluid Mechanics* **39**, 129–162.

Schmid, P. J. & Henningson, D. S. 2001 *Stability and Transition in Shear Flows*. Springer.

Spedding, G. R., Browand, F. K. & Fincham, A. M. 1996 Turbulence, similarity scaling and vortex geometry in the wake of a towed sphere in a stably stratified fluid. *Journal of Fluid Mechanics* **314**, 53–103.

Squire, H. B. 1933 On the Stability for Three-Dimensional Disturbances of Viscous Fluid Flow between Parallel Walls. *Proceedings of the Royal Society A : Mathematical, Physical and Engineering Sciences* **142** (847), 621–628.

Staquet, C. & Sommeria, J. 2002 Internal Gravity Waves : From Instabilities to Turbulence. *Annual Review of Fluid Mechanics* **34** (1), 559–593.

Süli, E. & Mayers, D. 2003 *An introduction to numerical analysis*. Cambridge University Press.

Takehiro, S.-I. & Hayashi, Y.-Y. 1992 Over-reflection and shear instability in a shallow-water model. *Journal of Fluid Mechanics* **236**, 259–279.

Tollmien, W. 1929 Über die Entstehung der Turbulenz. *Nachrichten von der Gesellschaft der Wissenschaften zu Göttingen, Mathematisch-Physikalische Klasse* pp. 21–44.

Tollmien, W. 1935 Ein allgemeines Kriterium der Instabilität laminarer Geschwindigkeitsverteilungen .

Trefethen, L. N., Trefethen, A. E., Reddy, S. C. & Driscoll, T. A. 1993 Hydrodynamic Stability Without Eigenvalues. *Science* **261**.

Wu, X. & Luo, J. 2006 Influence of small imperfections on the stability of plane Poiseuille flow and the limitation of Squire's theorem. *Phys. Fluids* **18** (044104).

Wu, X. & Zhang, J. 2008*a* Instability of a stratified boundary layer and its coupling with internal gravity waves. Part 1. Linear and nonlinear instabilities. *Journal of Fluid Mechanics* **595**, 379–408.

Wu, X. & Zhang, J. 2008*b* Instability of a stratified boundary layer and its coupling with internal gravity waves. Part 2. Coupling with internal gravity waves via topography. *Journal of Fluid Mechanics* **595**, 409–433.

Wunsch, C. & Ferrari, R. 2004 Vertical Mixing, Energy, and the General Circulation of the Oceans. *Annual Review of Fluid Mechanics* **36** (1), 281–314.

Yavneh, I., McWilliams, J. C. & Molemaker, M. J. 2001 Non-axisymmetric instability of centrifugally stable stratified Taylor-Couette flow. *Journal of Fluid Mechanics* **448**, 1–21.